LEAD ZIRCONATE TITANATE NANOTUBES PROCESSED VIA SOFT TEMPLATE INFILTRATION

A Dissertation
Presented to
The Academic Faculty

By

Ashley Bernal

In Partial Fulfillment
Of the Requirements for the Degree
Doctor of Philosophy in Mechanical Engineering

Georgia Institute of Technology

December, 2011

Copyright © Ashley Bernal 2011

Lead Zirconate Titanate Nanotubes Processed via Soft Template Infiltration

Approved by:

Dr. Nazanin Bassiri-Gharb, Advisor
G.W. Woodruff School of Mechanical Engineering
Georgia Institute of Technology

Dr. Rosario Gerhardt
School of Materials Science and Engineering
Georgia Institute of Technology

Dr. Peter Hesketh
G.W. Woodruff School of Mechanical Engineering
Georgia Institute of Technology

Dr. Oliver Brand
School of Electrical and Computer Engineering
Georgia Institute of Technology

Dr. Todd Sulchek
G.W. Woodruff School of Mechanical Engineering
Georgia Institute of Technology

Date Approved: October 28, 2011

ACKNOWLEDGEMENTS

First of all, I would like to thank my advisor Dr. Bassiri-Gharb. I thoroughly enjoyed working with her throughout graduate school and appreciated her support. Without her persuasion and adaptability in projects, I would not have had the opportunity to develop a passion for the field of ferroelectrics and nanoscale manufacturing. For this I am truly thankful. She was the type of advisor that was always accessible, extremely encouraging, and supportive of my desire to teach. Because of her, I was able to achieve my life-long career goal. We were able to develop a great working relationship, which I hope will continue well beyond graduate school.

I would also like to thank all of my committee members: Dr. Brand, Dr. Gerhardt, Dr. Hesketh, and Dr. Sulchek for providing research advice and asking thought provoking questions. Very special thanks to my undergraduate mentor, Dr. Ferro. His enthusiasm and passion inspired me to continue my education beyond a bachelor's degree in a multi-discipline project with a materials science flare. A thank you is also warranted to Dr. Ravi for teaching the lab portion of the MEMS class. The processing knowledge gained through these experiments was extremely valuable and pivotal to this thesis.

Also, thanks to all of the Nanotechnology Research Center (NRC) cleanroom staff members. I appreciate all of the support you have provided me over the years regarding processing questions and dedication to keep the cleanroom tools running. My appreciation also extends to the SPM group at Oakridge National Lab: Drs. Amit Kumar, Stephen Jesse, and Sergei Kalinin for help with PFM measurements and Dr. Alexander Tselev for modeling the electric field distribution in the PZT nanotubes.

I would like to thank all of the undergrads and high school students that worked with me over the past years: Joel Weber, Jared Frazier, Blair Kim, Max Lifson, Jonathan Shum, Elisabeth Deeb, and Yann Allemann. I thoroughly enjoyed getting to know each and every one of you and best of luck with your future endeavors.

TABLE OF CONTENTS

LIST OF TABLES

LIST OF FIGURES

NOMENCLATURE

A	Piezoelectric strain-amplitude response
AAO	Anodic aluminum oxide
AC	Alternating current
α_d'	Real irreversible piezoelectric Rayleigh coefficient
α_d"	Imaginary irreversible piezoelectric Rayleigh coefficient
α_ε'	Real irreversible dielectric Rayleigh coefficient
α_ε"	Imaginary irreversible dielectric Rayleigh coefficient
A_{el}	Strain-amplitude due to electrostatic interactions
AF	Antiferroelectric phase
AFM	Atomic force microscopy
ALD	Atomic layer deposition
A_{max}	Maximum strain-amplitude
A_{nl}	Strain-amplitude due to nonlocal contributions due to buckling
A_{piezo}	Strain-amplitude due to piezoelectric response
A_s	Constant dependent on dielectric permittivity
A_w	Amplitude of probing voltage
β	Calibration sensitivity
BE-PFM	Band excitation piezoresponse force microscopy
χ	Dielectric susceptibility
CSI	Contact limited strong indentation regime

d	Piezoelectric coefficient
d’	Real component piezoelectric coefficient
d”	Imaginary component piezoelectric coefficient
d*	Complex piezoelectric coefficient
D	Dielectric displacement
Δ	Change in polarization angle
ΔD	Change in dielectric displacement
DC	Direct current
d_h	Hydrostatic piezoelectric coefficient
DI	Deionized
D-SS-PFM	Dynamic switching spectroscopy piezoresponse force microscopy
E	Electric field $E=E_o\sin(\omega t)$
ε	Dielectric permittivity
ε’	Real component dielectric permittivity
ε”	Imaginary component dielectric permittivity
ε^*	Complex dielectric permittivity
EBL	Electron beam lithography
E_c	Coercive field
E_d	Depolarizing field
EDS	Energy dispersive x-ray spectroscopy
E_o	Amplitude of AC electric field
ε_o	Permittivity of free-space

ε_r	Relativity permittivity
E_{th}	Threshold field
F	Ferroelectric phase
FE	Ferroelectric
FEM	Finite Element Modeling
FIB	Focus ion beam
HT	Heat treatment
h_w	Amplitude of PRS
j	$\sqrt{-1}$
$\Delta\lambda$	Change in wavelength
LE	Linear elastic regime
LIL	Laser interference lithography
M	Electrostrictive coefficient
MPB	Morphotropic phase boundary
MOEMS	Micro-opto-electro-mechanical systems
NE	Nonlinear elastic regime
NL	Non-local effects regime
NOEMS	Nano-opto-electro-mechanical systems
O	Orthorhombic phase
P	Dielectric polarization
Ψ	Piezoresponse phase angle
P_c	Paraelectric cubic phase
P_d	Domain's polarization

PD	Plastic deformation regime
PFM	Piezoresponse force microscopy
PLD	Pulsed laser deposition
PRS	Piezoresponse signal
PZT	Lead zirconate titanate
Q	Electromechanical quality factor
R	Rhombohedral phase
RIE	Reactive ion etch
r_p	Normalized complex reflectance perpendicular to the sample
r_s	Normalized complex reflectance parallel to the sample
RTP	Rapid thermal processor
s	Elastic compliance
σ	Applied stress
SHO	Simple harmonic oscillator
SI	Strong indentation regime
SS-PFM	Switching spectroscopy piezoresponse force microscopy
t	Time
T	Temperature
ΔT	Change in temperature
t_c	Thickness of crystal
T_c	Curie temperature
TMA	Trimethyl aluminum
TR	Tetragonal phase

V	Volume of crystal
ω	Angular frequency
w_d	Domain width
W_e	Electrostatic energy
ω_o	Resonant frequency
W_w	Domain wall energy
x	Strain
XRD	X-ray diffraction
2-MOE	2-methoxyethanol

SUMMARY

The study of ferroelectric materials at small dimensions has been of increasing interest due to their numerous possible piezoelectric and ferroelectric applications such as memory devices, actively tunable photonic crystals, terahertz emitters, ultrasound transducers, energy harvesters, and micro/nano-electromechanical (MEMS/NEMS) sensors and actuators. Studies of ferroelectric size effects have been mostly limited due to difficulties in fabricating small scale piezoelectric materials with prescribed aspect ratios without damaging the surface layers of the ferroelectric via etching. Due to these fabrication difficulties, experimental verification of theoretical predictions of material characteristics for ferroelectrics at small scales is lacking. Therefore, this work focuses first on developing a manufacturing method of patterning ferroelectric materials at nanometer scale utilizing vacuum infiltration of PZT sol-gel solution into a soft-template, enabling the development of piezoelectric and ferroelectric NEMS/MEMS devices, and second to perform experimental studies to investigate the extrinsic contributions to the piezoelectric and ferroelectric response of nanoscale ferroelectrics.

CHAPTER 1

INTRODUCTION

This chapter outlines the motivation of this research. It also discusses the main objectives for this thesis and provides a basic overview of the PZT nanotube manufacturing approach developed herein and experiments conducted.

1.1 Introduction

High aspect ratio ferroelectric materials with sub-micron sized definition such as PZT have a wide range of potential applications including: actively tunable photonic crystals, terahertz emitters, ultrasound transducers, and energy harvesters. However, the major technological challenge of developing these devices is the current limitation of the available processing methods in patterning piezoelectric materials with prescribed aspect ratios in user-defined locations. Typical methods allowing tailorability of the aspect ratios of the ferroelectric structures produced involve wet and focused ion beam etching, the latter leading to a reduction in the ferroelectric properties due to surface damage, while the former is not appropriate for applications where the feature size approaches the ferroelectric (FE) grain size. This approach is extremely detrimental for nanosized structures where the surface area to volume ratio is extremely large. Therefore, the primary objective of this work is to develop a manufacturing approach for producing piezoelectric nanotubes with site specific registration and aspect ratio control without damaging the piezoelectric response. The secondary objective of this work is to

characterize the piezoelectric response of the resulting structures. The dielectric and piezoelectric response of PZT has an intrinsic and extrinsic component. The intrinsic component is due to the average unit cell distortion, and the extrinsic component represents domain wall and phase boundary motion contributions. The extrinsic contribution has shown to account for up to 80% of the total dielectric piezoelectric response of bulk polycrystalline ferroelectric materials at room temperature [1]. Therefore, studying the factors that influence the extrinsic component (i.e. domain wall motion) is essential to develop devices with large piezoelectric and dielectric response. Thus, the research discussed herein investigates nanoscale phenomena such as substrate clamping, lateral constraint, and ferroelectric wall tube thickness and their effect on the measured piezoelectric response.

1.2 Thesis Organization

Based on the above overview, this thesis is organized as follows:

Literature Review (Chapter 2)

Background information is provided by introduction of ferroelectricity and piezoelectricity. Different approaches of separating intrinsic and extrinsic contributions to the dielectric and piezoelectric response are reviewed. The application of Rayleigh law to describe the extrinsic response in ferroelectrics is also discussed. Furthermore, the properties of PZT are compared as a function of composition. Different methods for patterning piezoelectric materials at the nanometer scale as well as phenomena emerging at these small dimensions are reviewed.

Micro/Nanofabrication Methods and Characterization Techniques (Chapter 3)

Cleanroom processes used for fabrication of ferroelectric nanostructures included thermal oxidation, sputter deposition, atomic layer deposition (ALD), and electron beam lithography. Methods for process characterization used in this research primarily rely on film thickness verification methods such as refractometry and ellipsometry. In addition, perovskite phase formation for PZT nanotubes is confirmed via x-ray diffraction and micro-Raman spectroscopy. The piezoelectric response of the resulting nanostructures is determined via band-excitation piezoresponse force microscopy (BE-PFM) and switching spectroscopy piezoresponse force microscopy (SS-PFM). The operation principles for these cleanroom processes and characterization techniques are discussed in detail in this chapter.

Manufacturing Method (Chapter 4)

A soft-template infiltration approach is developed for manufacturing PZT nanotubes on platinized wafers. Critical processing steps for creating PZT nanotubes are discussed and specifically include: coating the soft-templates via ALD and immersing the coated soft-template in an ultrasound bath of PZT precursor while under vacuum. This chapter also provides possible methods for Al_2O_3 removal and top-electrode deposition.

PZT Nanotube Fabrication Optimization (Chapter 5)

Several processing steps require optimization for PZT nanotube fabrication. The exposure dose and development time for soft-template patterning was determined for a variety of aspect ratios. The atomic layer thickness was also optimized for mechanical

consolidation requirements, while still providing escape paths for organics created during thermal deposition. In addition, a hierarchical patterning was developed to prevent cracks and delaminating. Furthermore, the optimal thermal heat treatment was determined for perovskite phase formation, while minimizing stiction.

PZT Nanotube Characterization (Chapter 6)

PZT nanotubes are characterized in terms of chemical composition, crystallographic structure, and basic piezoelectric response. Perovskite phase is confirmed by comparing micro-Raman spectra with reference PZT thin films, while the chemical composition is verified via energy dispersive x-ray spectroscopy (EDS) analysis. In addition, the piezoelectric and ferroelectric nature of the tubes were characterized via read and write experiments performed via band excitation piezoresponse force microscopy (BE-PFM) and switching spectroscopy piezoresponse force microscopy (SS-PFM).

Nanoscale Phenomena (Chapter 7)

The shrinking of ferroelectric structures to the nanoscale produces new physical phenomena that require further understanding. This chapter is dedicated to the investigation of extrinsic contributions to the piezoelectric response by characterizing PZT nanotubes with various aspect ratios, lateral constraints, and wall thicknesses to better understand factors effecting domain wall motion such as substrate clamping, lateral constraint effects, and critical size.

Conclusions and Future Work (Chapter 8)

A summary of the research performed is reported and future recommendations are provided in order to improve manufacturability of the tubes as well as expand the knowledge regarding piezoelectric and ferroelectric response in ferroelectric nanostructured materials.

CHAPTER 2

LITERATURE REVIEW

This chapter focuses on providing background information regarding the literature relevant to the current investigation. An introduction regarding electromechanical properties is provided, followed by ferroelectric phenomena and domain formation. The ferroelectric response is characterized in terms of intrinsic and extrinsic contributions as a function of frequency, temperature, and aging (time-dependence). In particular, a detailed discussion is provided for nonlinearities that develop due to the dielectric and piezoelectric coefficient's (linear) dependence on the applied electric field, which is quantified using the Rayleigh law. The properties of PZT and current manufacturing methods used to pattern ferroelectric materials are also discussed. The chapter concludes with nanoscale phenomena.

2.1 Piezoelectric Materials

Piezoelectrics are materials that develop a charge polarization in response to an applied stress (Equation 2.1), and conversely develop a strain due to an applied electric field (Equation 2.2) (Figure 2.1) [2-3].

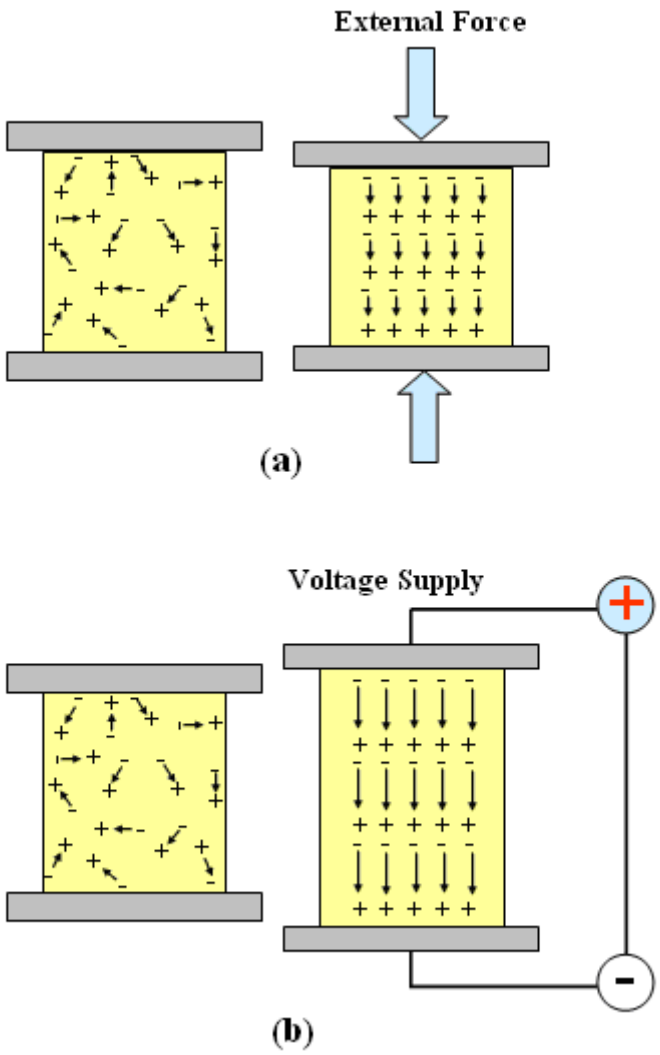

Figure 2.1: Schematic illustration of (a) direct and (b) converse piezoelectric effect.

The piezoelectric tensor describes the electromechanical coupling between the stimuli and response (Einstein notation implies summation over repeated indices):

$$D_i = d_{ijk}\sigma_{jk} \qquad \text{Equation 2.1}$$

$$x_{ij} = d_{kij}E_k \qquad \text{Equation 2.2}$$

In Equation 2.1, D_i is the dielectric displacement, d_{ijk} is the direct piezoelectric coefficient, and σ_{jk} is the applied stress. In Equation 2.2, x_{ij} is the resulting strain produced via the electric field E_k, and d_{kij} is the converse piezoelectric coefficient. In the following chapters of this thesis, reduced matrix notation (engineering notation) is used for tensor properties [3].

For unconstrained piezoelectric materials, the constants describing the electromechanical coupling are identical for the direct and converse effects [4]. Equation 2.1 and Equation 2.2 are only valid for small signal excitations as for higher driving fields the piezoelectric coefficients are no longer constant but rather dependent on the amplitude of the applied electric field [1].

Piezoelectricity develops in presence of an electric dipole moment created by ionic crystal lattices with asymmetric charge surroundings. All noncentrosymmetric crystal structures are piezoelectric except for point group 432, where the addition of symmetry elements leads to the absence of piezoelectricity (Figure 2.2) [2].

Piezoelectric materials are further classified as pyroelectric or non-pyroelectric. A pyroelectric material generates an electric potential in response to a change in temperature. In order for a material to exhibit pyroelectricity, it must be polar (i.e. the material must posses a natural charge separation or electrical dipoles in the absence of an electric field) [5]. The pyroelectric coefficient represents the proportionality constant between the change in temperature and the resulting change in electric displacement (Equation 2.3) [6].

$$\Delta D_i = p_i \Delta T \qquad \text{Equation 2.3}$$

In Equation 2.3, ΔD_i is the change in the dielectric displacement, p_i is the pyroelectric coefficient, and ΔT is the change in temperature.

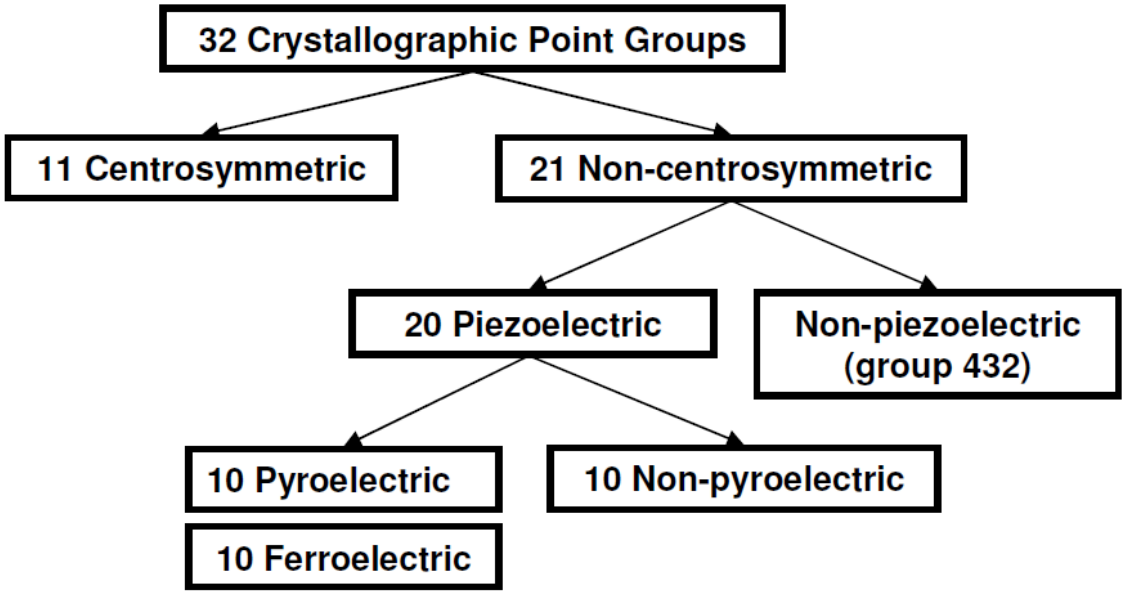

Figure 2.2: Flowchart demonstrating material classification of the 32 crystallographic point groups.

2.2 Ferroelectric Materials

Polar materials are further classified as ferroelectric and non-ferroelectric. A ferroelectric material, for a given temperature range, exhibits re-orientable spontaneous polarization between at least two equilibrium states via the application of an appropriate

electric field [7]. Not all polar materials are ferroelectric because the electric field required to reorient the spontaneous polarization can be higher than the breakdown field.

When cooling a ferroelectric material below its ferroelectric transition temperature (Curie temperature, T_c), spontaneous strain and charge develop due to distortion of the unit cell. In order to minimize the free energy of the system, domain structures are formed (Figure 2.3). Domains are volumes of material where the polarization direction is nearly uniform. The boundaries between domains are referred to as domain walls, which are named according to the angle formed between the spontaneous polarizations in adjacent domains (i.e. a 180^o domain wall is formed between two domains of opposite polarization direction).

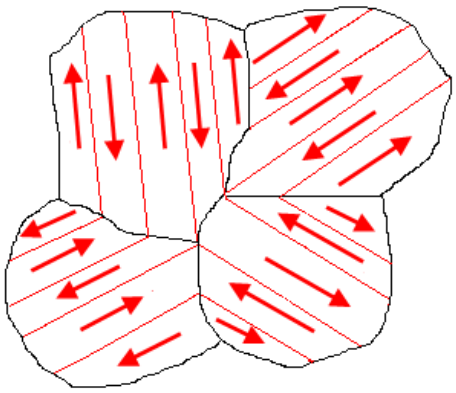

Figure 2.3: Schematic illustration of domain wall formation. The red lines represent domain walls and the black represent grain boundaries.

2.2.1 P-E and x-E Hysteresis Loops

One signature feature of ferroelectric materials is the nonlinear hysteretic polarization response to relatively large AC voltage excitations (P-E hysteresis loop) (Figure 2.1a) [4]. In a virgin polycrystalline materials (point O), when a small electric field is applied (E_j), the polarization (P_i) increases linearly with electric field, while the dielectric susceptibility (χ_{ij}) remains constant (Equation 2.4).

$$P_i = \chi_{ij} E_j \qquad \text{Equation 2.4}$$

As the electric field is further increased, domain wall motion occurs and the polarization response becomes nonlinear (i.e. the dielectric permittivity is a function of applied electric field). With further increase in the electric field, domains switch to increase alignment with respect to the applied electric field until saturation occurs (point A). As the field strength is then decreased, some of the domains will switch back but at zero field a remanent polarization exists (point B). As the field is increased with opposite polarity, eventually a zero net polarization is achieved (point C) corresponding to negative coercive field (E_c), and beyond which point small nuclei of domains with reverse polarization directions appear and grow. Eventually these domains merge until saturation is reached with ideally a single domain in the reversed polarization direction (point D). As the field is decreased and then increased with opposite polarity, the material undergoes nucleation of new domains with an opposite spontaneous polarization direction. The process continues until the hysteresis loop is completed with another saturation (point A).

The reorientation of the spontaneous polarization with the application of an electric field also produces an associated change in strain, resulting in a nonlinear hysteretic x-E (strain-electric field) response known as the "butterfly" loop (b) [4]. When the applied electric field is in the opposite direction of the net spontaneous polarization, the strain reduces until domains switch. Once the domains switch, the crystal expands due to the spontaneous polarization being in the same direction as the applied electric field.

The dominant nonlinearity in the strain response is due to domain wall motion; however, it should be noted other nonlinearities exist such as electrostriction [8]. Electrostriction applies to all crystal symmetries and describes the quadratic dependence of the resulting strain on the electric field where M_{ijkl} is the electrostrictive tensor (Equation 2.5) [9]. Electrostriction can also be described in terms of dielectric displacement (D) (Equation 2.6).

$$x_{ij} = M_{ijkl} E_k E_l \qquad \text{Equation 2.5}$$

$$x_{ij} = Q_{ijkl} D_k D_l \qquad \text{Equation 2.6}$$

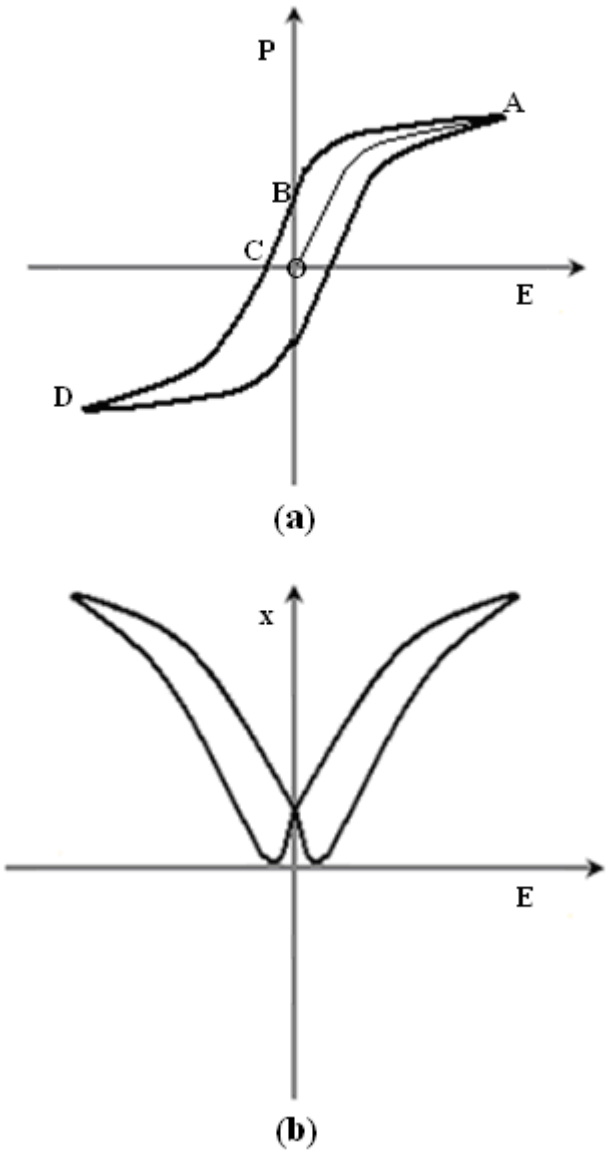

Figure 2.4: Schematic representation of the (a) polarization-electric field (P-E) hysteresis loop and the (b) strain-electric field (x-E) hysteresis loop of a polycrystalline ferroelectric material.

2.2.2 Domain Formation

The mechanical and electrical boundary conditions of a crystal as it is cooled through the ferroelectric phase transition affects the domain structure of the crystal and

ultimately influences the dielectric and piezoelectric response (Figure 2.5) [4]. At the Curie temperature, the onset of spontaneous polarization leads to the formation of surface charges (known as the depolarization field) due to a nonhomogeneous distribution of the spontaneous polarization near the surface of the ferroelectric material. The electrostatic energy due to the depolarizing field is equal to Equation 2.7 [2].

$$W_e = \frac{1}{2}\int_v D \cdot E_o dV \qquad \text{Equation 2.7}$$

In Equation 2.7, W_e is the electrostatic energy, D is the dielectric displacement, E_o is the magnitude of the electric field, and V is the volume of the crystal. In order to minimize the electrostatic energy due to the depolarization field, free charges from the surrounding medium can compensate, however, in air this process is extremely slow. Therefore to minimize the electrostatic energy, the material forms domains such that there is a zero net polarization in a virgin sample as it is cooled[1]. The creation of domain walls, however, also has an associated energy [2]:

$$W_w = \frac{\sigma}{w_d} V \qquad \text{Equation 2.8}$$

In Equation 2.8, W_w is the domain wall energy, σ is the energy per unit area of the domain wall, V is the volume of the crystal, and w_d is the domain width. Therefore, the formation of domains is energetically favorable if the sum of both the depolarizing electrostatic energy and domain wall energy is minimized.

[1] Virgin crystals show very small pyroelectric and piezoresponse effects unless poled. Poling is the process of applying an appropriate DC field in order to align domains.

For a multi-domain crystal with a simple periodic domain structure consisting of 180^o domain walls, the electrostatic energy can be written in terms of the domains formed [10-11]:

$$W_e = \frac{A_\varepsilon w_d P_d^2 V}{t_c} \qquad \text{Equation 2.9}$$

In Equation 2.9, W_e is the electrostatic energy, A_ε is a constant dependent on the dielectric permittivity of the material, P_d is the domain's polarization, V is the volume of the crystal, w_d is the domain width, and t_c is the thickness of the crystal. Based on Equation 2.9, as the domain width decreases the crystal has a lower electrostatic energy. Thus, multi-domain crystals have lower electrostatic energy when compared to mono-domain crystals.

Domain formation also occurs due to the influence of mechanical stresses caused by mechanical boundary conditions when undergoing the ferroelectric phase transition. Both 180^o and non-180^o walls can reduce the depolarizing electric field, while only the formation of non-180^o domain walls minimize the elastic energy [12-13]. At a critical ferroelectric thickness, the reduction in the elastic energy via the formation of non-180^o domains can actually be less than the energy required to form domains. Therefore at this critical thickness, the formation of non-180^o domains is no longer energetically favorable.

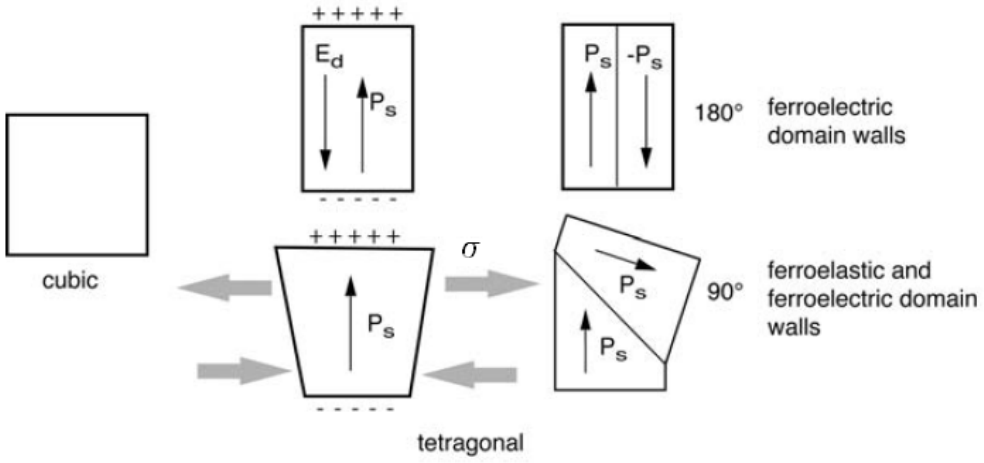

Figure 2.5: Illustration of the formation of 180° and 90° domain walls in order to minimize the effects of the depolarization field (E_d) and stress (σ) [4].

2.2.3 Intrinsic and Extrinsic Contributions

The dielectric and piezoelectric response of polycrystalline ferroelectric materials have intrinsic and extrinsic components [14]. The intrinsic component is the volume response that would be obtained in a single domain, single crystal ferroelectric (Figure 2.6a). The extrinsic component represents domain wall and phase boundary motion contributions (Figure 2.6b,c).

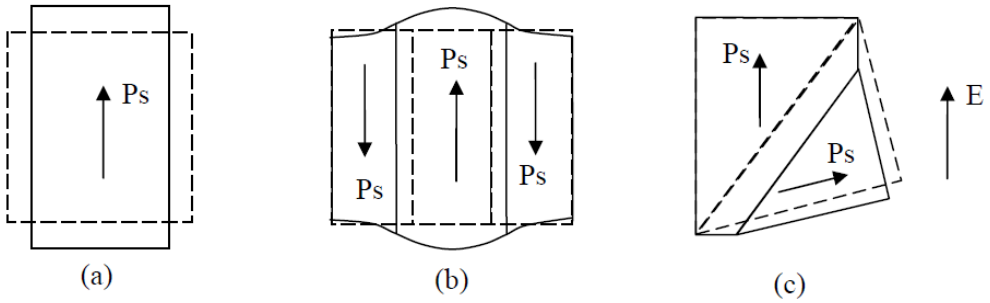

Figure 2.6: (a) Intrinsic contribution from a single domain under the application of an electric field; (b) extrinsic contribution to the dielectric response via 180° domain wall motion; (c) extrinsic contribution to the dielectric and piezoelectric response via the motion of non-180° domain wall. The dashed line represents the configuration before the application of the electric field [15].

In a ferroelectric crystal, the intrinsic and extrinsic contribution contributes to the real components of the dielectric and piezoelectric response, while only the extrinsic coefficient contributes to the imaginary part of the response (Equation 2.10 and Equation 2.11) [16].

$$\varepsilon^* = \varepsilon^{'} - j\varepsilon^{''} \quad \text{where} \quad \varepsilon^{'} = \varepsilon^{'}_{\text{int}\,rinsic} + \varepsilon^{'}_{extrinsic} \quad \text{and} \quad \varepsilon^{''} = \varepsilon^{''}_{extrinsic} \qquad \text{Equation 2.10}$$

$$d^* = d^{'} - jd^{''} \quad \text{where} \quad d^{'} = d^{'}_{\text{int}\,rinsic} + d^{'}_{extrinsic} \quad \text{and} \quad d^{''} = d^{''}_{extrinsic} \qquad \text{Equation 2.11}$$

In Equation 2.10, ε^* is the complex dielectric permittivity, $\varepsilon^{'}$ is the real component of the dielectric permittivity, and $\varepsilon^{''}$ is the imaginary component of the dielectric permittivity. In Equation 2.11, d^* is the complex piezoelectric coefficient, $d^{'}$ is the real component of the piezoelectric coefficient, and $d^{''}$ is the imaginary component of the piezoelectric coefficient.

Several experimental studies have been performed in order to distinguish the intrinsic and extrinsic contributions to the dielectric and piezoelectric response via studying frequency [17-19], temperature [16, 20], and aging time dependence [21-23]; however, all of these methods are only qualitative. Therefore, throughout this thesis the Rayleigh analysis was employed as this approach is the most versatile and only quantitative method.

2.2.3.1 AC Field Dependence of the Dielectric and Piezoelectric Response

The piezoelectric and dielectric response dependence on the AC field has three different regions: a low field region, a Rayleigh region, and a high field region (Figure 2.7). At low AC field amplitudes, the relative dielectric permittivity and piezoelectric coefficient are approximately constant (i.e. independent of the driving field), thus the dielectric and piezoelectric response increase linearly with electric field.

Although these linear descriptions are accurate at low fields with further increases in the AC field amplitude, these linear low field approximations become inaccurate. Therefore, often a threshold field (E_{th}) is reported below which the relative dielectric permittivity and piezoelectric coefficient are independent of the AC field levels [14, 24-25]. The threshold field, however, is often difficult to determine, thus it is usually defined as less than a 5% increase in the dielectric permittivity and piezoelectric coefficient with respect to low field values [26].

At intermediate fields, the relative dielectric permittivity and piezoelectric coefficient are no longer constant, thus the piezoelectric and dielectric responses are nonlinear. In order to quantify the intrinsic and extrinsic contributions, a model similar to

the classical Rayleigh law in ferromagnetics is often employed [27]. The Rayleigh law applied to ferroelectrics describes the hysteretic response of domain wall motion from one potential energy well to another position via the application of a sufficient electric field to overcome the initial energy barrier. The Rayleigh law also assumes that there is a random distribution of pinning centers that comprise the domain wall energy profile [28].

The Rayleigh law has successfully described the nonlinear dielectric and piezoelectric behavior of ferroelectric thin films [8] [29-30], bulk ceramics [28] [31-33], and single crystals [34-36] at sub-switching conditions where the real component of the dielectric (Equation 2.12) and piezoelectric coefficients (Equation 2.13) depend linearly on the applied electric field's amplitude:

$$\varepsilon' = \varepsilon'_{init} + \alpha'_{\varepsilon} E_o \qquad \text{Equation 2.12}$$

$$d' = d'_{init} + \alpha'_{d} E_o \qquad \text{Equation 2.13}$$

ε'_{init} and d'_{init} represent the field-independent terms which are dominant at low fields and represents intrinsic ionic response as well as reversible domain wall vibration and motion. The α_d and α_ε terms represent contributions from irreversible domain wall or phase boundary motion or in general any mechanism that can lead to a nonlinear and hysteretic change in the dielectric or piezoelectric response. The reversible motion involves the motion of interfaces around an equilibrium position, while irreversible motion refers to the motion of the interface from one potential energy well to another (Figure 2.8). Throughout the remainder of this thesis, α will be used to denote the irreversible piezoelectric Rayleigh parameter.

With even further increases in the electric field (i.e. high field region), domain switching occurs and the Rayleigh law no longer applies, as the field dependence is no longer linear but becomes sub or super linear.

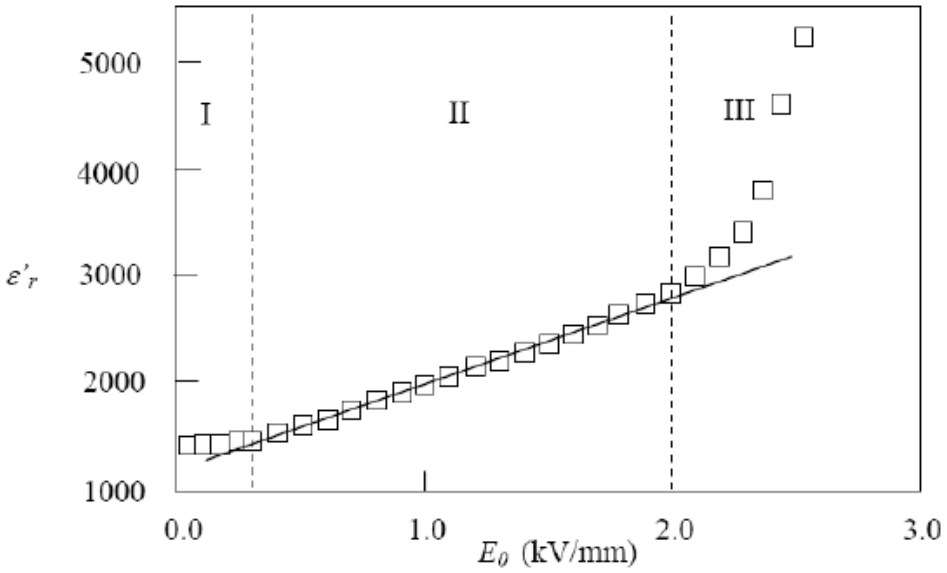

Figure 2.7: Schematic graphic representation of the AC field dependence of dielectric permittivity in bulk PZT ceramics. The low field region (I) shows a relatively constant dielectric permittivity and region (III) represents the high field region with a superlinear field-dependence of the dielectric permittivity. These two regions are separated by the Rayleigh region, where the dielectric permittivity increases linearly with the AC field amplitude [37].

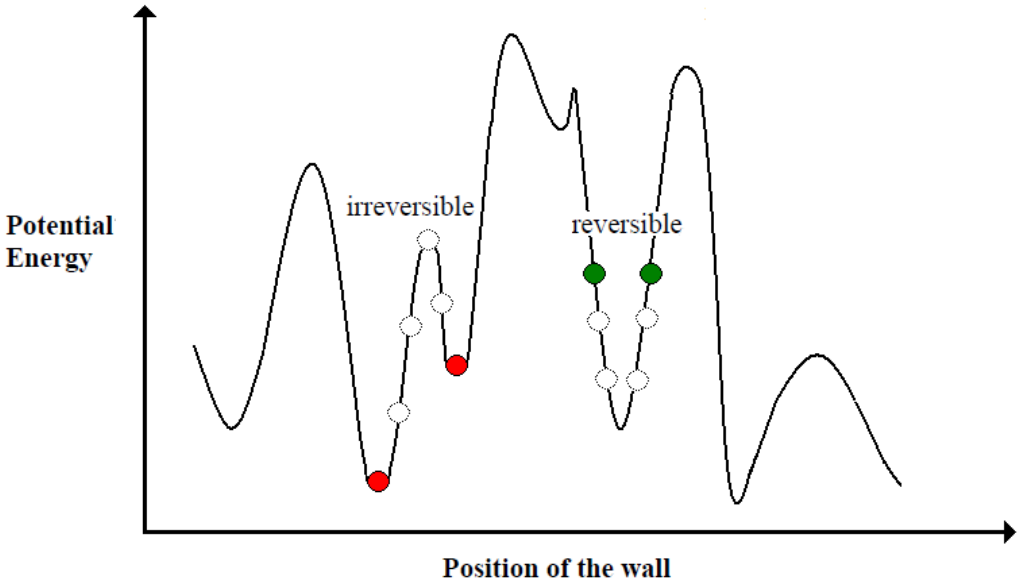

Figure 2.8: A schematic illustration of the potential energy landscape for domain wall motion with reversible and irreversible effects [33]. The dotted circles represent the motion of the walls. Ultimately, the wall will shift to minimum potential energy.

2.3 Lead Zirconate Titanate (PZT)

Although several different materials exhibit ferroelectricity, the most technologically relevant piezoelectric material is lead zirconate titanate (PZT) due to its large dielectric and piezoelectric coefficients (Table 1) [38-40].

$Pb[Zr_xTi_{1-x}]O_3$ is a solid solution of lead zirconate and lead titanate with a prototype perovskite (ABO_3) structure. Above T_c, PZT has a paraelectric cubic phase, but at room temperature it exhibits a rhombohedral ($x>0.52$), monoclinic ($0.46<x<0.52$), or tetragonal ($x<0.48$) distortions (Figure 2.9) [41].

Table 1. Piezoelectric and dielectric coefficient of various materials in thin film form [42]

Material		d_{31} (pC/N)	d_{33} (pC/N)	ε_3
PZT (composition dependent)	Ferroelectric	-94 to -274	80 to 593	425 to 1900
$BaTiO_3$	Ferroelectric	-78	190	1700
PVDF	Ferroelectric	23	-35	4
ZnO	Nonferroelectric	-4.7	12	8.2

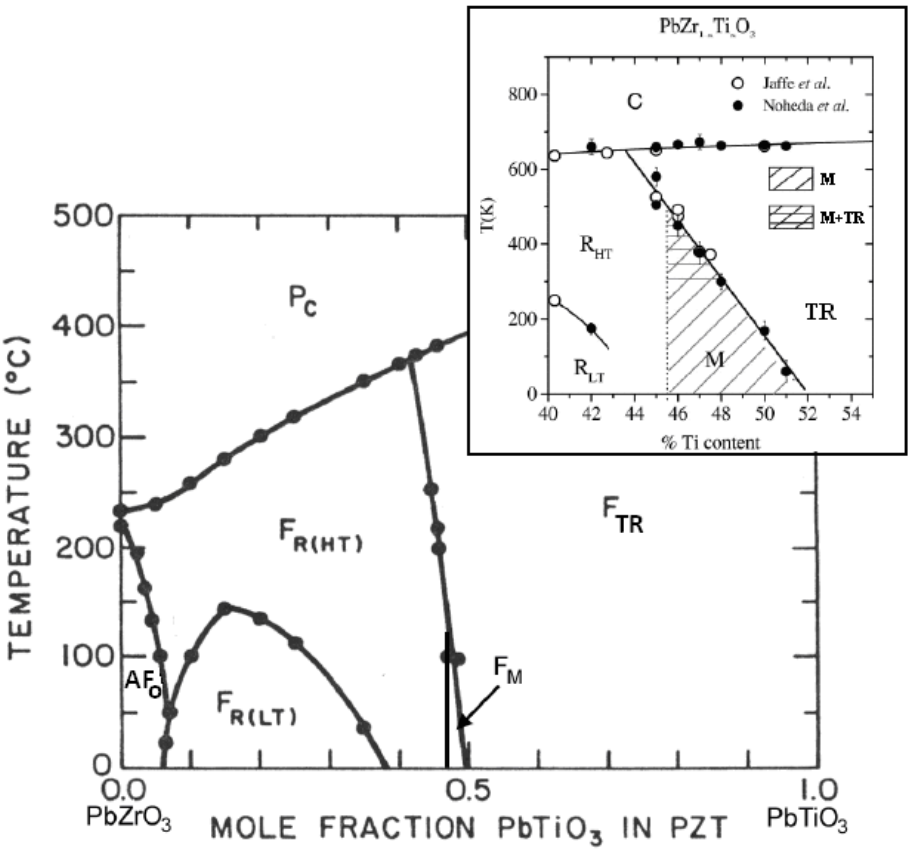

Figure 2.9: Temperature-composition phase diagram for PZT [43-44]. P_c is the paraelectric cubic phase, AF and F represent antiferroelectric and ferroelectric phases, respectively, while the subscript indicates the crystal's structure. O is orthorhombic, TR is tetragonal, M is monoclinic, and R is rhombohedral. HT and LT denote high and low temperatures, respectively. The inset provides details regarding the monoclinic phase [45].

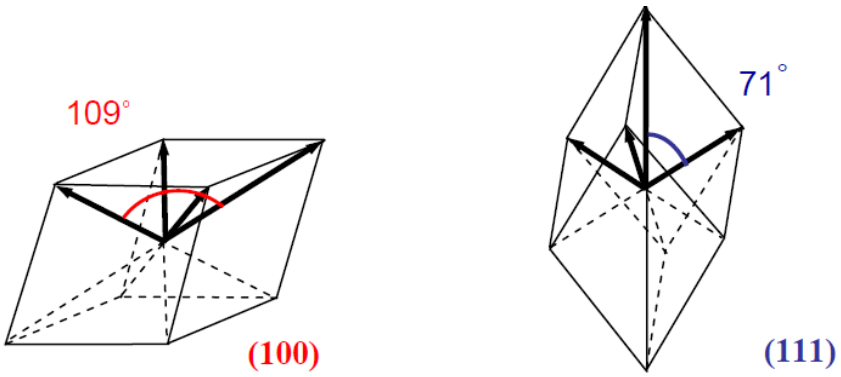

Figure 2.10: A schematic representation of the available polarization directions for (100) and (111) oriented rhombohedral crystals [15].

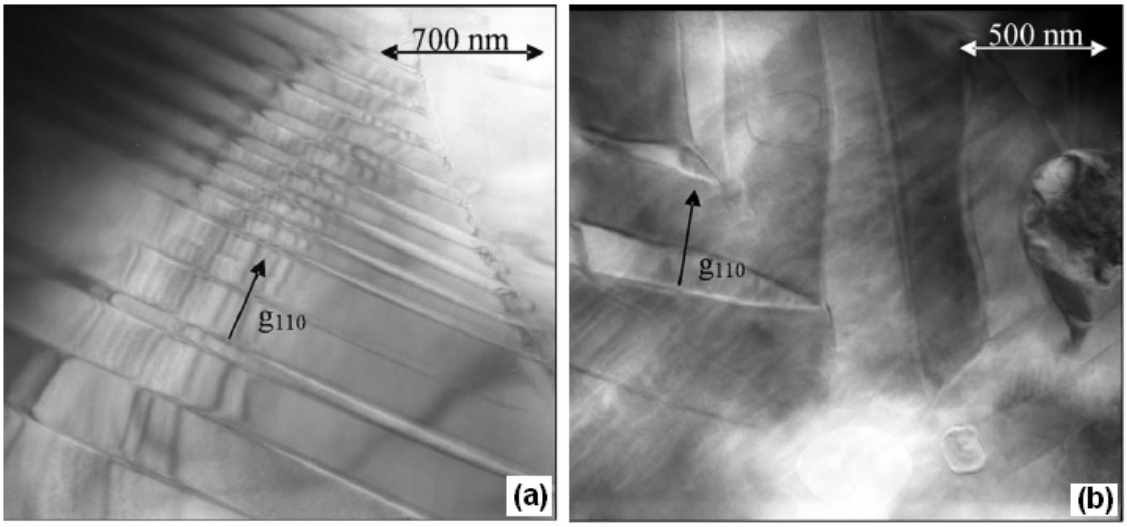

Figure 2.11: Bright field images of domain structure observed for undoped $Pb[Zr_xTi_{1-x}]O_3$ with (a) x=0.4 (tetragonal) and (b) x=0.6 (rhombohedral) [46].

The tetragonal phase distortion has six degenerate spontaneous polarization directions along the principal axes forming 90^o and 180^o domain walls. Rhombohedral

crystals have eight degenerate spontaneous polarization directions along body diagonals resulting in 71°, 109°, and 180° domain walls. Figure 2.10 demonstrates the available polarization directions for rhombohedral crystals with two different orientations, and Figure 2.11 shows the domain structures formed in undoped PZT observed via TEM (transmission electron microscopy).

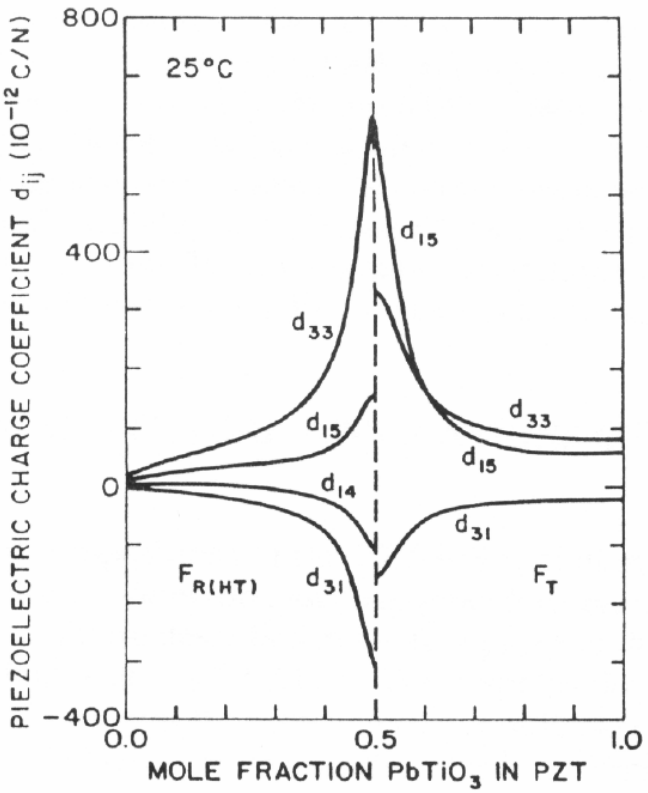

Figure 2.12: Theoretically calculated piezoelectric properties of PZT as a function of $PbTiO_3$ content [47].

All domain walls that are not 180^o domain walls (i.e. 71^o, 90^o, and 109^o) are collectively known as non-180^o domain walls. 180^o domain wall motion mainly contributes to the dielectric response of the ferroelectric material [15] and are purely ferroelectrically active (only excited via electric fields). Non-180^o domain wall motion contributes equally to the dielectric and the piezoelectric response and is both ferroelectrically and ferroelastically active (i.e. excited via mechanical means) [13]. Studies have shown that the piezoelectric coefficients rapidly increase at the morphotropic phase boundary (MPB)[2] corresponding to x~0.5 [38, 48-53]. This increase is in part due to an increased availability of polarization directions from both the rhombohedral and tetragonal distortions, which allows for better alignment of the ferroelectric dipoles during poling (application of sufficient DC electric field in order to align domains) [43]. Figure 2.12 shows the dependence of the piezoelectric coefficients of PZT as a function of $PbTiO_3$ content with peaks corresponding to the MBP composition [47].

2.4 Nanoscale Ferroelectric Applications

High aspect ratio piezoelectric materials such as PZT have a wide range of applications at the micron and sub-micron scale, specifically as actively tunable photonic crystals [54-56], terahertz emitters [57-58], ultrasound transducers [59-61], and energy harvesters [62-67].

[2] The morphotropic phase boundary is nearly temperature independent in PZT.

Photonic crystals refer to materials that have a periodic refractive index that can guide the propagation of electromagnetic waves. In order to steer electromagnetic waves, the photonic crystals must have repeating structures of high- and low- ε materials with dimensions of fractions of the wavelength of the electromagnetic waves [68]. The use of ferroelectric materials allows for tuning of the dielectric permittivity through the ferroelectric response as well as the change in the aspect ratio of the material through the piezoelectric response, thus allowing for active control of the refractive index of the periodic structures.

Terahertz waves can penetrate organic materials and fabrics but are blocked by metals and heavy elements, thus allowing for potential applications in security screening and biological imaging. The important material parameters for THz emitters are a large gradient in charge density, a large piezoelectric coupling constant, and reasonable carrier mobility [57]. Previously, only free-electron laser sources [69] and optical pumps [70] have been able to generate terahertz pulses; however, recent studies have been performed that demonstrate THz emission from PZT microtubes [58], thus allowing for inexpensive, lightweight, and robust devices activated by FE switching under applied electric field.

Ultrasound devices use piezoelectric materials as transducers and sensors to emit and detect ultrasonic waves, respectively. The ability to produce high resolution images is dependent on the frequency of the emitted sound waves, which is directly correlated to depth penetration and inversely correlated to image resolution. High aspect ratio sub-micron-sized piezoelectric materials provide imaging capability for low depth penetration tissues such as the cornea and hypodermis [60]. Also, 1-3 patterned piezoelectrics[3]

[3] 1-3 denotes the connectivity of the phases present. In this case, a ceramic-air composite is being discussed with the ceramic connected only in 1 dimension and the air in 3 dimensions.

exhibit a lower impedance than full piezoelectric ceramics allowing for more efficient impedance matching with organic tissues, therefore minimizing the reflection of sound waves back to the detector at the interface [71].

Piezoelectric materials can also be used as a means of transforming mechanical vibrations or forces into electrical energy. Sources of biomechanical vibrations include human activities such as expansion and contraction of the rib cage during breathing [66] and locomotion [67]. The key element for creating commercially successful "bio-energy" scavenging devices is to develop unobtrusive, flexible, and low weight harvesting systems. The energy harvesting capability of a piezoelectric device depends on the material's piezoelectric coefficients and the structure's geometry. Piezoelectric nanotubes are extremely attractive for energy harvesting applications due to their flexibility, low weight, and fail safe mode (if a single nanotube fails the device is still capable of harvesting energy).

2.5 Nanoscale Patterning of Ferroelectric Materials

The major challenge in the technological advancement of the aforementioned applications is the limited manufacturing processes available. The two fundamental approaches for sub-micron patterning of piezoelectric [4] materials are top-down and bottom-up. A top-down manufacturing approach includes starting with larger systems and creating smaller ones by material removal, for example by focused ion beam milling or wet etching (Figure 2.13). Typically focused ion beam milling is preferred to wet etching due to the latter's isotropic nature and poor sidewall definition; however,

[4] These two fundamental approaches for sub-micron patterning are true for all materials.

problems also exist with focused ion beam milling. First, the high energy of the incoming beam can damage the PZT surface and hence degrade the ferroelectric and piezoelectric response [72-73]. Second, this processing method is a serial approach with slow throughput capabilities and high cost.

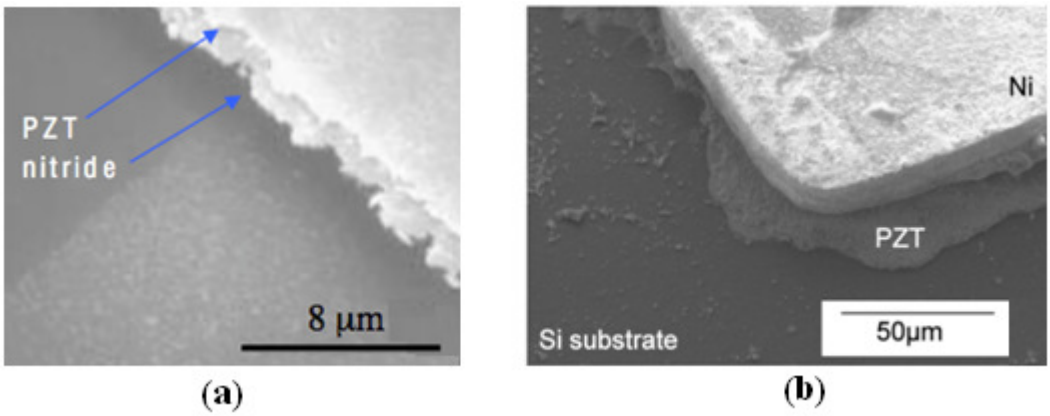

Figure 2.13: Edge definition of PZT structures with (a) wet etching using an HCl and HF mixture [74] and (b) ion beam (or dry) etching [75].

In bottom-up approaches, structures are built from smaller building blocks. There are several different bottom-up approaches that have been reported in literature for patterning piezoelectric materials; however, they are either limited to the creation of low aspect ratio nanodots and nanodisks or high aspect ratio tubes and wires without site specific registry. These are discussed in detail in the following sections.

2.5.1 Low-Aspect Ratio Ferroelectric Patterning Methods

W. Lee et al. developed a method to create low aspect ratio PZT structures via pulsed laser deposition of PZT onto an ultrathin anodic aluminum oxide (AAO) mask (Figure 2.14a) [76-77]. In a typical anodization process, only honeycomb-like structures of self-ordered arrays of oxide nanopores are created (Figure 2.14b). Therefore, the density and location of the patterned piezoelectric material is limited by the AAO mask. Although the pore density can be tuned [77-79], the increased number of processing steps is undesirable. In addition, the aspect ratio of the piezoelectric material is limited due to the mask lift-off process, and sub-100 nm sized PZT nanodots exhibited structural instability (Figure 2.14c).

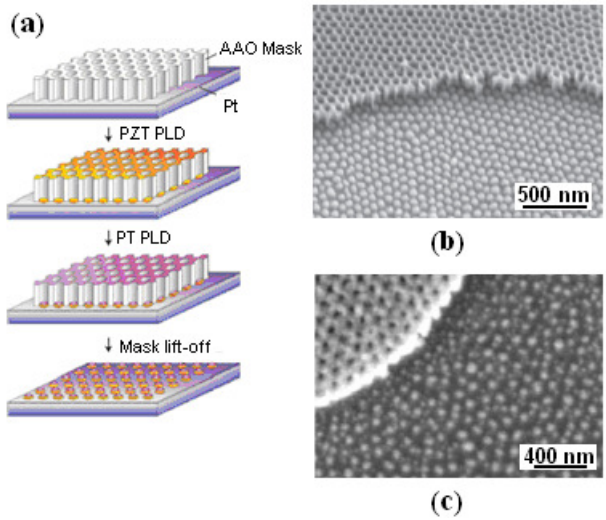

Figure 2.14: (a) Schematic illustration of the processing method used to create PZT nanodots including: creation of AAO mask, deposition of PZT via PLD, deposition of PT via PLD, and mask lift-off; (b) SEM image of 120 nm-wide PZT nanodots and the AAO mask visible at the top of the image; (c) SEM image illustrating structural instability of PZT nanodots, when attempting to create structures with lateral dimensions below 100 nm [76].

The major fabrication challenge of the above method is the creation of the ultrathin AAO mask. The authors reported that processing of the ultrathin masks led to mechanical deformations such as folding, cracking, or ripping. These issues were overcome by performing a two step anodization process in which polystyrene was used for mechanical consolidation; however, the processing required four separate etch steps with increasing handling requirements. A similar approach for creating nanodots was also developed by I. Vrejoiu et al. using gold membrane stencils [80]; however, it did not provide any major advantages in terms of handling, patterns created, or cost.

H. Han et al. also developed a bottom-up method to create piezoelectric nanodisks [81]. Laser interference lithography (LIL) was used to pattern photoresist. The pattern was subsequently transferred to a SiO_2 mask layer and the underlying anti-reflection coating layer (Figure 2.15a). The photoresist was then stripped, and PZT was deposited via pulsed laser deposition (PLD). A lift-off process is performed to remove the anti-reflection layer (and SiO_2 mask), and subsequently the PZT was crystallized (Figure 2.15b). The numerous steps required and the limitation of PLD in creating only "flat" (i.e. low aspect ratio) structures due to difficulty in infiltrating into high aspect ratio holes limits the technological use of the method for some of the aforementioned applications. Furthermore, only specific periodic structures can be produced via LIL patterning[5] [82].

[5] Although LIL patterning is employed in this report, other patterning approaches such as electron beam lithography could be used.

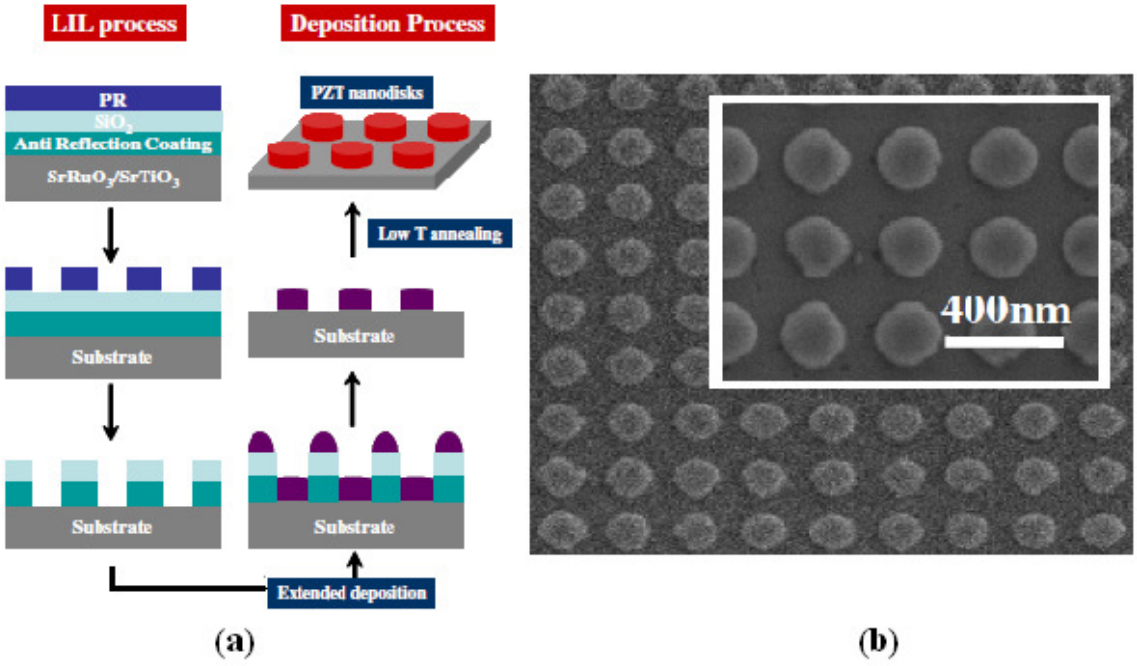

Figure 2.15: (a) Schematic representation of the processing steps used to create PZT nanodisks via LIL developed by Han et al. [81]. The resist is spun-coated onto the substrate and patterned via LIL. Subsequently, the pattern is transferred to the SiO_2 and anti-reflection coating via reactive ion etching. PZT is then deposited via PLD. A lift-off process is subsequently used to remove the anti-reflective coating (and SiO_2 mask). PZT nanostructures are crystallized in a PbO atmosphere; (b) SEM image of the resulting PZT nanostructures.

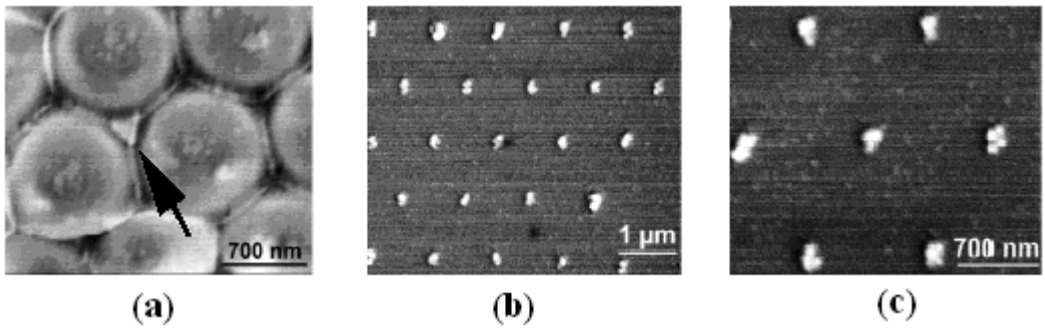

Figure 2.16: SEM micrograph of triangular-shaped nanostructures located at the interstice of the three adjoining shell structures, located at the arrow tip; (b) SEM micrograph of patterned $BaTiO_3$ nanostructures after lift-off of latex spheres; (c) high-magnification image of the nanopattern [83].

Ma et al. also developed a lift-off technique for patterning ferroelectric structures using a monolayer of latex spheres as the stencil mask (Figure 2.16) [83-84]. Although this method eliminates the etching steps necessary to create the mask in the aforementioned lift-off procedures, the size of the structures were still limited in aspect ratio with a height to width ratio of 1:6.4.

Yet, another method for creating low aspect ratio nanoislands includes depositing an ultrathin film of PZT precursor by spin coating followed by drying [85]. The sample is then annealed at temperatures greater than 600^{o}C in a PbO environment. During this high temperature processing step, the amorphous film forms into crystallized islands. The formation of these islands is driven by energy considerations. The total surface and interface energy is minimized by introducing surfaces of lower energy resulting in truncated pyramid structures. The misfit strain between the substrate and the deposited material ultimately determines the final distribution of the structures. A large misfit strain resulted in small truncated structures, whereas as small misfit strain resulted in irregular shapes and a larger size distribution. The disadvantage of this method is that only structures with truncated pyramid shapes can be produced. Also, the structures exhibited interfacial misfit dislocations between the substrate and the epitaxial structure, which is detrimental for its ferroelectric properties [86-88].

Nonomura et al. used a similar approach for self-assembled $PbTiO_3$ nanoislands using metalorganic chemical vapor deposition [89]. By varying the substrate's orientation, the shape of the resulting structure changed. For instance, triangular-shaped, triangular-prism-shaped, and square-shaped structures were produced on Pt/$SrTiO_3$ (111), (101), (001), respectively (Figure 2.17). The disadvantage of this approach is the

epitaxial growth requirement and the inability to vary the $PbTiO_3$ structure's shape on a single substrate or control their location.

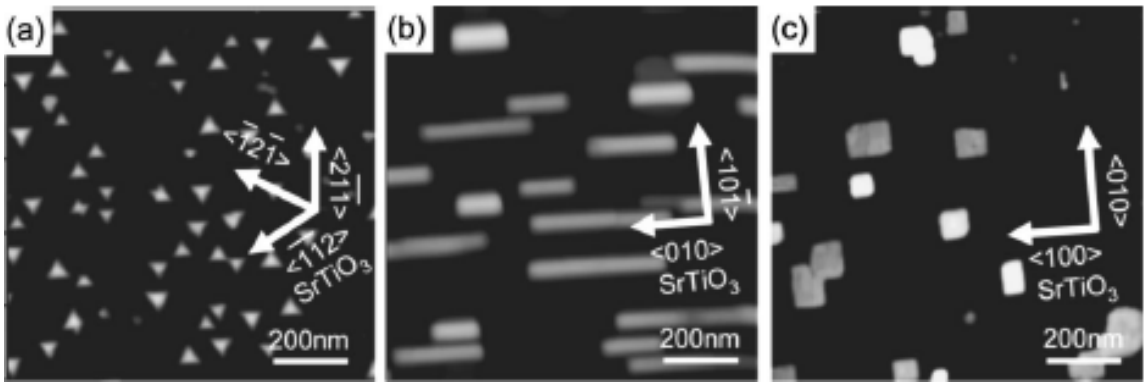

Figure 2.17: AFM images of self-assembled $PbTiO_3$ nanoislands prepared on (a) $Pt/SrTiO_3$ (111), (b) $Pt/SrTiO_3$ (101), and (c) $Pt/SrTiO_3$ (001) [89].

Alexe et al. also developed a method for patterning low aspect ratio nanosized ferroelectric memories (Figure 2.18a,b) [90]. In this approach, metalorganic precursors are deposited on a substrate via spin coating and chemical reactions are induced via irradiation with an electron beam. The solubility of the exposed region is altered such that submerging the substrate in the appropriate solvent causes the unexposed regions to dissolve. The disadvantages of this method include slow throughput and only low aspect ratio structures are produced. In an alternative ferroelectric memories fabrication method based on a parallel processing technique, Harnagea et al. fabricated arrays of PZT cells by imprinting precursor sol-gel layers via nanoimprint lithography (Figure 2.19a,b) [91]. Although this method improves throughput, the size of the structures are limited to low

aspect ratios with a width of 350 nm and height of 50 nm. Another major drawback includes adhesion of the sol-gel to the mold.

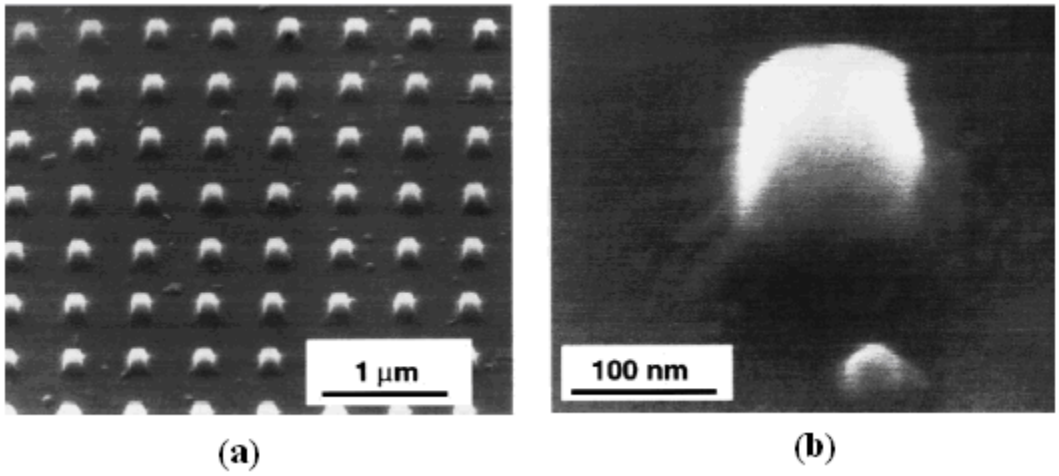

Figure 2.18: (a) SEM of a PZT cell array after patterning via EBL and annealing and (b) higher magnification SEM image of a 100 nm PZT cell on Nb doped $SrTiO_3$ substrate [90].

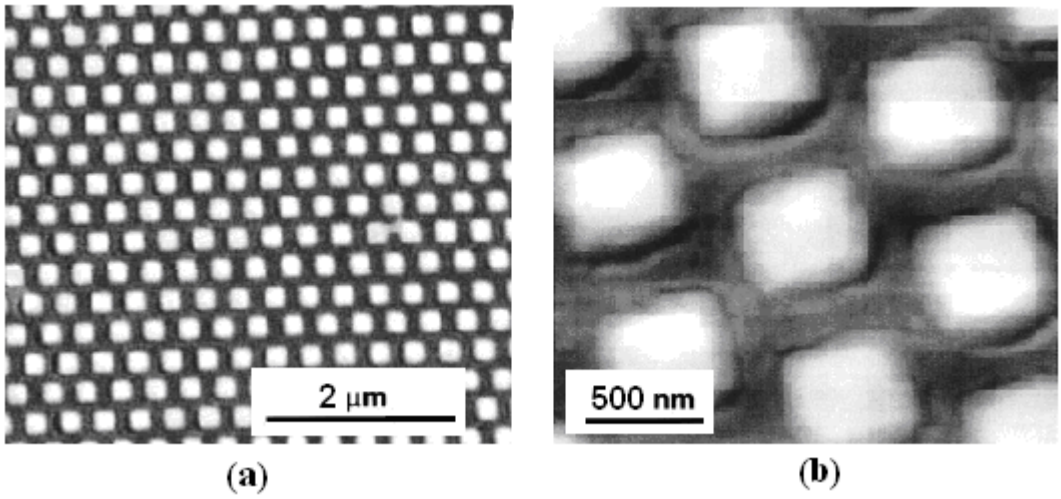

Figure 2.19: (a) AFM topography image of an imprinted crystallized array of ferroelectric PZT cells on Nb doped $SrTiO_3$ substrate and (b) higher magnification AFM topography image [91].

2.5.2 High-Aspect Ratio Ferroelectric Patterning Methods

To manufacture PZT nanowires, J. Wang et al. [92] modified a hydrothermal approach developed by Cheng et. al [93]. In this approach, non-ferroelectric phase PZT wires were fabricated via a chemical means and converted to perovskite phase PZT wires via annealing in a PbO atmosphere at 600^{o}C for 20 min. The disadvantage of this method includes little control over the diameter and length of the wires and random location and orientation on the substrate.

S. Xu et al. also developed a method for creating single-crystal nanowire arrays using hydrothermal decomposition (Figure 2.20a) [94]. The advantage of this approach compared to the previous method is the ability to fabricate vertically aligned nanowires; however, there is still limited control of the length of the wires created and no site-specific registry. In addition, this method has epitaxial growth requirements.

Bharadwaja et al. also created vertically aligned microtubes via PZT sol-gel vacuum infiltration into pores of Si hard-molds (Figure 2.20b) [95]. The sidewalls of the resulting PZT nanotubes, however, exhibited ripples due to scallops created during Si etching of hard-molds using the Bosch process[6].

[6] The Bosch process is an etching procedure to create nearly vertical sidewalls via alternating repeatedly between two modes: 1) nearly isotropic plasma etch (often SF_6 is used for silicon) and 2) deposition of a chemically inert passivation layer (for instance, C_4F_8). During etching, the passivation layer protects the sidewalls of the trench, while the directional ions bombard and etch the passivation layer at the bottom of the trench.

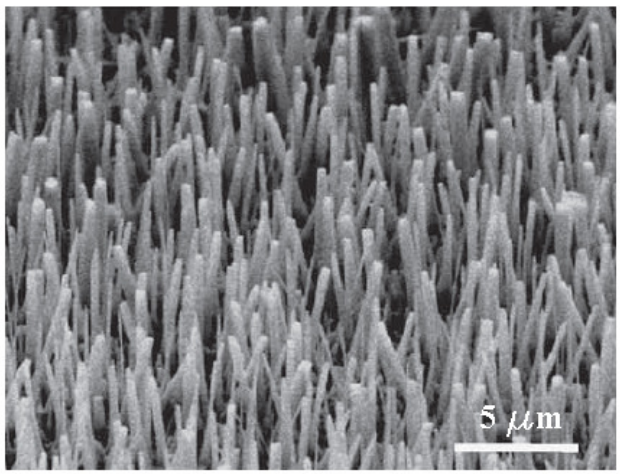

(a)

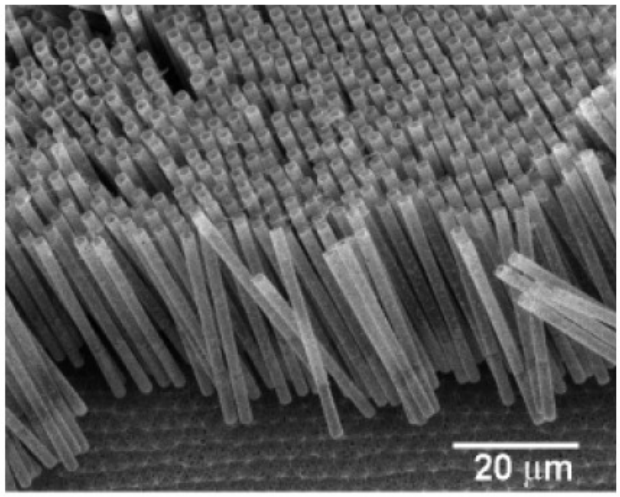

(b)

Figure 2.20: (a) SEM image of the epitaxially grown PZT nanowires on an Nb-doped STO substrate by hydrothermal decomposition [94]; (b) SEM image of released PZT microtubes created using Si hard templates [95].

Scott et al. used a similar approach to create PZT microtubes via infiltration of a metalorganic decomposition (MOD) PZT precursor solution into Si hard molds (Figure 2.21) [57]. The hard molds were created by etching n-type phosphorus doped Si wafers [96]. The pore diameter was determined by the doping density. For example, a phosphorus doping density of $1x10^{15}cm^{-3}$ resulted in 2 μm-diameter holes. After

infiltration of the hard molds, the PZT were partially exposed from the Si templates via polishing to remove the excess PZT layers crystallized on top of the Si molds, followed by etching in a 30 wt % KOH solution at room temperature. The major drawback for the use of these Si hard molds to manufacture PZT microtubes is the formation of secondary phases due to chemical reactions between the ferroelectric (PZT) and template walls (Si). The non-ferroelectrically-active secondary phases can reduce the overall piezoelectric response of the nanostructures [97]. Furthermore, the height and diameter of the holes will both depend on the doping of the Si and therefore cannot be independently controlled beyond a certain aspect ratio.

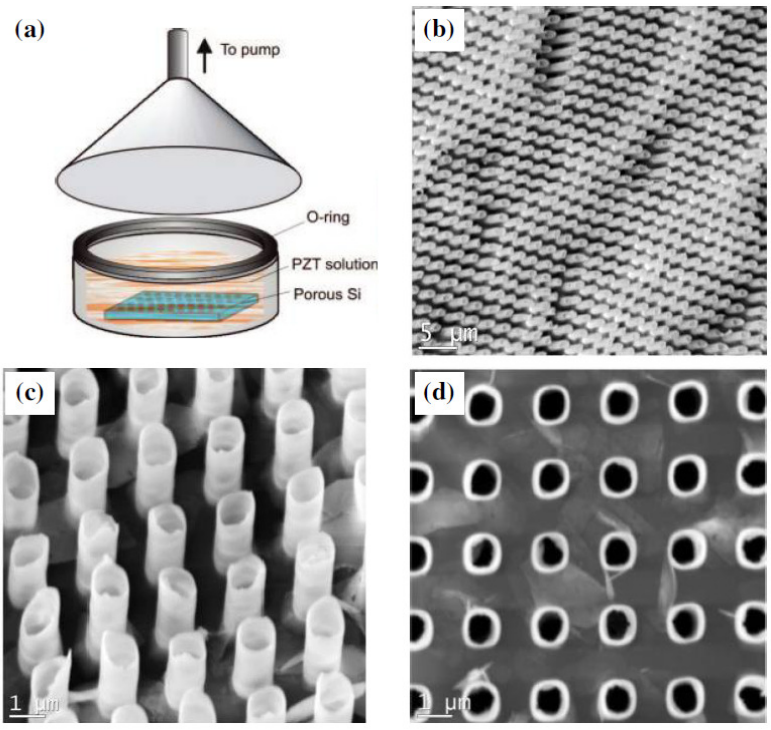

Figure 2.21: (a) Schematic of the fabrication process of PZT tubes in the Si hard mold. (b) Scanning electron microscopy images of PZT nanotube array partially exposed from the Si substrate and (c) detailed SEM image. (d) Top-view SEM image demonstrating ~45 nm PZT wall tube thickness and 1μm diameter.

In summary, current bottom-up processing methods used to pattern piezoelectric materials are either restricted to low aspect ratio patterning methods such as nanoimprint lithography, electron beam irradiation, lift-off, and shadow mask processing; or for creation of high aspect ratio structures, are limited to hydrothermal processing and infiltration of Si hard-molds, which allow for limited, if at all, control of the location of the patterned piezoelectric material, therefore not satisfying alignment requirements for future device fabrication.

2.6 Nanoscale Phenomena

As previously discussed in section 2.4, a wide range of applications would be enabled with the capability for patterning ferroelectric materials at micron and sub-micron scales. However, the use of ferroelectric materials for the aforementioned applications depends also on the ability to maintain a stable ferroelectric phase as devices continue to miniaturize. Additionally, extrinsic size effects can also reduce the effective piezoelectric response as the material's dimensions decrease, thus reducing the technological potential of ferroelectric materials.

Size effects in ferroelectrics are both intrinsic and extrinsic in nature. Intrinsic size effects are limited to thicknesses of a few nanometers and have been extensively studied through theoretical and experimental work in ferroelectric thin films. Conversely, extrinsic size effects have been much less studied primarily due to fabrication challenges in producing ferroelectric nanostructures. Specifically the inability of creating structures with prescribed aspect ratios and various boundary conditions, without surface damage to the ferroelectric material, limits the capability of investigating factors influencing the

extrinsic contribution to the piezoelectric response such as substrate clamping and lateral constraint.

2.6.1 Substrate Clamping

Literature reports indicate a significant reduction in the dielectric and piezoelectric response as the ferroelectric film thickness decreases. The disparity in the response of ferroelectric thin films with thicknesses of a few microns and below with respect to bulk ceramics has been attributed to the clamping of the films to the substrate. Most thin films are under appreciable levels of in-plane stress due to lattice mismatch between the film and the substrate, as well as differences in thermal expansion coefficients during crystallization. Ferroelastic domains form to help reduce the elastic and electrostatic energy associated with the processing stresses as well as the ferroelectric transition of the material. However, the in-plane residual stresses also act as a pinning source for non-180º domain wall motion.

In bulk ferroelectric ceramics at room temperature, domain wall and phase boundary motion are responsible for up to 80% of the total piezoelectric response; however, substrate clamping in ferroelectric thin films can largely reduce the overall piezoelectric response due to a reduction in contributions from non-180º domain wall motion [1]. Thus, for continued miniaturization of ferroelectric devices with large piezoelectric response, a more extensive understanding of non-180° domain wall motion as affected by substrate clamping is required.

In order to investigate substrate clamping in ferroelectric thin films, Bastani et al. studied extrinsic contribution to the dielectric and piezoelectric response for polycrystalline, (100)-oriented PZT films with thicknesses ranging from 20 nm to 260 nm [98]. The films were prepared by spin-coating a sol-gel precursor solution onto platinized Si substrates, followed by thermal treatment. The thermal treatment was adjusted such that films with similar grain sizes were produced. The study suggested the existence of a critical film thickness (~50 nm) below which extrinsic contributions were suppressed as evident via an ~50% reduction in the piezoelectric response.

In an attempt to determine the amount of clamping in nanostructures rather than films, Lee et. al calculated the degree of strain relaxation of epitaxially grown $PbTiO_3$ (a purely tetragonal ferroelectric thin film) as a function of scaling ratio (lateral size to height) via finite element analysis [99]. The theoretical calculations suggested that the strain relaxation of these films is strongly dependent on the scaling ratio of the structure and not just the lateral dimension or film thickness alone. As the scaling ratio decreased below 20, the in-plane strain was found to drop drastically based on finite element modeling (Figure 2.22). This reduction of in-plane strain could also result in a change in the non-180° domain wall structure as non-180° domain walls form to reduce residual stress. However, the final domain structure will depend on the overall electrostatic and elastic energies as well as the geometry of the samples.

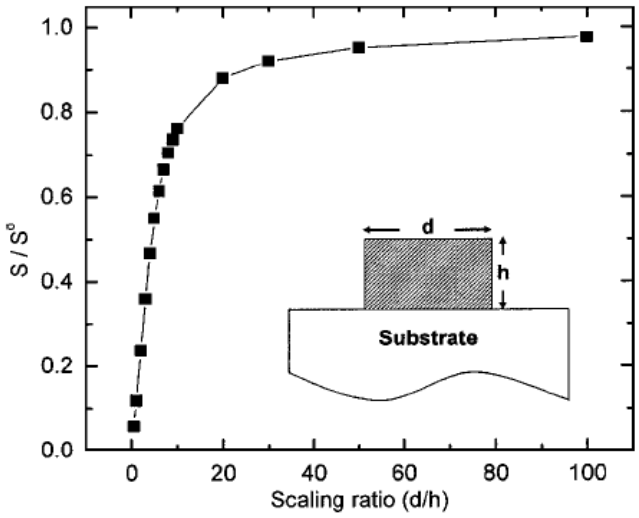

Figure 2.22: Finite element simulation results of the strain relaxation in epitaxial $PbTiO_3$ films patterned into discrete islands on an MgO (001) single crystal substrate. S and S^0 represent the volumetric average in-plane strains in the patterned island and continuous films, respectively [99].

To experimentally investigate substrate clamping in nanostructures, Nagarajan et. al patterned epitaxial 20/80 PZT films via focused ion-beam milling and measured the polarization vs. electric field (Figure 2.23a). Results from the study suggested enhanced contribution of non-180^o domain wall motion for the 1 μm^2 island structures with 100 nm thickness when compared to continuous films with similar thickness (Figure 2.23b) [100]. Bühlmann et al. also observed a steep increase in the piezoelectric response for 200 nm epitaxially grown 40/60 PZT films on Nb-doped $SrTiO_3$ with patterned lateral sizes below 200 nm (Figure 2.24a-c) and proposed that this increase was due to a reduction in residual stress, which ultimately resulted in a change in the domain configuration i.e. elimination of *a*-domains [101]. In a tetragonally-distorted ferroelectric material, *a*-domains are domains with polarization parallel to the substrate (i.e. the out of plane lattice parameter corresponds to *a*), while *c*-domains are domains with polarization

direction perpendicular to the substrate (i.e. the out of plane lattice parameter corresponds to *c*). Figure 2.25 is a schematic illustration of the three possible domain configurations for tetragonal epitaxial thin films on $SrTiO_3$ (STO) substrates. The presence of *a*-domains reduces the overall piezoresponse. By patterning epitaxial films, the tensile, biaxial stress, developed in the film due to the thermal expansion coefficients' mismatch and spontaneous ferroelectric strain, can be released.

For both of the aforementioned experiments, an increase in the piezoresponse was observed by nanoscale patterning of the ferroelectric material. However, a quantitative measure of the enhancement in the extrinsic contributions to the piezoelectric response due to a reduction in clamping was impossible to determine because of damages introduced in the surface layer of the ferroelectric material during etching of the structures. Thus, the research conducted herein focuses on studying substrate clamping effects in nanostructures created via a manufacturing scheme that does not require etching.

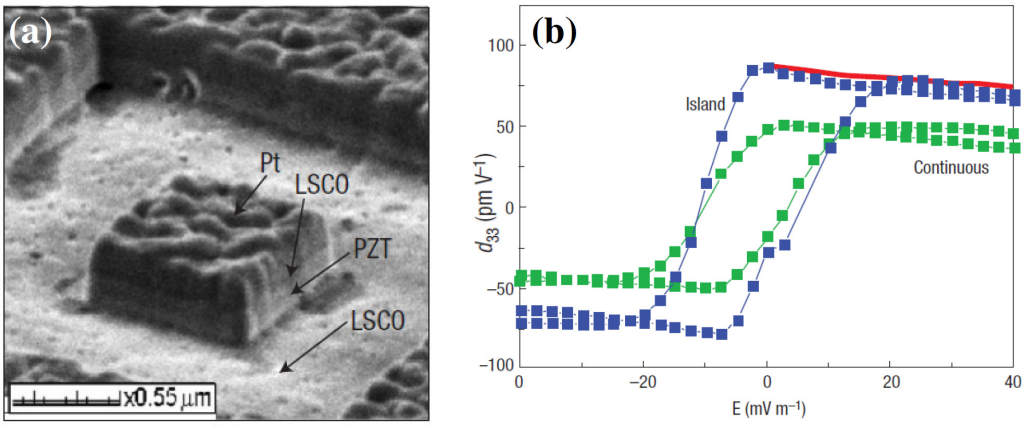

Figure 2.23: Piezoelectric loops for the island and continuous film. The red line is the theoretically predicted single crystal, single domain curve [100].

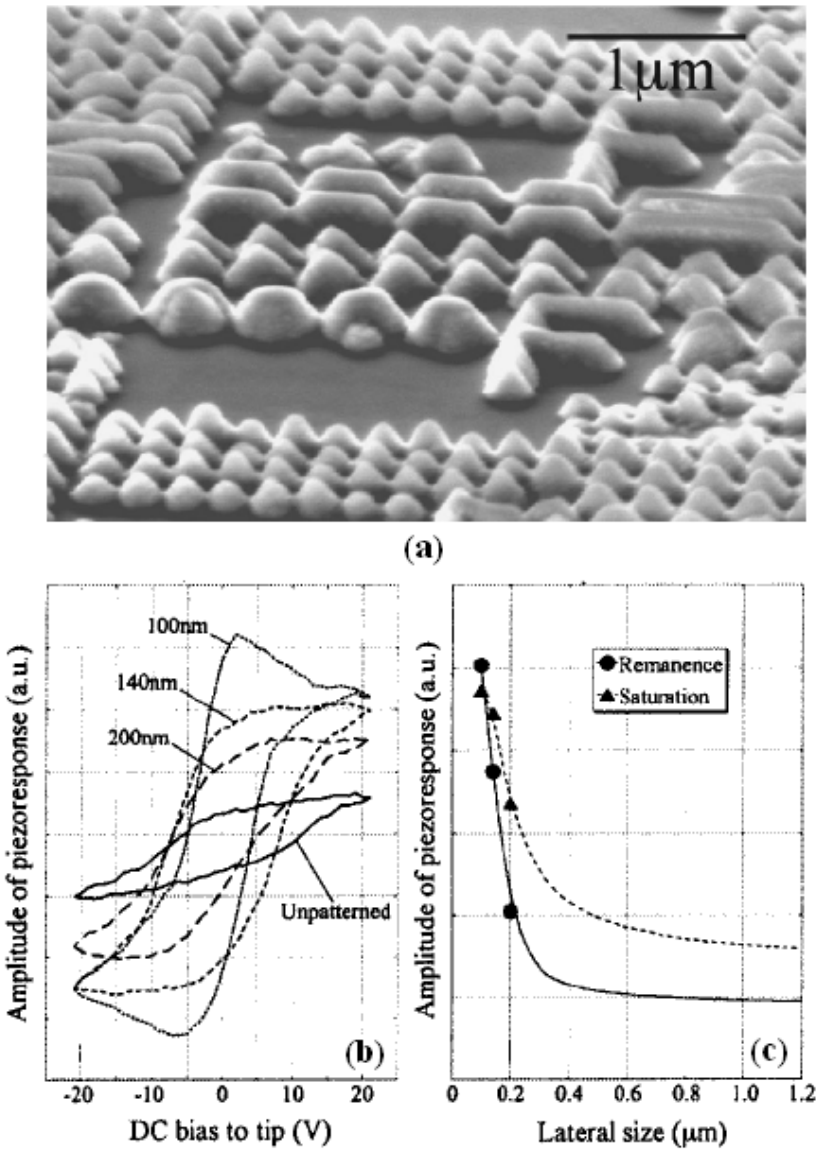

Figure 2.24: (a) SEM image showing PZT islands with lateral size in the range from 100 nm to continuous film; (b) piezoresponse-electric voltage loops demonstrating increased piezoelectric response with a decrease in lateral size; (c) remanent piezoresponse and saturation as a function of lateral size of the PZT island [101].

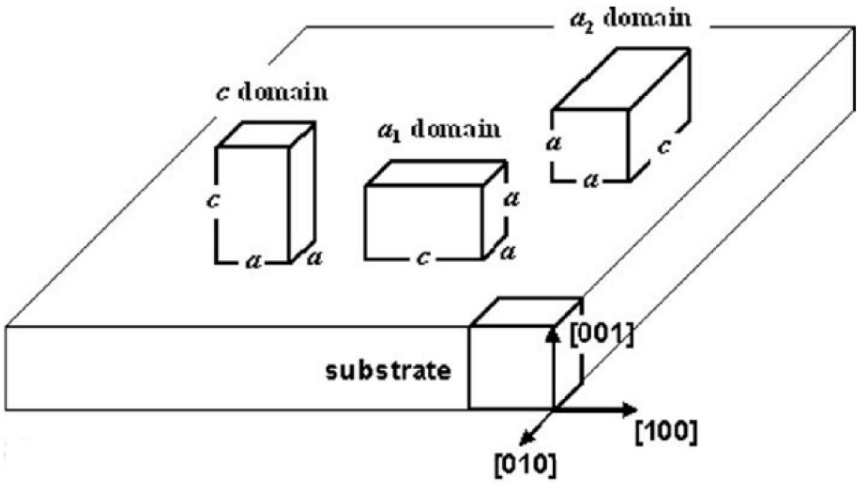

Figure 2.25: Schematic illustration of the types of domains formed in tetragonal epitaxial thin films on $SrTiO_3$ substrates [102].

2.6.2 Lateral Constraint

Clamping to the substrate is not the only factor that can cause a reduction in the piezoelectric response: lateral constraint can also affect the piezoelectric response of a ferroelectric material due to reduction in non-180° domain wall motion. Most studies have focused to date on substrate clamping; however, when patterning structures using focused ion-beam milling or dry etching the lateral constraint of the material is also being reduced. In order to study the effect of different types of clamping (both substrate clamping and lateral constraint), Ryu et al. created free-standing films, islands[7], and fully clamped films with 10 μm thickness [103]. The continuous film is clamped by the substrate and also by the inactive area of the film, the island structure has only substrate clamping, while the freestanding film only has lateral clamping from inactive area

[7] Island's diameter was ~500 μm.

(Figure 2.26a). The island structures showed ~19% increase in the dielectric permittivity when compared to the clamped film, and the freestanding structure demonstrated ~35% increase (Figure 2.26b). These results suggest that substrate clamping is the dominate factor effecting electrical properties in ferroelectrics when compared to other types of clamping; however, lateral constraint also has an important effect (reduction) on the dielectric response of FE structures.

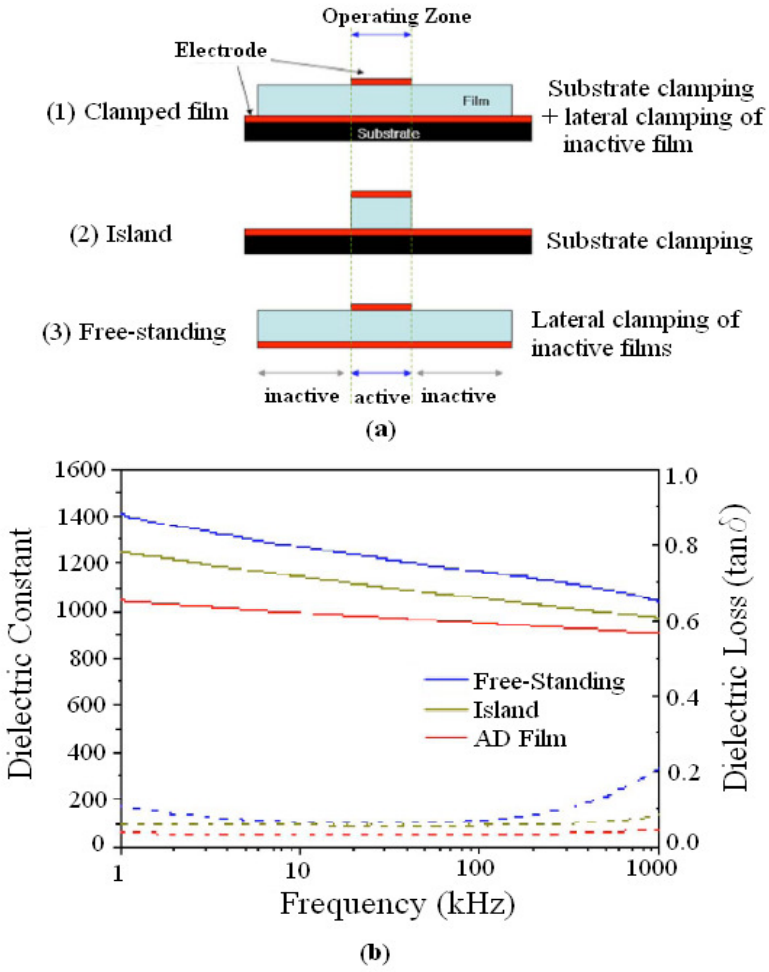

Figure 2.26: (a) Schematic representation of clamped, island, and freestanding films configurations, illustrating clamping arising from the substrate and from the lateral, inactive volume of the film; (b) frequency-dependence of the dielectric permittivity and loss for clamped, island, and freestanding PZT thick films [103].

2.6.3 Ferroelectric Size Effects

The influence of size on the properties of ferroelectric materials is a crucial factor in determining the extent to which these materials can be implemented into future applications at small scale. Many experimental efforts regarding size effects in ferroelectrics have focused on studying the phase transition in ferroelectric powders. Typically powders are synthesized by chemical routes or milling procedures which produces residual strains. In order to remove defects produced during manufacturing, the powders are often also post-processed annealed; however, annealing can lead to an increase in particle size. Therefore, one of the limitations of this approach is the difficulty in controlling the size of the powders without varying material properties. Furthermore, characterizing size effects is extremely challenging as methods for determining the dielectric and piezoelectric properties of particles are not well developed. Despite the above limitations, the critical size for $PbTiO_3$ powders was calculated to be on the order of 5-15 nm via measuring the variation of tetragonal distortion (c/a) lattice parameters[8] as a function of particle size and extrapolating to a tetragonal distortion of unity [104]. Ishikawa also determined the critical size of $PbTiO_3$ to be the same order of magnitude via Raman-scattering measurements[9] [105].

Because of the aforementioned challenges for measuring size effects in particles, thin film investigation has become an extremely attractive platform. In thin film ferroelectrics, size effects are both intrinsic and extrinsic in nature. For instance, intrinsic size effects result in reduction in the ferroelectric transition temperature, while extrinsic

[8] Lattice constants a and c were calculated from (100) and (001) reflections respectively via XRD measurements.

[9] The frequency (ω_s) of the soft E(1*TO*) mode vanishes ($\omega_s \rightarrow 0$ as $T \rightarrow T_c$).

size effects result in changes in domain population and mobility of domain walls [106]. Difficulty in determining size effects in thin films arises due to the inability of separating true size effects from other factors that change with film thickness such as microstructural heterogeneities, variations in crystalline quality, and mechanical stresses imposed on the film by the substrate [107]. Both microstructural heterogeneities and variations in crystalline quality are mostly size independent and can be improved by altering the processing method; however, controlling the mechanical stress imposed on the film by the underlying substrate is extremely challenging due to the high processing temperatures required to crystallize ferroelectric materials. As previously discussed, most ferroelectric thin films processed on Si substrates are under appreciable levels of in-plane tensile stress and residual stress acts as a pinning source preventing non-180^o domain wall motion. Therefore, the experimental studies reporting reduced remanent polarization and increased coercive field with increasing film thickness are inherently flawed as they cannot differentiate the true ferroelectric size effects from residual stress effects due to clamping to the substrate.

Because of such difficulties in characterizing extrinsic size effects experimentally, a larger focus has been placed on theoretical calculations. For instance, Madsen et. al used previous modeling results from Tanners and Ashby's theoretical work [108] to calculate the minimum size for twinning in $PbTiO_3$ (~10 nm) [109]. Twinning in ferroelectrics occurs in order to reduce the elastic energy associated with misfit strain via the formation of periodic 90^o domain walls [110]. At a critical thickness, domain twinning is no longer energetically favorable due to the increase in energy associated with domain wall formation. In other words, twin domains only occur in systems in

which the sum of elastic energy and domain wall energy is a minimized. J. Hlinka et. al also determined the minimum size for twinning by numerically solving the time-dependent Ginzburg-Landau[10] equation for the polarization field [111]. The model indicated that the minimum size for twinning in $BaTiO_3$ is ~22.9 nm.

In general, however, theoretical studies of size effects in ferroelectrics are curbed also by practical limitations. Specifically, although theoretical calculations for "simple" perovskite chemistries such as $BaTiO_3$ and $PbTiO_3$ are more approachable, most technologically-relevant compositions for piezoelectric applications are more complex solid solutions (such as PZT or relaxor-ferroelectric compositions $Pb(Mg_{1/3}Nb_{2/3})O_3$-$PbTiO_3$, $Pb(Zn_{1/3}Nb_{2/3})O_3$-$PbTiO_3$, or $Pb(In_{1/2}Nb_{1/2})O_3$-$Pb(Mg_{1/3}Nb_{2/3})O_3$-$PbTiO_3$) presenting a major challenge for any theoretical approach.

In summary, only a limited number of techniques are available for fabrication of ferroelectric materials at the nanoscale that allow compatibility with device production. In fact, the inability of available techniques to produce structures with user-defined shapes, locations, and aspect ratios has been a major limitation for development of active nanoelectromechanical systems. In addition, the inability to pattern piezoelectric materials at the nanoscale without inducing surface damage has prevented experimental verification of theoretical predictions of interesting nanoscale phenomena in ferroelectric materials. Based on this literature review, the research conducted herein aims to develop a manufacturing method for fabricating piezoelectric nanostructures with excellent control of the design and to further explore factors affecting future device performance

[10] The Ginzburg-Landau theory is a mathematical theory developed to examine macroscopic properties of a material with the aid of general thermodynamic arguments without attempting to explain the underlying microscopic mechanism. Based on this theory, the free energy of a ferroelectric material, in the absence of electric field and applied stress, can be written as a Taylor expansion in terms of components of the polarization vector.

by characterizing the elements that influence domain wall motion such as substrate clamping, lateral constraint, and critical size.

CHAPTER 3

MICRO/NANOFABRICATION METHODS AND CHARACTERIZATION TECHNIQUES

This chapter details the cleanroom equipment used to manufacture PZT nanotubes and characterize their structure. In addition, procedures used to measure electromechanical properties are also discussed.

3.1 Thermal Oxidation

Thermal oxidation of silicon involves heating a silicon wafer at elevated temperatures in order to promote the growth of silicon dioxide. A typical oxidation furnace consists of a resistive heating element wound around a fused silica tube. The wafers are placed in a quartz boat and are inserted into a heated furnace tube using a cantilever load arm.

Silicon dioxide is formed via chemical reactions with molecular oxygen (dry oxidation) (Reaction 3.1) or water vapor (wet oxidation) (Reaction 3.2).

$$Si_{solid} + O_{2\,gas} \rightarrow SiO_2 \qquad \text{Reaction 3.1}$$

$$Si_{solid} + 2H_2O_{vapor} \rightarrow SiO_2 + 2H_2 \qquad \text{Reaction 3.2}$$

Wet oxidation results in a lower quality oxide due to the inclusion of hydrogen impurities; however, the primary advantage of using water vapor as the reactant is the

enhancement of oxygen's diffusion rate through the oxide layer to the reaction site at the silicon-oxide interface, resulting in faster growth rates. Silicon wafers used in this thesis were wet-oxidized via a Tystar Furnace at 1100°C for 2 hr and 20 min (see section 4.1).

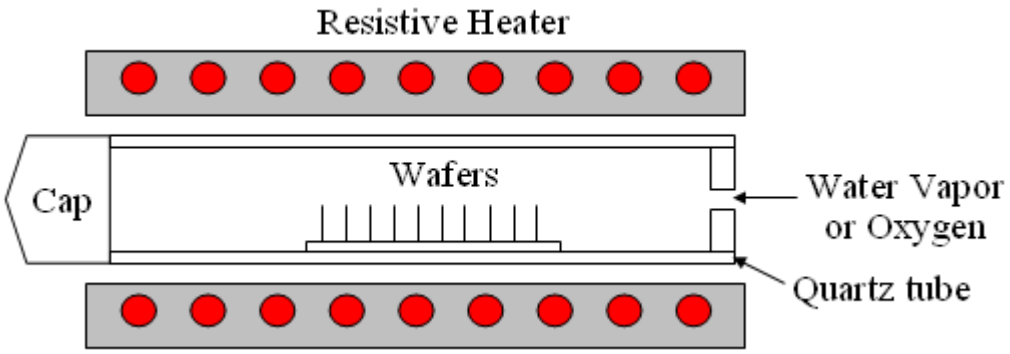

Figure 3.1: Schematic representation of a typical thermal oxidation furnace.

3.2 Physical (Sputter) Deposition

Sputter deposition is a physical vapor deposition method for depositing thin (often metallic) films. Plasma is initiated via the application of a large voltage across a parallel plate reactor in a vacuum chamber. The characteristic glow is due to the emission of phonons. Once the plasma is formed, ions are accelerated towards the cathode (i.e. target) and collide into it. When the energetic ion strikes the target with the appropriate amount of energy[11], the target ejects atoms that deposit on the substrate. The sputter

[11] Energetic ions with very low energy may simply bounce off of the target's surface, while at extremely high energies the ion can become implanted into the target.

yield, or ratio of the number of target atoms ejected per number of incident ions, depends on the ion's mass, the ion's energy, the target's mass, and the target's crystallinity. In this thesis, oxidized Si wafers were sputter coated with Ti and Pt via a Unifilm Multisource Sputtering System (see section 4.1).

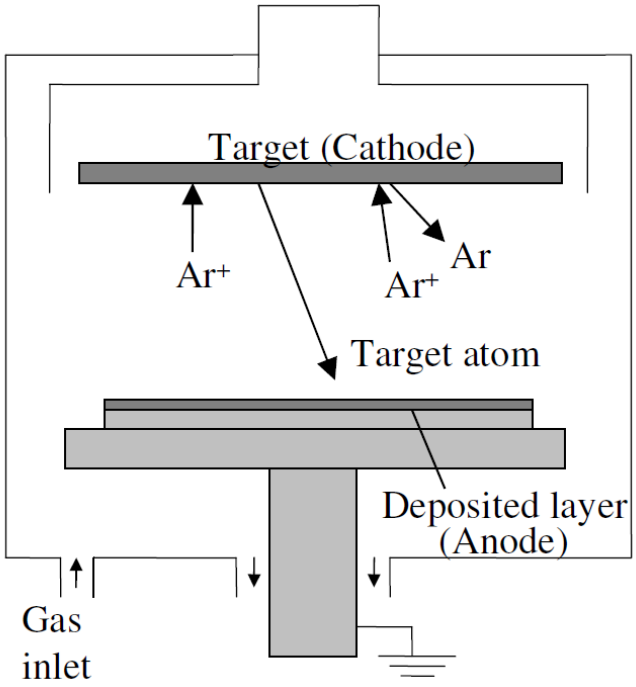

Figure 3.2: Schematic representation of a typical sputter deposition chamber.

3.3 Electron Beam Lithography (EBL)

Electron beam lithography (EBL) is a patterning approach with nanometer resolution in which a beam of electrons are scanned across electron sensitive resist. Resist are generally composed of a polymer resin and sensitizers dissolved in an organic solvent. After spin coating, the resist film is soft-baked to remove residual solvent and

exposed. Electron irradiation of the resist causes chemical changes such as cross-linking or chain scission, which results in differentiation in the solubility of the exposed regions when compared to unexposed regions. Resists are classified as negative tone if cross-linking is the dominant chemical process in the exposed region or positive tone if chain scission dominates. Figure 3.3 illustrates the resulting pattern for both negative and positive tone resist after development.

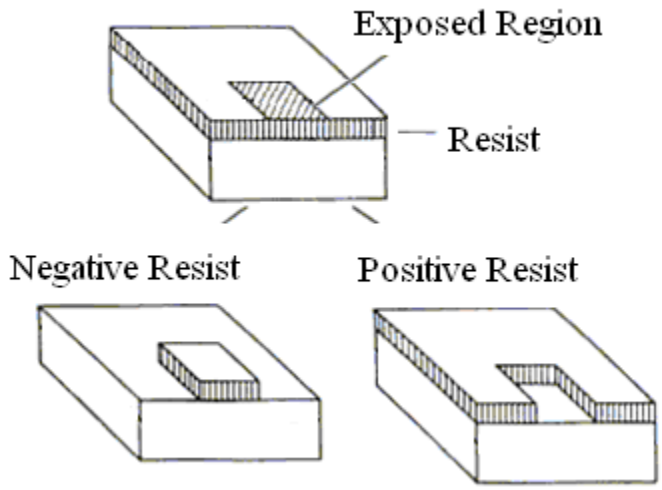

Figure 3.3: Schematic representation of (electron beam) lithography with patterning of both positive and negative resists

The optimal exposure dose is dependent on the pattern density, underlying substrate, accelerating voltage, and resist thickness (Table 3.1). For a given patterned region, as the density increases, the required dose decreases due to scattering of electrons (proximity effect). The underlying substrate also affects the required dose due to

electrons penetrating the resist and colliding with the substrate. The type of collision depends on the lattice parameters of the substrate. As the distance between atoms increases, the higher probability of electrons from the beam passes through the substrate lattice and become implanted. However, as the lattice constant decreases, electrons are more likely to undergo elastic collisions, thus broadening the exposure area and decreasing the required dose (back scattering).

The accelerating voltage also affects the required dose. As the accelerating voltage increases, the beam spot size decreases because there is less time for electrons to repel each other when traveling down the electron beam's column. As the beam spot size decreases, the required dose increases. Finally, the resist thickness also affects the required dose. As the resist thickness decreases, the required dose decreases as less volume of material requires exposure.

In this work, a JOEL JBX-9300FS system was used for EBL patterning. The electron beam is generated via a thermal field emission and is focused via a four-stage lens system. Patterning is performed via a vector scan and step-and-repeat method. The superior resolution of EBL when compared to optical lithography is due to orders of magnitude shorter wavelength of electrons when compared to UV photons.

Table 3.1: Factors affecting the required dose in EBL patterning

Increase in the following parameters:	Required Dose
Pattern Density	↓
Resist Thickness	↑
Accelerating Voltage	↑
Substrate's Lattice Constant	↑

Figure 3.4: JOEL JBX-9300FS Electron Beam Lithography Tool for patterning electron-sensitive resist.

3.4 Atomic Layer Deposition (ALD)

Atomic Layer Deposition (ALD) is based on self-limiting sequential gas phase chemical reactions, in which precursors remain separate throughout the process. The major advantage of ALD when compared to other deposition techniques is its excellent thickness uniformity over complex landscape profiles. ALD is similar in chemistry to chemical vapor deposition; however, the chemical reaction is broken into two half-reactions. A precursor gas is introduced into the process chamber and chemisorbed on the substrates surface. Excess precursor is then purged from the chamber. A second precursor is then introduced into the chamber reacting with the first. The byproducts from the reaction and the excess precursor, is again removed from the camber via a vacuum purge.

For Al_2O_3 ALD, the substrate is placed in the reactor and water vapor is introduced into the chamber. The water vapor absorbs on the surface forming hydroxyl groups (Figure 3.5a). Next, Trimethyl Aluminum (TMA) is pulsed into the reaction chamber. TMA reacts with the absorbed hydroxyl groups and produces methane byproducts (Figure 3.5b). The reaction continues until complete passivation of the surface[12] (Figure 3.5c) (Reaction 3.3). The excess TMA and methane is then pumped out of the chamber. Water vapor is again pulsed into the process chamber and reacts with the dangling methyl groups (Figure 3.5d), forming aluminum-oxygen bridges and hydroxyl surface groups[13] (Figure 3.5e) (Reaction 3.4). The methane byproduct is once again pumped out of the chamber. By setting the total number of cycles (two half-reactions

[12] TMA is self-limiting in that it does not react with itself.
[13] Excess H_2O vapor does not react with the hydroxyl surface groups, again limiting the reaction causing perfect passivation.

form one cycle) the alumina thickness can be controlled (Figure 3.5f). In this research, ~10 nm of Al_2O_3 is deposited via a Cambridge Fiji ALD system (see section 4.1.2).

$$Al(CH_3)_{3(g)} + O - H_{(s)} \rightarrow O - Al(CH_3)_{2(s)} + CH_4 \qquad \text{Reaction 3.3}$$

$$2H_2O_{(g)} + O - Al(CH_3)_{2(s)} \rightarrow O - Al(OH)_{2(s)} + 2CH_4 \qquad \text{Reaction 3.4}$$

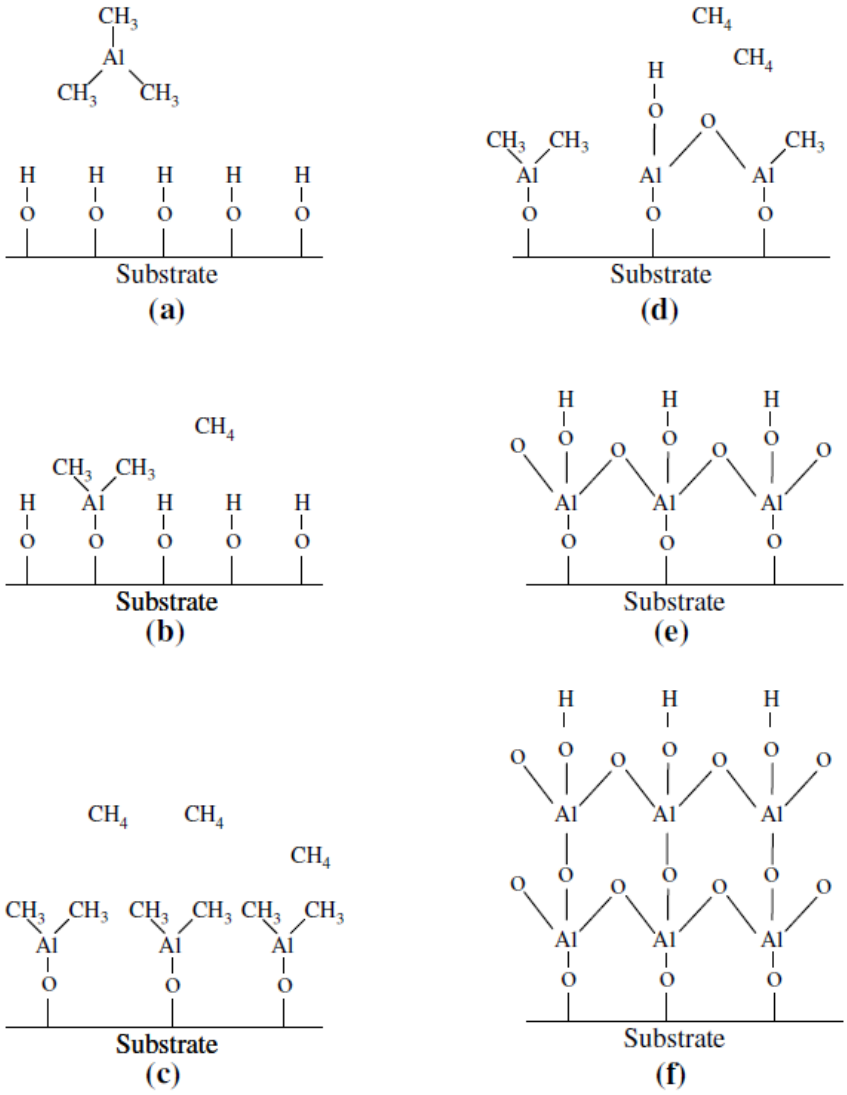

Figure 3.5: Schematic representation of subsequent chemical reactions during atomic layer deposition of Al_2O_3: (a) hydroxyl groups (either native or after a first water pulse) on the sample surface are exposed to the TMA groups during the Al-precursor pulse; (b) reaction of TMA with hydroxyl groups; (c) passivation of surface with TMA and removal of byproduct methane; (d) pulse of water vapor and reaction with the organic groups; (e) absorption of water vapor on surface and removal of byproduct methane; and (f) processes b-d are repeated until the desired Al_2O_3 thickness is achieved.

3.5 Reactive Ion Etching (RIE)

Reactive Ion Etching (RIE) is a method that uses both chemical and physical means to remove material. Plasma is generated in a vacuum chamber via an electromagnetic field. The oscillating electric field ionizes gas molecules via stripping them of electrons. The ions are then accelerated towards the sample surface and undergo chemical reactions, with material removal accomplished via volatile reaction compounds. Etching can also occur via physical means in which energetic incident ions collide with the sample causing the surface to eject atoms. In this research, the thin layer of Al_2O_3 connecting adjacent PZT pillars is removed via a STS Vision 320 RIE System with the following gas flow rates: 25 sccm CHF_3, 5 sccm O_2, and 25 sccm Ar at a pressure of 25 mT and a power of 200 W.

3.6 Refractometry

Refractometry is a measurement technique to characterize the thickness and refractive index of transparent thin films. The intensity of reflected light is measured as a function of wavelength. When the incoming light and reflected waves constructively interfere, an optical maximum results; however, if the waves interfere destructively, a minimum results. By determining difference in the wavelength between the maxima or minima ($\Delta\lambda$), the thickness (t) can be determined via Equation 3.5.

$$t = \frac{\Delta\lambda}{2n} \qquad \text{Equation 3.5}$$

In Equation 3.5, n is the real component of the refractive index and is assumed to be wavelength independent. The thickness of the spin coated ma-N 2403 was measured via a Nanospec Refractometer over the spectral range from 400 nm to 800 nm. The refractive index is nearly wavelength independent (less than 6% variation) for wavelengths ranging from 400 nm to 800 nm (Figure 3.6).

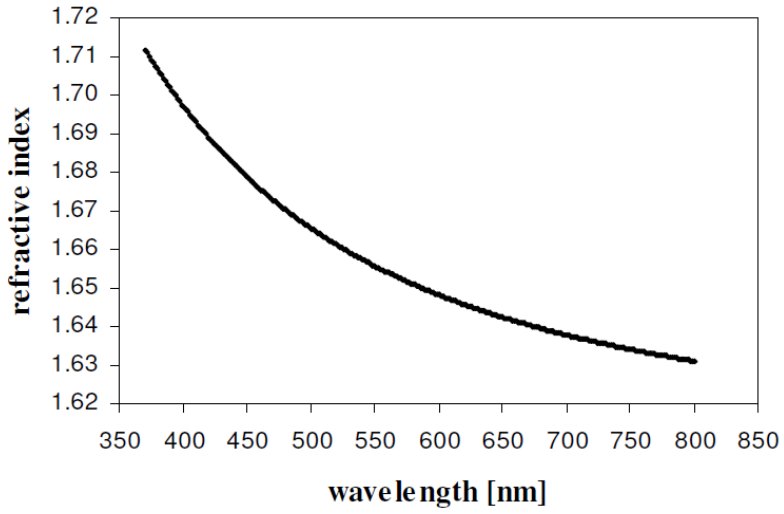

Figure 3.6: Refractive index vs. wavelength of unexposed ma-N 2403 determined via ellipsometry.

3.7 Ellipsometry

In this technique, a polarized coherent beam of light is incident on the surface at several angles and wavelength. Ellipsometry measures the complex reflectance which is parameterized by Ψ and Δ (Equation 3.6).

$$\rho = \frac{r_p}{r_s} = \tan(\Psi)e^{i\Delta} \qquad \text{Equation 3.6}$$

In Equation 3.6 r_s and r_p represents normalized components of the complex reflectance oscillating perpendicular and parallel to the sample surface, respectively. Tan(Ψ) is the amplitude ratio after reflection and Δ is the change in polarization angle. The film thickness and index of refractions is then determined by fitting experimental data to models such as Cauchy. The Cauchy model assumes that index of refraction (n) decreases with increasing wavelength (λ) (Equation 3.7).

$$n(\lambda) = A + \frac{B}{\lambda^2} + \frac{C}{\lambda^4} \qquad \text{Equation 3.7}$$

The film thicknesses and refractive index of ALD Al_2O_3 was measured using a J.A. Woollam variable-angle spectroscopic ellipsometer (VASE). Measurements were obtained over the spectral range from 370 nm to 1690 nm using incidence angles of 65^o, 70^o, and 75^o.

3.8 Scanning Electron Microscopy (SEM)

Microstructural characterization of the PZT nanostructures was performed via a Zeiss Ultra60 Field Emission Scanning Electron Microscope (SEM) with a 5 keV acceleration voltage and 30 μm aperture. The working distance was set at 4 mm from the pole piece. Secondary electrons were detected via a high efficiency in-lens detector.

3.9 Focused-Ion Beam (FIB) Milling

Cross-sections of the resulting PZT structures were prepared via focused-ion beam (FIB) milling. Gallium ions are extracted from a liquid metal ion source via the application of an electric field and accelerated towards the sample. Gallium is used due to its low surface free energy (ensures wetting of the needle), low volatility (leads to a long source life), and low melting temperature (29.8 ºC) (minimizes reactions between the source and the tungsten needle).

During operation, Ga flows from the reservoir to the tip of the tungsten needle via the application of electric field between the tip and extraction electrodes. The electric potential causes the conductive liquid to deform into a Taylor cone. When a threshold voltage is reached, the Taylor cone inverts and releases a source of ions. The extracted ions travel down the ion column with a user-defined acceleration voltage and beam current[14]. The beam is focused via a condenser lens and objective lens. When the Ga ions collide with the sample's surface, moment is transferred from the incident ion to the sample. If the energy transferred is greater than the sample's binding energy, surface ions are ejected. For cross-sectional milling of the PZT nanotubes, an acceleration voltage of 20 keV and a beam current of 10 pA was used.

The FIB system was also used to deposit top electrodes (Pt) on the PZT nanotubes. The deposition process is similar to the etching process. A precursor is introduced near the surface of the sample using a small nozzle and is then absorbed onto the surface. The precursor is then decomposed into volatile and nonvolatile products by the ion beam. The volatile components are removed via the vacuum while the nonvolatile products

[14] The beam current is controlled via the aperture's diameter.

remain on the surface, producing a deposited layer. The precursor used to deposit Pt was Trimethyl (methylcyclopentadienyl) platinum ($C_9H_{16}Pt$) with a 10 keV acceleration voltage and 50 pA beam current.

3.10 Energy-Dispersive X-ray Spectroscopy (EDS)

Chemical analysis of crystallized PZT was performed via energy-dispersive x-ray spectroscopy (EDS). In this technique, inner shell electrons of a sample are ejected via a high energy beam resulting in an electron hole. In order to compensate, outer shell electrons replace the ejected electrons by releasing energy in the form of x-rays. The amount of energy released by the transferring electron depends on its current shell occupancy (i.e. energy level) and its desired shell occupancy. Every atom possesses a unique amount of energy released during the electron transferring process to various shells (Figure 3.7), therefore allowing the identity of the atom from which the x-ray was produced to be determined. Table 3.2 details the K_α, L_α, and M_α peak for lead, zirconium, and titanium. The K_α peak corresponds to the amount of energy required for electrons to transfer from the L-shell to the K-shell. The L_α peak corresponds to the amount of energy required for electrons to transfer from the M-shell to the L-shell, and the M_α peak corresponds to electron transfer from the N-shell to the M-shell. In this work, EDS was performed with excitation beam of 15 keV.

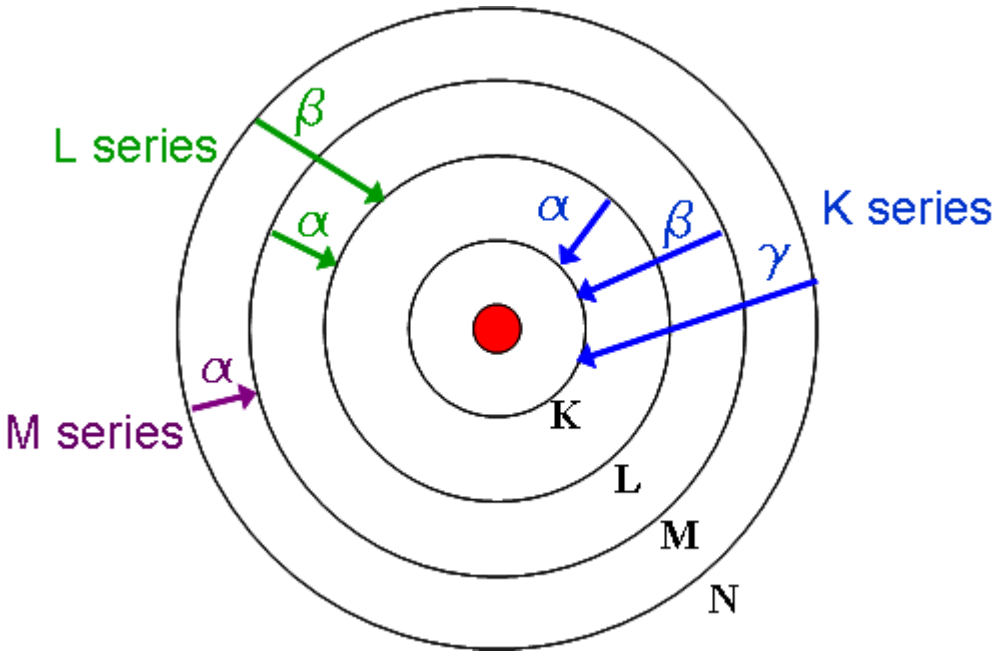

Figure 3.7: Illustration of the various x-rays emitted by electron transfer from higher-energy shells to lower-energy shells during EDS analysis.

Table 3.2: Peaks for EDS analysis of PZT

	K-alpha (keV)	L-alpha (keV)	M-alpha (keV)
Lead	74.969	10.551	2.345
Zirconium	15.775	2.042	---
Titanium	4.510	0.452	---

3.11 X-ray Diffraction (XRD)

X-ray diffraction (XRD) is a versatile, non-destructive technique that provides information regarding chemical composition and crystallographic structure via K-α1 emission. A monochromatic x-ray beam is incident on a crystal such that diffraction occurs (i.e. constructive interference). Monochromatic x-rays are desirable to prevent

peaks from K-β emission. The relationship between x-ray wavelength and interatomic spacing to the angle of diffracted beam is described via Bragg's law (Equation 3.8) and is illustrated in Figure 3.8.

$$n\lambda = 2d_{space}\sin\theta \qquad \text{Equation 3.8}$$

In Equation 3.8, n is an integer, λ is the wavelength of the incident x-ray, d_{space} is the interplanar spacing of the crystal, and θ is the angle of incidence.

In θ-2θ scans, the diffracted beam intensity is collected at an angular position of twice the incident beam. High intensity peaks result when the Bragg diffraction condition is satisfied, thereby providing information regarding the crystallographic planes present.

The XRD tool used in this study was an X'Pert PRO Alpha-1 with a Johansson monochromator and ultra-fast X'Celerator detector (Figure 3.9). The x-ray generator was set at 45 kV and 40 mA. The incident beam optics included a 10 mm mask and an anti-scatter slit fixed at 1^o. The diffractive beam optics included a 5.0 mm antiscatter slit. The PZT films were scanned from 20^o to 65^o using a θ-2θ goniometer.

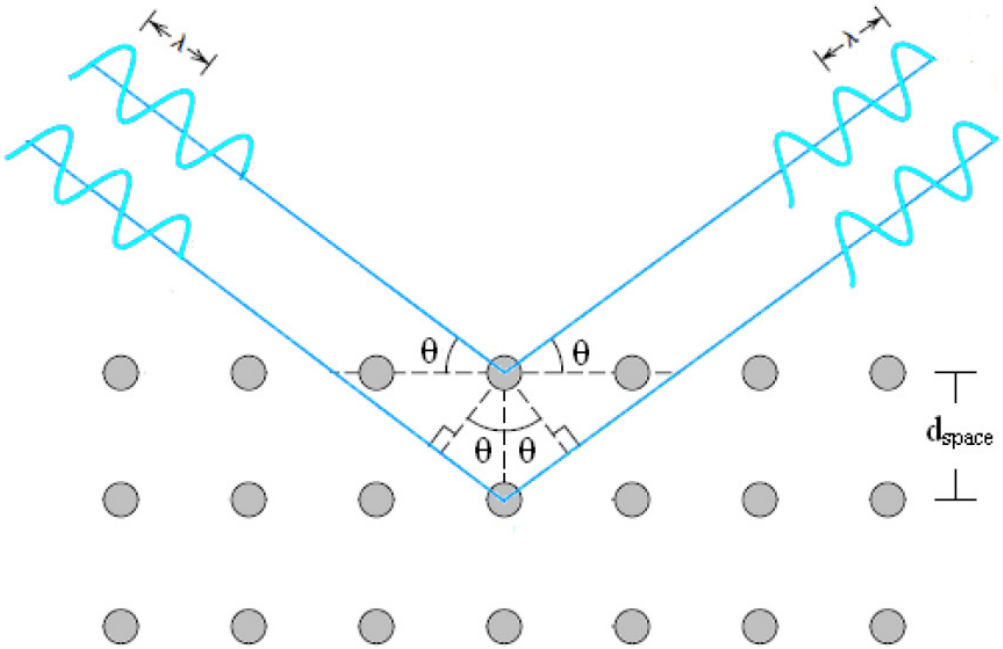

Figure 3.8: Schematic illustration of Bragg's law of diffraction for crystalline solids.

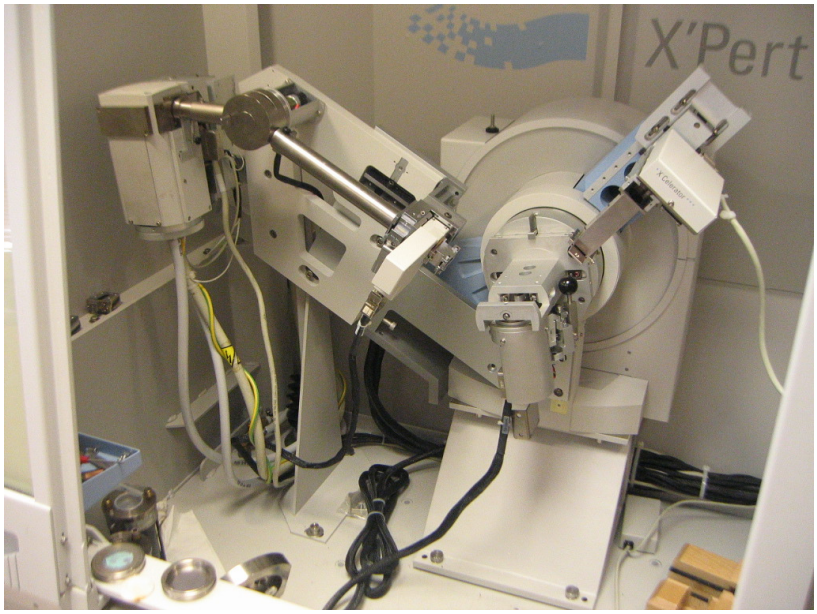

Figure 3.9: X'Pert PRO Alpha-1 diffractometer with a CuK_{α} radiation and θ-2θ goniometer used in this work.

3.12 Micro-Raman Spectroscopy

Raman spectroscopy is a light scattering technique in which incident photons interact with a material's crystal lattice resulting in the change in wavelength of the refracted beam with respect to the incident beam. This wavelength shift is dependent on the distribution of phonons and electrons within the material's lattice.

Impingement of incident radiation on the sample's surface can result in three different events. The photon can be reflected, absorbed, or transmitted. Raman spectroscopy solely studies photon absorbance. When a photon is absorbed either via an electron or more unlikely case a phonon [112], the absorbing species is promoted from a ground state to a virtual energy state. Subsequently, the exited species relaxes via photon emission. If the excited species relaxes without further interactions, the wavelength of the emitted photon is identical to the incident photons. This phenomenon is known as elastic Rayleigh scattering. In a small number of occurrences, the excited species either absorbs or emits additional energy carriers and moves to a secondary non-equilibrium state. Upon relaxation from this secondary state, the wavelength of the emitted photon is unequal to the incident photon's wavelength. Stokes scattering occurs when the photon is scattered at lower energy (i.e. lower frequency) and Anti-Stokes scattering occurs when the photon is scattered at higher energy (i.e. higher frequency) (Figure 3.10).

Raman spectra in the range of 100-800 cm^{-1} were collected for PZT nanotubes at an excitation wavelength of 512 nm and exposure time of 15 sec. The spectra were compared to reference PZT films. A notch filter was used to cut-off the spectral range of ~100 cm^{-1} from the laser line in order to prevent stray light due to Rayleigh scattering from exceeding the intensity of the Raman signal.

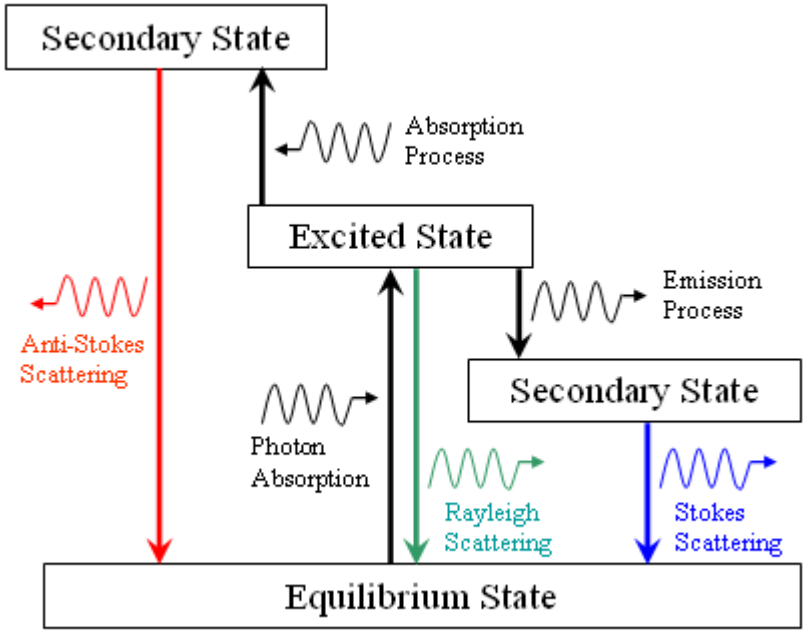

Figure 3.10: Process flow diagram illustrating three types of scattering events: Rayleigh, Stokes, and Anti-Stokes [113].

3.13 Piezoresponse Force Microscopy (PFM)

Piezoresponse Force Microscopy (PFM) is a scanning probe microscopy technique in which an AC voltage is applied to the sample via the tip of a cantilever in order to measure the converse piezoelectric effect. The underlying Pt substrate is used as the bottom electrode and is connected to ground. The surface response is equal to the bias-induced tip deflection (Equation 3.9)[114].

$$d = d_o + A\cos(\omega t + \varphi) \qquad \text{Equation 3.9}$$

The phase (φ) of the electromechanical response of the surface provides information regarding the polarization direction. For example when a positive tip bias is applied to the sample and the polarization vector is pointed downward, the surface oscillations are in phase with the tip voltage ($\varphi = 0$). However, when a positive tip bias is applied and the polarization vector is pointing upward, the surface oscillations are 180^o out-of-phase. Difficulty in interpretation of results arises due to electrostatic interactions (A_{el}) between the tip and the surface and non-local contributions due to buckling of the cantilever (A_{nl}) (i.e. capacitive cantilever surface interactions) that can also contribute the strain-amplitude response (A) [115] [116].

$$A = A_{el} + A_{piezo} + A_{nl} \qquad \text{Equation 3.10}$$

The dominant contribution to the strain-amplitude response in Equation 3.10 depends on the tip radius and indentation force. In order to develop quantitative piezoelectric response measurements, the electrostatic and cantilever surface interactions must be minimized. Figure 3.11 shows several different regimes in which different contributions to the strain-amplitude response dominate [117]. It is important to note that the extension of the different regions also depends on the contact between the tip and the sample's surface. Less than perfect contact can result due to poorly conductive coating and contaminates on the sample surface. The operational mode for experiments conducted in this thesis is in the strong indentation regime as previous studies have shown that the piezoresponse is dominated in this regime by d_{33}. For instance, Figure 3.12 shows the sensitivity of the piezoresponse to s_{ij} (elastic compliance), d_{ij} (piezoelectric coefficient)

and ε_{ij} (dielectric permittivity) for three different ferroelectric compositions. The main contributor to the piezoresponse is d_{33}, which is nearly 4 times larger than the next largest contributors which are d_{31} and ε_{33}[15]. This dominance implicitly justifies the assumption that the measured piezoresponse is equal to d_{33} and electrostatic contributions are negligible.

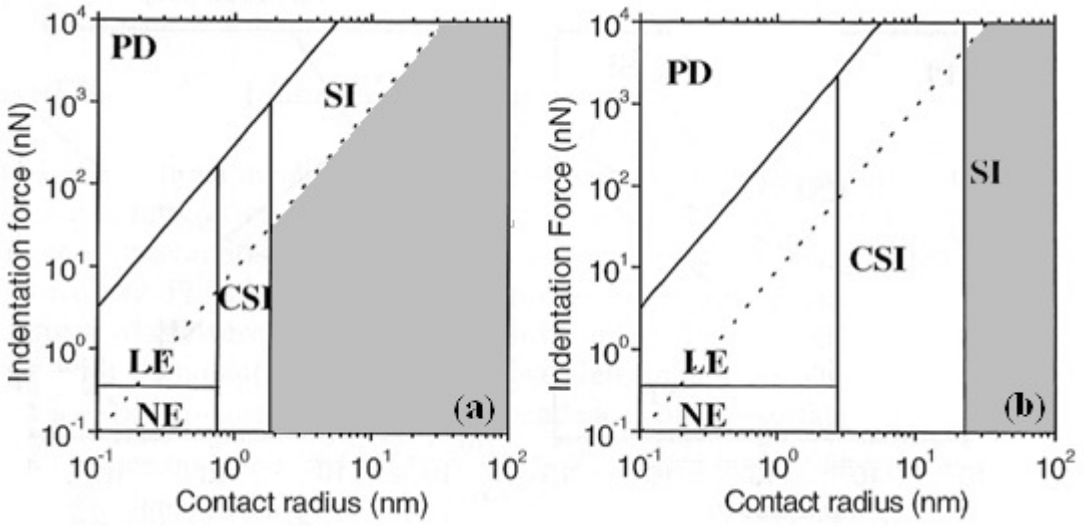

Figure 3.11: (a) Good contact and (b) poor contact in PFM measurements. SI denotes strong indentation regime, CSI the contact limited strong indentation regime, LE the linear electrostatic regime, NE the nonlinear electrostatic regime, NL the non-local effects regime, and PD the plastic deformation regime. The area above the dotted line designates the region where stress-induced switching is possible, and therefore, the ideal working condition for electrical-switching in PFM is the region denoted by gray shading [114].

[15] The dielectric permittivity contributes to the strain amplitude due to Coulombic tip-surface interaction.

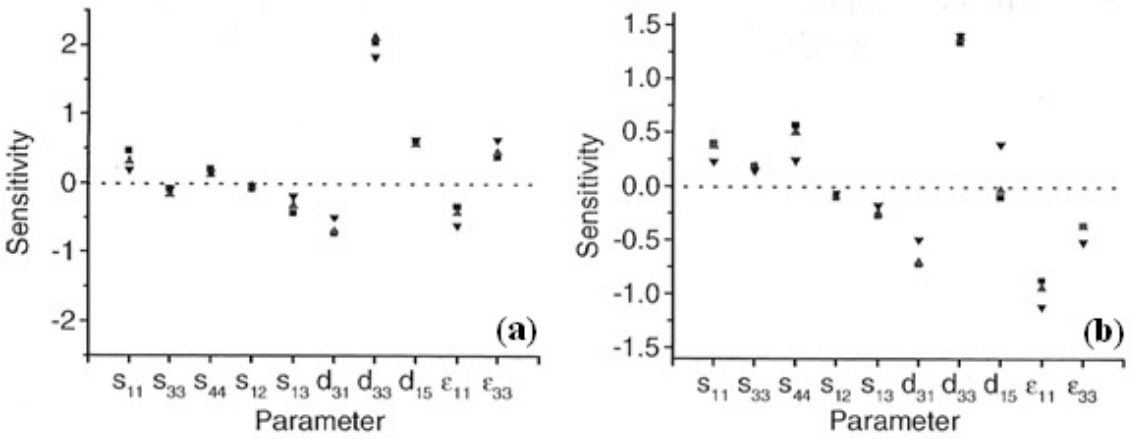

Figure 3.12: Sensitivity of the piezoresponse characterization to different material parameters for (a) strong indentation (b) weak indention regime. The data refer to characterization of $BaTiO_3$ (squares), PZT4 (upward pointing triangles), and PZT5a (downward pointing triangles) [114].

3.13.1 Calibration of the Piezoresponse Signal

The piezoresponse measurement technique is based on the detection of local vibrations of a PFM cantilever induced by probing a piezoelectric material via an applied AC signal. The cantilever vibrations are converted to an electrical signal (piezoresponse signal (PRS)) via a photodiode. The piezoelectric coefficient (d_{33}) can then be extracted from the PRS [114]:

$$h_w = \beta d_{33} A_w \qquad \text{Equation 3.11}$$

In Equation 3.11, h_w is the amplitude of the PRS, A_w is the amplitude of the probing voltage, and β is the sensitivity of the detector (i.e. conversion factor between the mechanical displacement of the tip and the amplitude of the PRS). In order to calibrate the output response of the tool, the amplitude of the PRS is measured for a

quartz sample which has a known piezoelectric coefficient of 3 pm/V. For the Cypher™ Atomic Force Microscope (Asylum Research) used in this research, the sensitivity was found to be 0.0767 V/nm (i.e. 130 nm/V). For more information regarding the calibration see 6.10.

3.13.2 Band-Excitation Piezoelectric Force Microscopy (BE-PFM)

In PFM scans, an AC voltage is applied between the conductive tip and a bottom electrode located underneath the ferroelectric material being tested. The application of the time varying voltage results in an oscillating surface displacement due to the converse piezoelectric effect. This change in surface displacement results in the cantilever being driven into oscillation. If the driving frequency of the PFM approaches the contact resonance of the system (i.e. cantilever and sample), then the recorded deflection of the cantilever can increase by orders of magnitude, which results in an increase in sensitivity (i.e. increase in signal-to-noise ratio).

In order to ensure that this increased sensitivity is maintained throughout a scan, Band-Excitation Piezoelectric Force Microscopy (BE-PFM) (Figure 3.13) has been developed by S. Jesse et al. [118]. In this technique, the input signal excites the cantilever with a band of frequencies. The frequency band is chosen such that the resonance frequency of the system is captured for all points along the sample's scanned area. For BE-PFM performed in this thesis, a chirp waveform was used with a 3 V_{ac} amplitude, 280 kHz center frequency, 80 kHz bandwidth, and 250 Hz point spacing in the

frequency domain. 3 V_{ac} was used to excite the film corresponding to <1/3 the coercive field to ensure the domain density did not change.

The user defined input signal is then Fourier transformed to generate the excitation signal in the time domain. When the excitation signal is applied to the sample via the Pt coated cantilever tip, the sample oscillates due to the converse piezoelectric effect, which causes the cantilever to vibrate. This vibration (i.e. displacement) is captured via reflecting a laser off of the end of the cantilever onto a photodiode. The photodiode converts the cantilever's displacement into an electrical signal known as the piezoresponse signal (PRS). The PRS is collected via a fast data acquisition card (NI-6115) and fast Fourier transformed to convert from the time domain to the frequency domain, thereby allowing the amplitude and phase vs. frequency curve to be determined at each point in the scanned image. The PRS signal is analyzed by fitting a simple harmonic oscillator (SHO) model at each scanned point independently in order to identify three independent parameters: resonant frequency (ω_o), max amplitude (A_{max}), and electromechanical quality factor (Q) (Equation 3.12 and Equation 3.13). It should be noted that ω_o is not the resonance frequency of the free cantilever but rather related to the tip-surface interaction.

$$A(\omega) = \frac{A_{\max}\,\omega_o^2}{\sqrt{(\omega^2 - \omega_o^2)^2 + (\omega\omega_o / Q)^2}} \qquad \text{Equation 3.12}$$

$$\tan(\varphi(\omega)) = \frac{\omega\omega_o / Q}{\omega^2 - \omega_o^2} \qquad \text{Equation 3.13}$$

For these measurements, the PZT nanotube is probed using a platinum coated AFM tip (Olympus, AC240TM), while the underlying platinized silicon substrate is used as the bottom electrode.

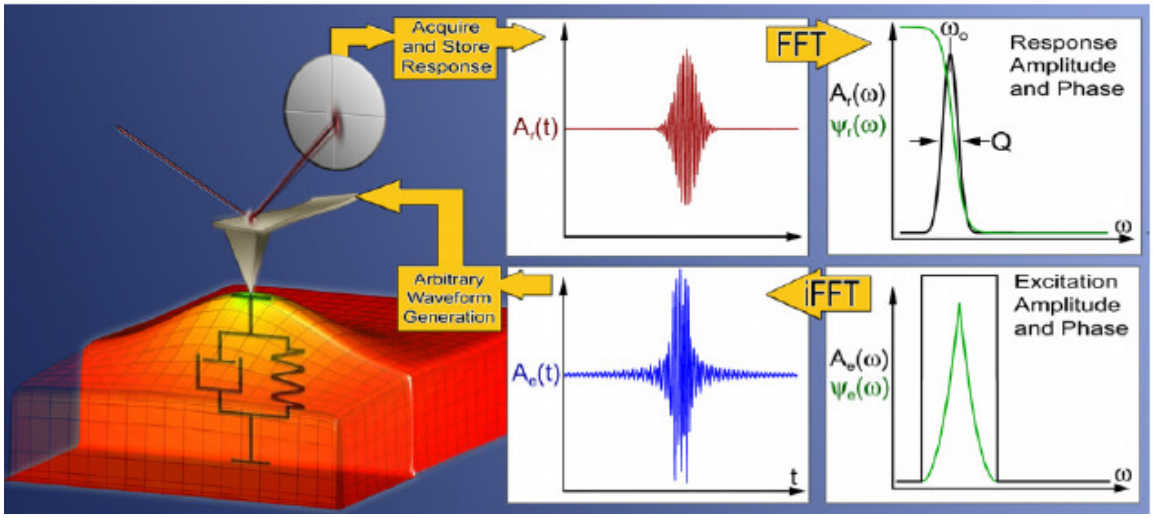

Figure 3.13: BE-PFM setup for conducting piezoresponse measurements where A=response amplitude, ψ=phase, ω_o= resonance frequency, and Q=mechanical quality factor [118].

3.13.3 Switching Spectroscopy Piezoelectric Force Microscopy (SS-PFM)

To study the ferroelectric response of the PZT nanotubes, Switching Spectroscopy Piezoelectric Force Microscopy (SS-PFM) is employed in which electromechanical hysteresis loops are acquired at each scanned point on a closely meshed grid. In order to collect these hysteresis loops, a triangular wave of DC pulse steps (i.e. bias) is applied to the sample through the AFM tip (Figure 3.14), and the response (amplitude and phase) is collected after each DC pulse for a band of frequencies. The change in response amplitude (A) and phase (ψ) at resonance is a direct result of the nucleation and growth of domains and is used to determine the piezoelectric response (PR) (Equation 3.14). Subsequent analysis of the piezoelectric response loops collected allows extraction of similar parameters to that of a macroscopic P-E hysteresis loop such as coercive voltage and remanent response.

$$PR = A_{max} \sin(\Psi) \qquad \text{Equation 3.14}$$

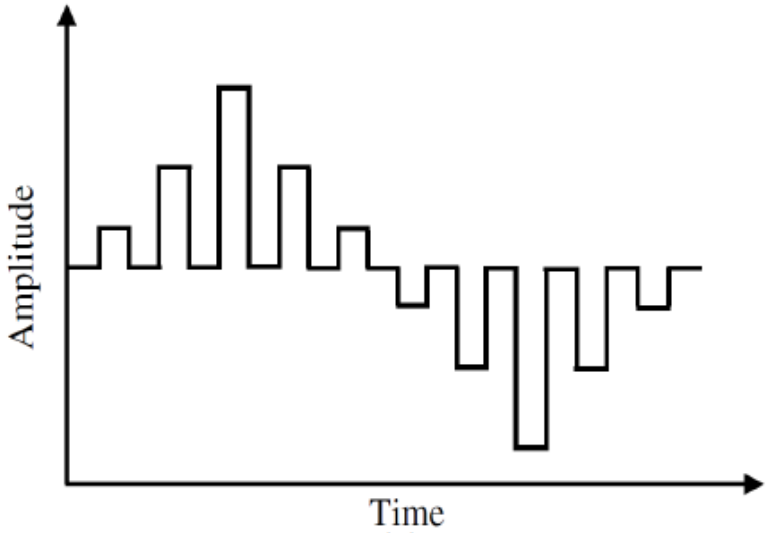

Figure 3.14: Probing waveform for SS-PFM measurements.

3.13.4 Dynamic Switching Spectroscopy Piezoresponse Force Microscopy (D-SS-PFM)

Dynamic Switching Spectroscopy Piezoresponse Force Microscopy (D-SS-PFM) is similar to Switching Spectroscopy Piezoelectric Force Microscopy (SS-PFM) (see section 3.13.3). The major variation lies in the fact that after the application of DC pulse, the response (amplitude and phase) is collected for a band of frequencies as a function of delay time [119]. Thus, D-SS-PFM provides information regarding the response dynamics of the PZT nanotubes at millisecond time scales.

CHAPTER 4

MANUFACTURING METHOD

A manufacturing process capable of creating high aspect ratio piezoelectric material with site specific registry and lateral dimension control is required for creation of many micro- and nano-opto-electro-mechanical systems (MOEMS/NOEMS). The method discussed herein is based on vacuum infiltration of PZT chemical solution precursors into soft-templates.

In order to create soft-templates, negative resist is spin-coated (Figure 4.1a) and patterned using electron beam lithography (EBL) (Figure 4.1b). The soft-templates are then coated with a thin layer of aluminum oxide (<15 nm) using atomic layer deposition (ALD) (Figure 4.1c). The aluminum oxide coated template is then immersed into an ultrasound bath of PZT precursor (sol-gel) solution while under vacuum. Once infiltration of the PZT is completed (determined via the termination of bubble formation), the template is removed from the bath (Figure 4.1d) and rinsed with solvent to remove excess PZT from the surface (Figure 4.1e). The sample is then pyrolyzed and annealed. Thermal annealing leads to decomposition of the organic template and simultaneous crystallization of PZT, therefore creating PZT nanotubes with a thin layer of ALD-deposited aluminum oxide connecting adjacent tubes (Figure 4.1f) [Provisional Patent 61/420,958].

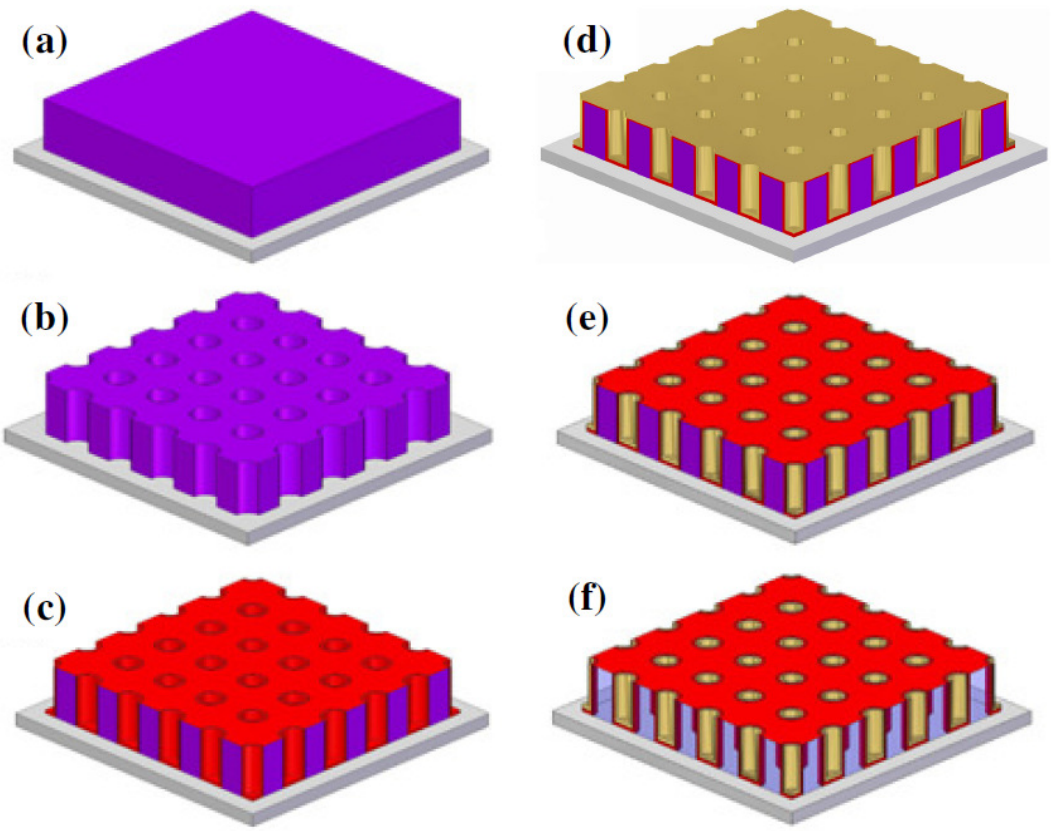

Figure 4.1: Schematic representation of the processing steps used to create PZT nanotubes via sol-gel vacuum-infiltration into a soft-template. (a) The negative e-beam resist is spun-coated onto the substrate; (b) the e-resist is patterned using EBL; (c) the sample is coated with a thin layer of aluminum oxide deposited via ALD; (d) PZT is vacuum-infiltrated into the soft-template; (e) the excess surface PZT is removed; (f) the samples is heat treated to crystallize PZT while the resist is thermally removed (decomposed).

4.1 Soft-Template Processing

(100)-Si substrates were used with an in-house-prepared, bottom electrode stack consisting of 1 μm-thick SiO_2, 200 Å of TiO_x, and 1000 Å of Pt. Si wafers were wet oxidized in a Tystar furnace at 1100°C for 2 hr and 20 min. Wet oxidation was chosen

rather than dry oxidation due to its faster growth rate (discussed in section 3.1). Although wet oxidation results in less dense oxides, the oxide in this application acted as a lead diffusion barrier, therefore breakdown due to electrical stress was not a concern.

Ti and Pt were sputter deposited with a peak rate[16] of 25 Å/min and 200 Å/min, respectively, via a Unifilm Multisource Sputtering System in an argon-enriched low vacuum environment. The Ti was used for adhesion purposes, and Pt was chosen as the bottom electrode material because it can withstand the processing temperature required to crystallize PZT. The resulting grain size of the platinized wafers was less than 30 nm (Figure 4.2).

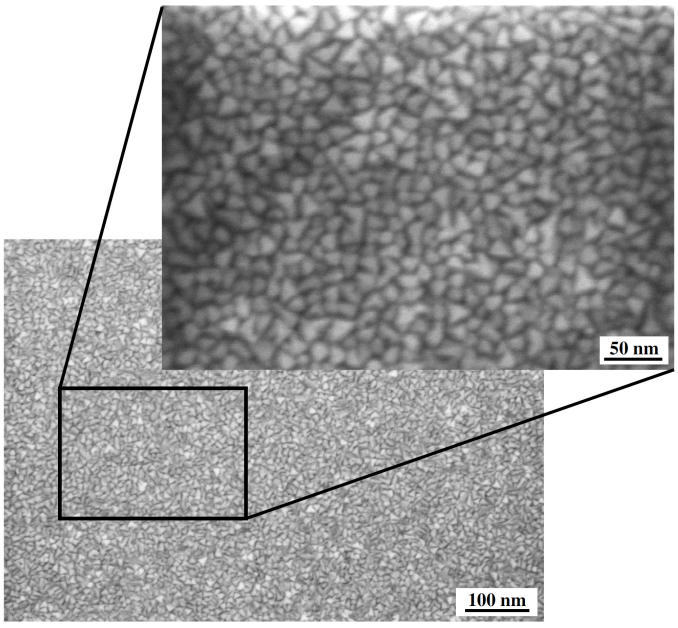

Figure 4.2: SEM micrograph showing platinum grain size uniformity across the wafer and ~30 nm average grain size.

[16] The deposition profile has a Gaussian distribution with the peak deposition directly underneath the center of the target. Therefore in order to ensure a uniform deposition, wafers are placed on a planetary system.

The platinized wafers were cleaned using acetone, methanol, and isoproponal followed by a dehydration bake for 10 min in an oven at 150°C. The cleaning and dehydration bake improved the resist's adhesion to the underlying substrate.

4.1.1 Electron Beam Lithography (EBL)

To create the soft-templates, ma-N 2403 resist was spun coated onto a platinized Si wafer and patterned via EBL[17]. Ma-N 2403 (MicroChem™) is a mixture of a photoactive compound and novolac dissolved in a solution of organic liquids consisting of the following components: 1-Methyl-2-pyrrolidone, n-Butyl acetate, and cyclohexanone. Ma-N 2403 is a negative resist in which crosslinking occurs when exposed to energetic stimuli such as electrons and photons (see section 3.3). The thickness of the resist, ultimately determining the height of the nanotubes, is varied by adjusting the spin speed. After spin coating, the resist is pyrolyzed at 90°C for 1 min to remove excess solvent. Figure 4.3 shows the resist thickness before and after pyrolysis as a function spin speed for a spin duration of 30 sec, measured via a Nanospec Refractometer.

[17] During EBL patterning, electrons deposit a net negative charge on the underlying substrate. A build-up of negative charge can result in electrostatic deflection of the beam. Conductive substrates such as platinized-Si wafers prevent electrostatic beam deflection and thus minimize pattern placement errors.

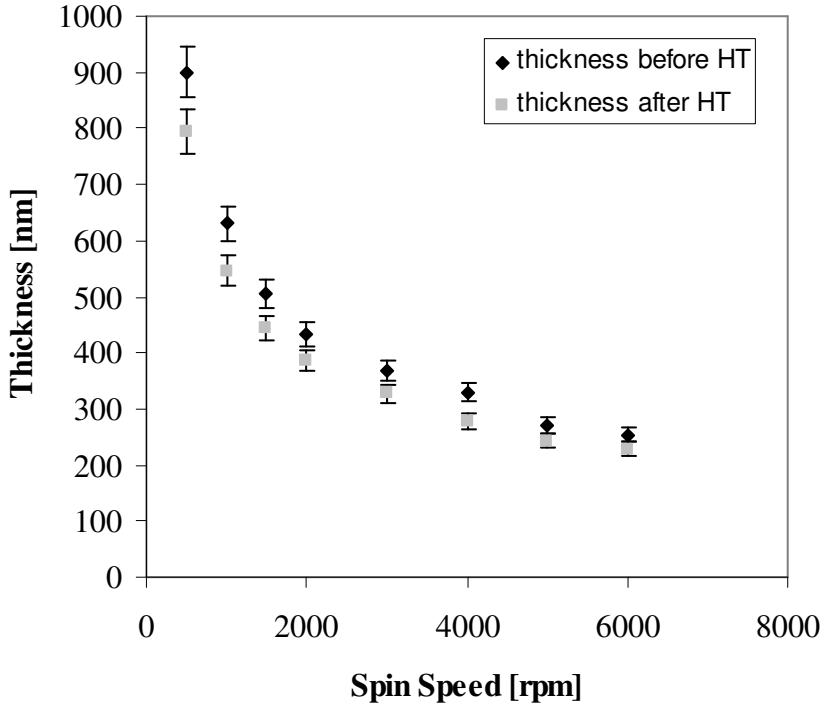

Figure 4.3: Spin speed vs. e-resist thickness curve for ma-N 2403, before and after heat treatment (HT) at 90°C for 1 min.

In order to pattern ma-N 2403, electron beam lithography (EBL) was chosen instead of optical lithography due to its superb resolution in patterning sub-micron features. The resist is patterned using a JOEL JBX-9300FS EBL system with a ZrO/W[18] thermal emission source and a 4 nm diameter Gaussian beam. The dose was adjusted for each pattern density and thickness (see section 5.1). The pattern was developed by immersion in MF-319 (an alkaline corrosive solution containing diluted tetramethylammonium hydroxide, Microposit ™) for 70 seconds followed by immersion in de-ionized water for 1 min.

[18] ZrO/W is commonly used for thermal emission sources due to it low work function (energy to move an electron from the Fermi level into surrounding vacuum).

4.1.2 Atomic Layer Deposition

After development of the polymeric resist, the resist template was coated with 10 nm Al_2O_3 in a Cambridge Fiji ALD system via a 99.99% TMA precursor (Sigma-Aldrich ™). The pulse and purge durations are shown in Table 4.1. The substrate temperature was set at 100°C, chosen due to reflow issues of the resist at temperatures greater than 150°C. Deposition temperatures lower than 100°C are undesirable due to the increased cycle time necessary for the chemical reactions between the Al precursor (TMA) and water to occur. Also, purge times would need to be lengthen to prevent physisorption and to remove unreacted gas-phase precursors [120].

Table 4.1: ALD aluminum oxide processing conditions

Pulse H_2O	Wait	Pulse TMA	Wait	Repeat
0.06 sec	10 sec	0.06 sec	15 sec	100 cycles

4.2 Processing of PZT Nanotubes

The ALD-coated polymeric template was immersed into an ultrasound bath of PZT precursor sol-gel solution while under vacuum. The PZT precursor solution was prepared via a 2-methoxyethanol (2-MOE) solvent route based on a method developed by Wolf and Trolier-McKinstry (Figure 4.4) [51]. The $Pb[Zr_xTi_{1-x}]O_3$ composition was targeted close to the morphotropic phase boundary (x~0.52) due to the expected

enhancement of the ferroelectric and piezoelectric response at this composition. 10% excess Pb with respect to stoichometric requirements was added to compensate for lead's high volatility at PZT crystallization temperatures.

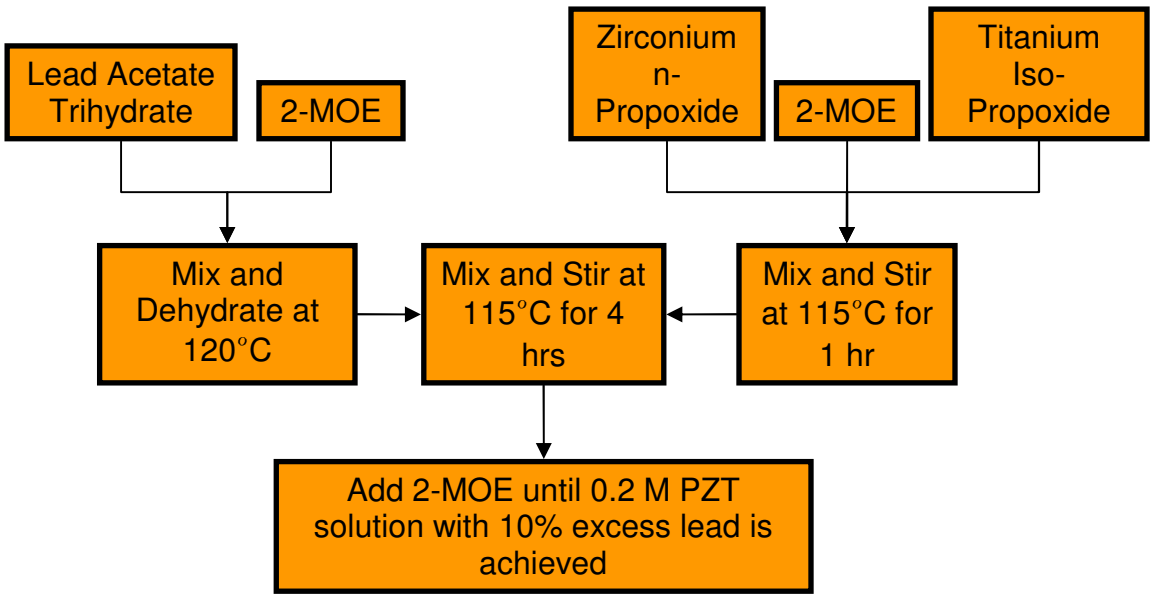

Figure 4.4: Process-flow for preparing PZT chemical solution precursor.

4.2.1 Ultrasound Bath and Vacuum Requirement

Periodic and sub-micron patterning of the polymeric template leads to a superhydrophobic behavior of its surface [121]. In order to release the trapped air and overcome the surface tension against infiltration, the template was immersed in the PZT

precursor solution under vacuum (25 in-Hg) and placed in an ultrasonic bath (Figure 4.5). Figure 4.6a shows PZT precursor accumulation on the template surface in absence of the ultrasonic bath. However, with the aid of the ultrasonic bath, the precursor solution infiltrated into the template creating cup-shaped structures within each hole (Figure 4.6b)

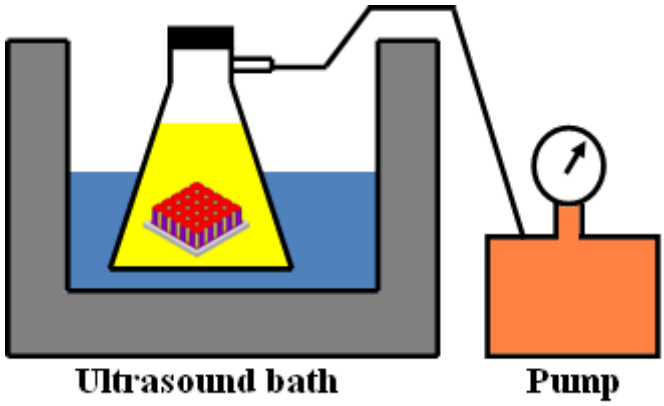

Figure 4.5: Schematic illustration of the ultrasound bath setup used for vacuum infiltration of PZT precursor solution into the soft-template.

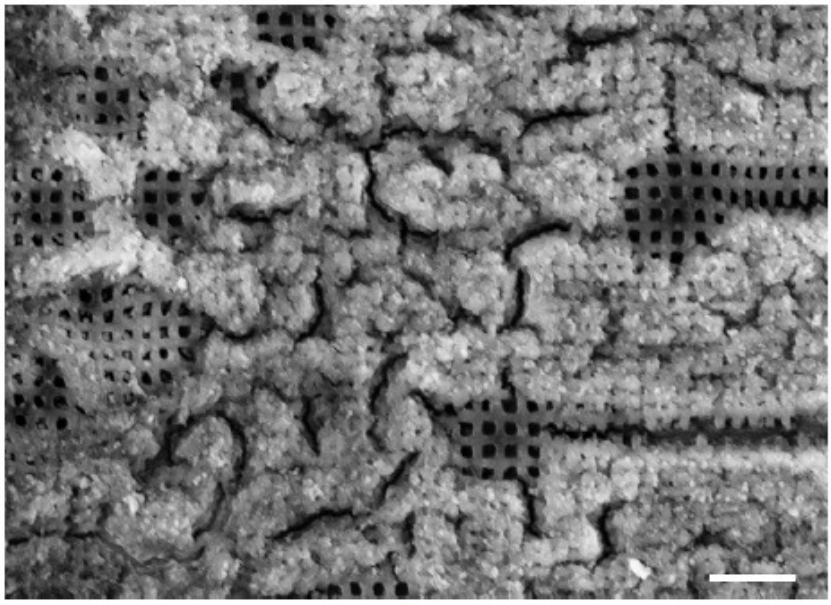

(a)

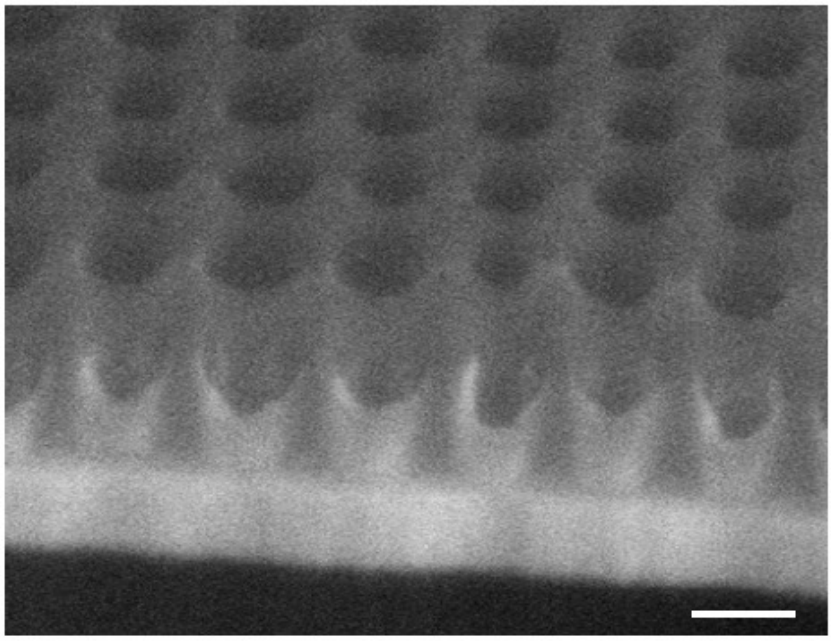

(b)

Figure 4.6: SEM images of (a) incomplete PZT infiltration under vacuum in absence of ultrasonic bath (1 μm scale bar) and (b) cross-section of PZT precursor-infiltrated templates (prior to heat treatment) obtained by focused ion beam milling. PZT "cups" are observed within each hole (200 nm scale bar).

4.2.2 Thermal Treatment

After the infiltration of the precursor solution into the template is completed (~5 min), determined by the termination of released trapped air, the sample is removed from the ultrasound bath and rinsed with 2-MOE in order to remove the excess PZT from the surface. The sample is then pyrolyzed on a hotplate at 300ºC for 1 min and annealed at 600ºC with a ramp to 800ºC at 25ºC/min. Thermal annealing led to crystallization of the PZT and decomposition of the organic resist. The resulting PZT structures are shown in Figure 4.7. Based on SEM images, the nanostructures are held together only by the ALD layer, indicating complete removal of the polymeric template during thermal treatment.

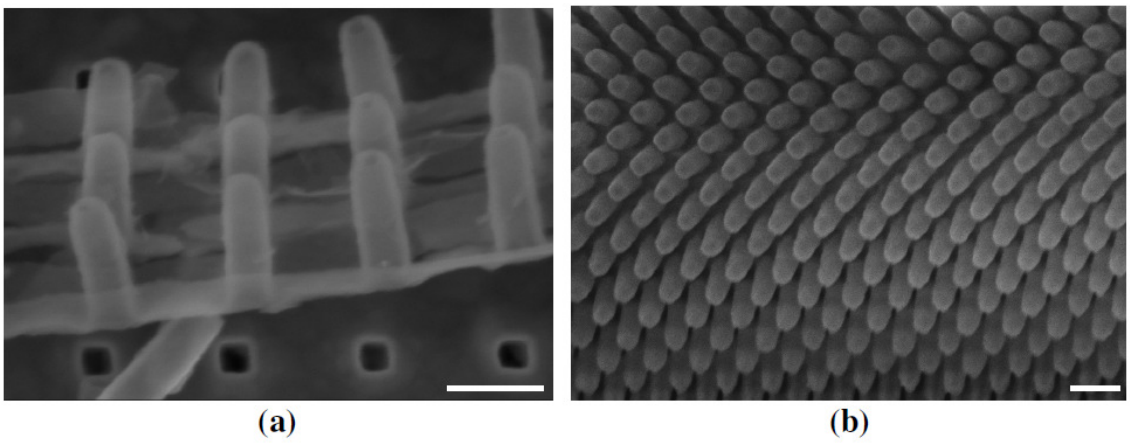

Figure 4.7: SEM micrograph of PZT nanotubes removed from the underlying substrate showing (a) a thin layer of Al_2O_3 connecting adjacent tubes and (b) complete removal of the polymeric template (200 nm scale bars).

4.2.3 Possible Al_2O_3 Removal

There are two principle etching techniques for material removal: wet etching (reactant is liquid) and dry etching (reactant is a gas). Initial attempts in this work were made to remove the thin layer connecting adjacent PZT pillars via wet etching with a 50% NaOH solution (BDH ™) (Reaction 4.1).

$$Al_2O_{3(s)} + 3H_2O_{(l)} + 2NaOH_{(aq)} \rightarrow 2NaAl(OH)_{4(aq)} \qquad \text{Reaction 4.1}$$

Wet etching was chosen due to its simplicity, lower cost, and higher selectivity when compared to dry etching. However, the isotropic nature of wet etching (Figure 4.8) caused undercutting beneath the PZT nanotube (Figure 4.9) and eventually resulted in complete release of tubes from the underlying substrate. In order to circumvent this issue, a RIE system was used. The anisotropic nature of an RIE is due to the high degree of directionality of the flux of reactive ions normal to the surface (see section 3.5).

Figure 4.8: A schematic of an (a) isotropic etch profile and (b) anisotropic etch profile.

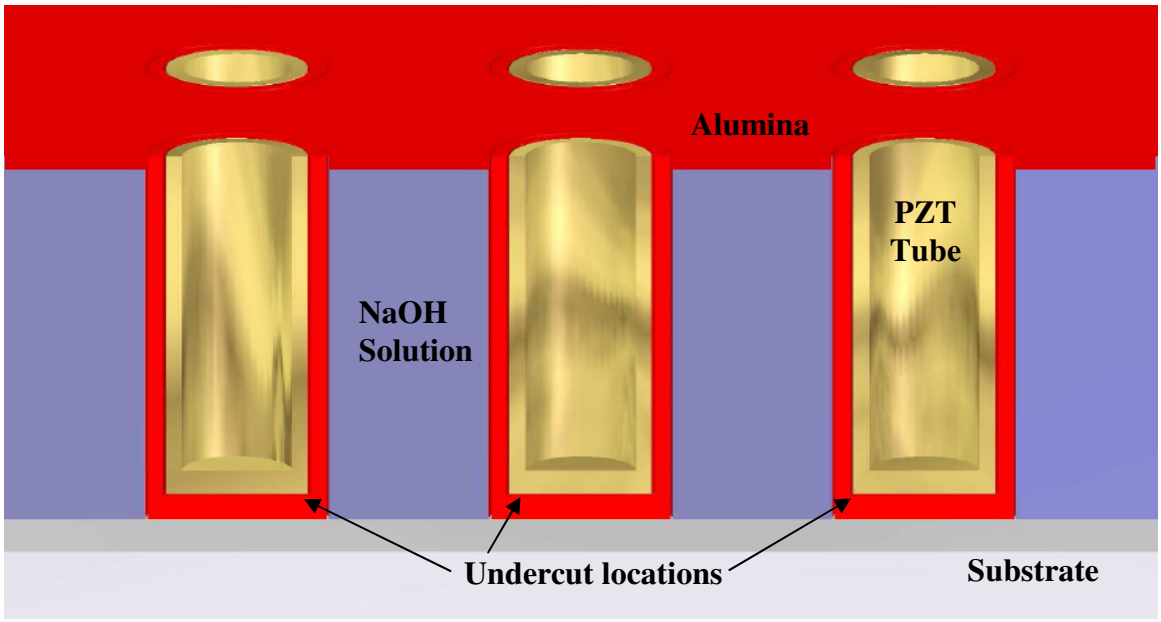

Figure 4.9: Schematic cross-section of PZT nanotube arrays illustrating undercut locations during wet etching of Al_2O_3.

The processing conditions for Al_2O_3 removal via a Vision 320 RIE (STS ™) included the following sequence of gas flows: 25 sccm CHF_3, 5 sccm O_2, and 25 sccm Ar at a pressure of 25 mT and a power of 200 W. In order to determine the etch rate of Al_2O_3, a 20 nm-thick Al_2O_3 film was deposited via the Cambridge Fiji ALD system with the exact same purge and cycle times as that used for the ALD coated soft-template. The resulting Al_2O_3 thickness was measured via a Woollam ellipsometer after a 1 min etch time. This process was repeated five times for statistical relevancy. The etch rate was approximately 1.8 nm/min ± 0.2 nm/min. This relatively slow etch rate is desirable for controllability purposes since the Al_2O_3 thickness is less than 10 nm. Faster etch rates could lead to undesired PZT damage. Figure 4.10 shows the resulting free-standing PZT

structures after Al_2O_3 removal by RIE with the aforementioned processing conditions and a total etch time of 5 minutes.

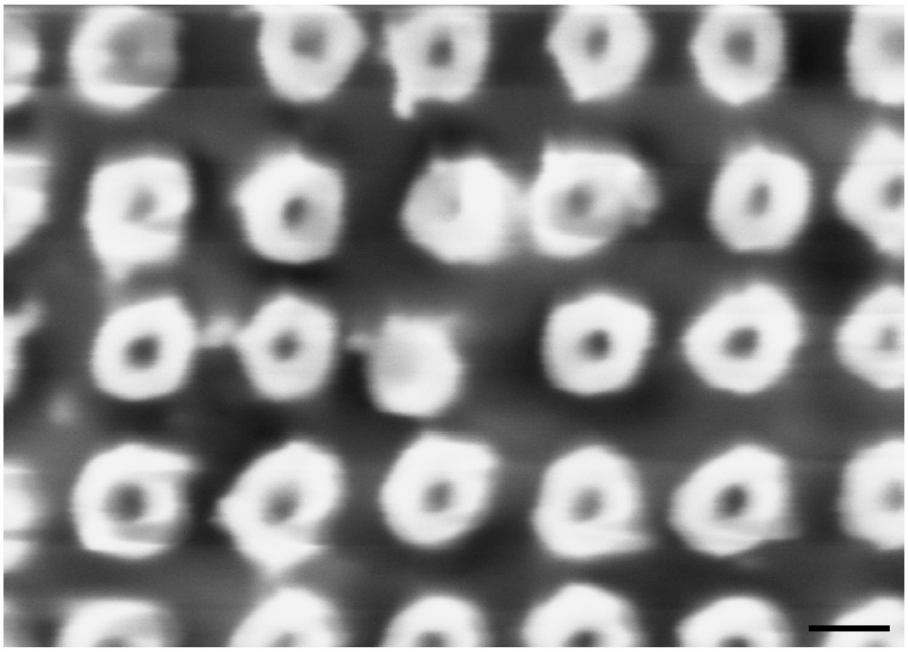

Figure 4.10: SEM micrograph showing free-standing PZT nanotubes after RIE with CHF_3 (50 nm scale bar).

4.2.4 Possible Electrode Deposition

Pt electrodes were deposited via a FIB system. A Pt precursor was introduced near the sample's surface, and the ion beam decomposed the precursor into volatile and nonvolatile products, producing a deposited layer (see section 3.9). Figure 4.11 shows SEM micrographs of Pt coated PZT nanotubes with two different precursor injection

angles. The beam current and acceleration voltage for deposition were 10 keV and 50 pA, respectively. A relatively low acceleration voltage and beam current were chosen to prevent damage to the underlying nanotubes. The precursor introduced normal to the sample's surface resulted in Pt caps on the top surface of the PZT tube with the cap diameter larger than the outer tube diameter. The precursor injected by the tip at 30^{o} from the surface normal resulted in Pt deposition primarily on the sidewalls of the nanotubes.

Figure 4.12 is an SEM micrograph of the PZT nanotubes adjacent to the targeted area for Pt deposition. Three distinct regions are shown: (1) the desired region for deposition, (2) surrounding nanotubes capped with Pt, and (3) PZT nanotubes without Pt coating. Similar regions were also observed for the precursor injected at a 30^{o} angle. The surrounding region of the nanotubes capped with Pt extends almost 1 μm away from the desired region. This Pt deposition was due to the inability to precisely control the location where the Pt precursor gas adsorbs onto the sample's surface in addition to back scattering of ions from the beam due to interactions with the underlying substrate, causing a broadening of the exposure area.

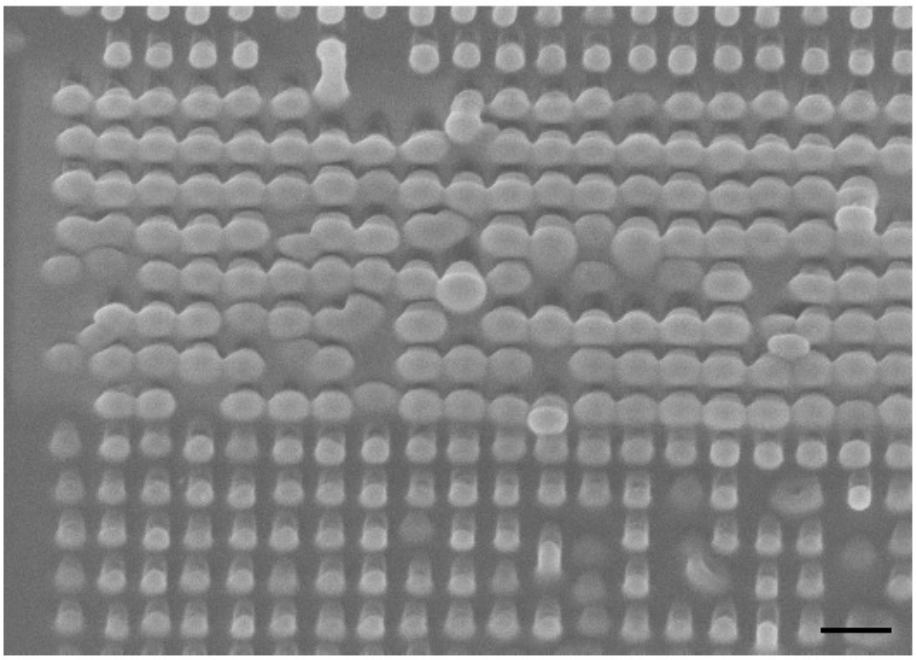

(a)

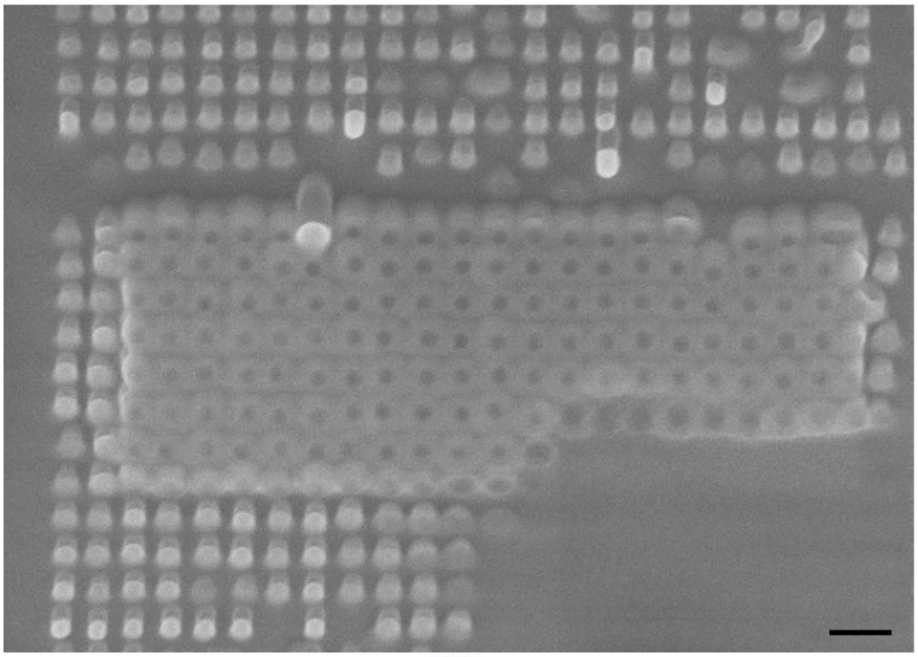

(b)

Figure 4.11: Pt deposition on PZT nanotubes via FIB with (a) precursor injected normal to sample surface and (b) precursor injected at 30^{o} from normal to the substrate (300 nm scale bars).

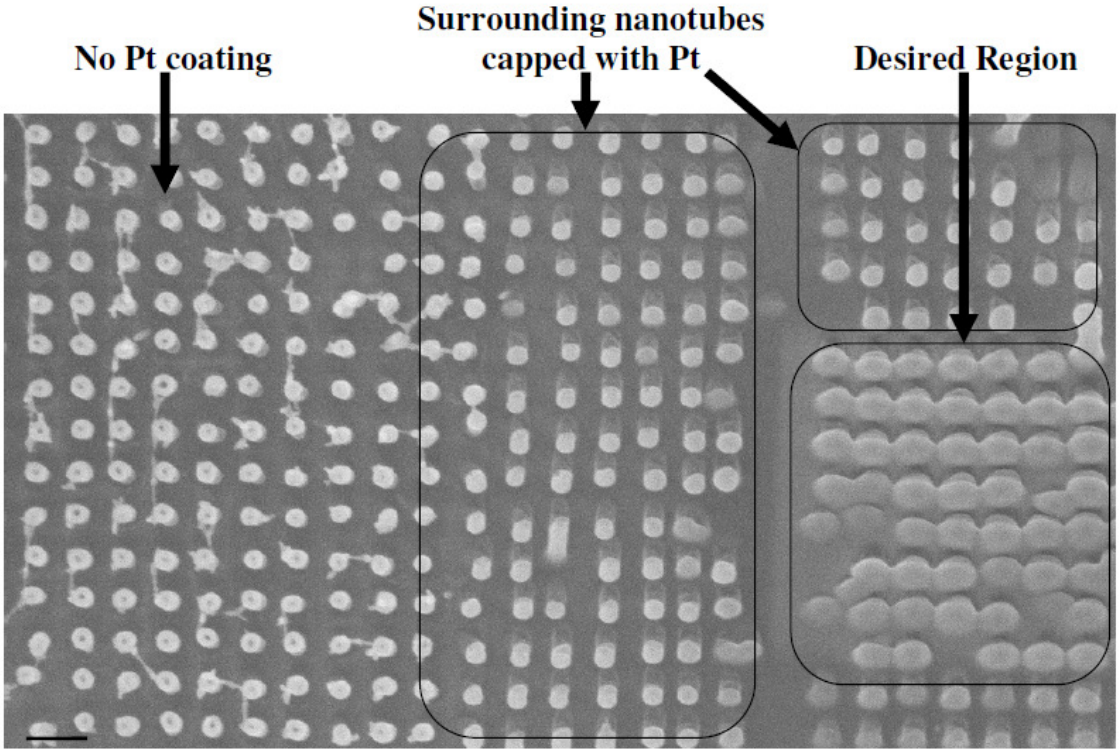

Figure 4.12: SEM micrograph showing the long range distance of Pt deposited via FIB on PZT nanotubes (300 nm scale bar).

CHAPTER 5

PZT NANOTUBE FABRICATION OPTIMIZATION

This chapter discusses optimization of the processing steps for PZT nanotube fabrication. The exposure dose for soft-template manufacturing is determined for various hole dimensions, pattern densities, and resist thicknesses. The optimal thickness of the ALD-deposited Al_2O_3 coating is also discussed. Furthermore, the heating rate and PZT crystallization temperature is optimized for perovskite phase formation, while minimizing stiction issues.

5.1 E-beam Shot Pitch and Dose Modulation

An important factor influencing pattern definition after electron beam exposure of resist is the shot pitch. The shot pitch is equivalent to a pixel (i.e. the smaller the shot pitch, the better the feature definition) (Figure 5.1). The available shot pitch is limited by the scanning frequency of JOEL JBX-9300FS EBL system (max=50 MHz). Equation 5.1 is used to determine the minimum shot pitch for a user-defined dose and current.

$$a = \sqrt{\frac{I}{fD}} \qquad \text{Equation 5.1}$$

In Equation 5.2, a is the shot pitch, I is the current, f is the scan frequency, and D is the dose. A shot pitch of 5 was used to pattern all templates, as larger shot pitches resulted in loss of pattern definition. Figure 5.2 shows an SEM micrograph of the resulting pattern

produced with a shot pitch of 8 for an original design of 100 nm wide square holes. As can be seen, the hole dimensions are very irregular with sizes ranging from 70 nm to 100 nm.

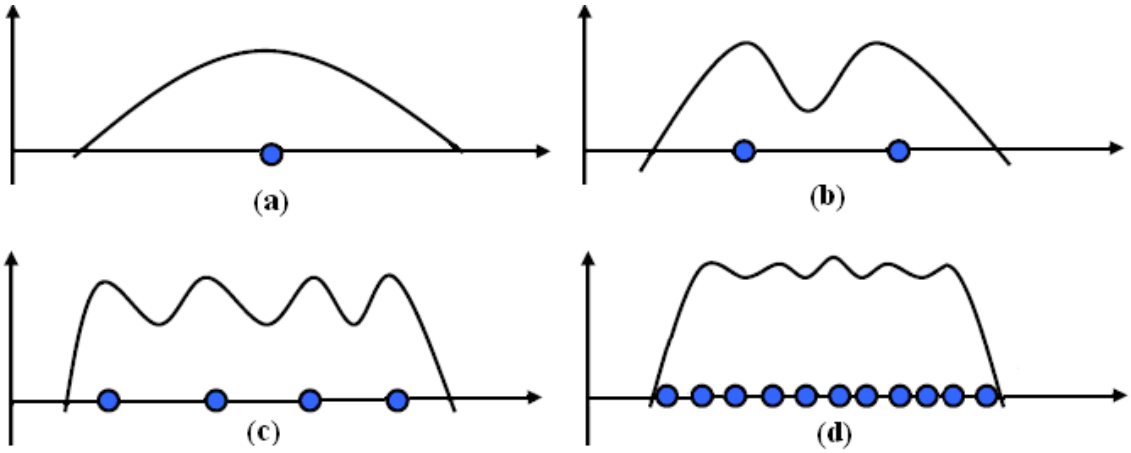

Figure 5.1: Effect of shot pitch on the energy deposition profile of a line with (a) 1, (b) 2, (c) 4, and (d) n pixels.

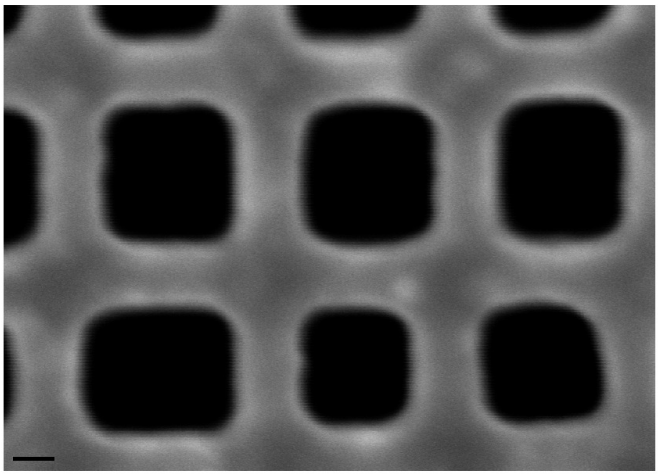

Figure 5.2: SEM micrograph of patterned ma-N 2403 with a shot pitch of 8 (30 nm scale bar).

The appropriate dose for patterning ma-N 2403 resist with a shot pitch of 5 was determined via a modulation test in which the same pattern is exposed with a range of doses. The dimensions of the resulting pattern (determined via SEM imaging) were compared with the original desired pattern to determine the optimal dose. Figure 5.3 shows results from a modulation test for creating 100 nm diameter holes with a 400 nm pitch, 500 nm resist thickness, 2 nA beam current[19], and 100 keV acceleration voltage[20]. The optimal dose modulation was -5% with respect to a base dose of 450 μC/cm^2 (i.e. ~427.5 μC/cm^2 exposure dose).

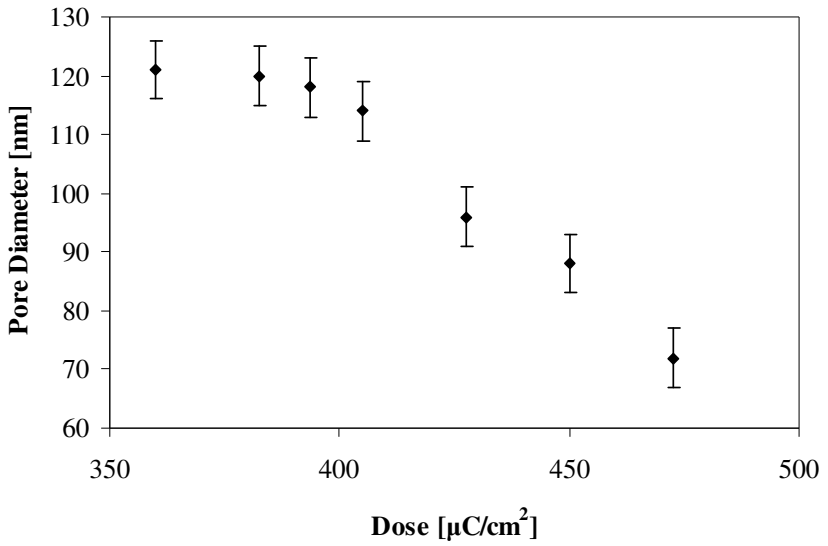

Figure 5.3: Dosage modulation results for patterning 100 nm holes with a 10% fill factor for 500 nm-thick soft-template with a 100 keV acceleration voltage and 2 nA beam current.

[19] Stochastic scattering-random electron-electron interactions broaden the beam, which is roughly proportional to the current. Lower beam currents increase resolution at the expense of throughput. A 2 nA beam current results in ~4 nm beam diameter [122].

[20] Forward scattering of electrons is highly dependent on the acceleration voltage. The range of acceleration voltages available for the JBX-9300 is 50keV to 100keV. A large acceleration voltage was chosen to minimize forward scattering at the expensive of an increase in required dose.

Dose modulation tests were performed for three pattern densities, two hole dimensions[21], and two resist thicknesses[22] (Table 5.1). The pattern density was varied by altering the pitch (Figure 5.4). The pitch is defined as the distance between the centers of adjacent holes. Because ma-N 2403 is negative resist, the pattern density (i.e. exposed area) increases as the pitch between holes increases. With increasing pattern density, the required dose decreased as expected (see section 3.3). The resist thickness range of 250 nm to 500 nm did not impact the required dose for the 100 nm holes; however, 200 nm holes required a slight increase in dose as the resist thickness increased.

Table 5.1: Optimal dose modulation for patterning ma-N 2403 with respect to a 450μC/cm^2 base dose

Resist Thickness (nm)	Hole dimension (nm)	Pitch (nm)	Modulation (%)
250	100	200	0
250	100	300	0
250	100	400	-5
250	200	400	+5
250	200	600	+5
250	200	800	0
500	100	200	0
500	100	300	0
500	100	400	-5
500	200	400	+10
500	200	600	+5
500	200	800	+5

[21] 100 nm and 200 nm diameter holes provide the capability of creating PZT nanotubes with aspect ratios (height: width) from 1.25:1 to 5:1.

[22] Resist thicknesses of 250 nm and 500 nm are the maximum and minimum resist thickness achievable via a typical spin-coater (1500 rpm and 6000 rpm, respectively). Spin coating slower than 1500 rpm resulted in large thickness non-uniformity across the wafer.

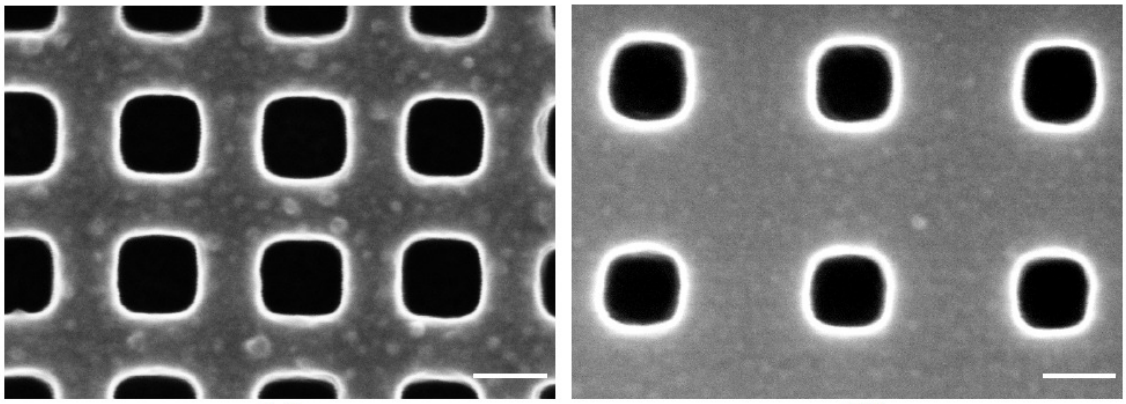

Figure 5.4: Soft-template with 100 nm holes and (a) 200 nm and (b) 300 nm pitch (100 nm scale bar).

5.2 Atomic Layer Deposited Al_2O_3 Thickness Optimization

The ALD layer is critical in creating the soft-templates as it acts as a chemical barrier and prevents chemical reactions between the solvent based precursor and the resist[23] (Figure 5.5). The ALD layer also provides mechanical consolidation during the ultrasound bath. The thickness of the Al_2O_3 layer is measured via a Woollam ellipsometer (Figure 5.6) and fitted to a Cauchy model ($n(\lambda) = A + \frac{B}{\lambda^2} + \frac{C}{\lambda^4}$). The fit parameters are detailed in Table 5.2 for 100 cycles. The quality of the fit is captured via the mean square error (MSE) value, i.e. the square of the "error", or amount the measured value differs from the model. A low MSE value (<1), such as that observed in these experiments, signifies a good fit.

[23] Information regarding maN-2403 is proprietary. Therefore, the exact chemical composition is unknown.

When performing ALD, dangling surface bonds determine how easily the precursor will passivate the surface during the first precursor pulse. If complete passivation does not occur, multiple precursor pulses may be required to obtain a continuous layer, which ultimately leads to lower thickness for a given number of cycles. Because the dangling surface bonds are possibly different for the region ultimately probed by the ellipsometer for thickness measurements (i.e. a location where Al_2O_3 was directly deposited on the platinized Si substrate), compared to the surface bonds of ma-N 2403 patterned resist[24] (which is ultimately the region of interest but too small of an area to measure via ellipsometry), the calculated ALD thickness was also verified via SEM imaging of the patterned hole's diameter in the ma-N 2403 before and after coating.

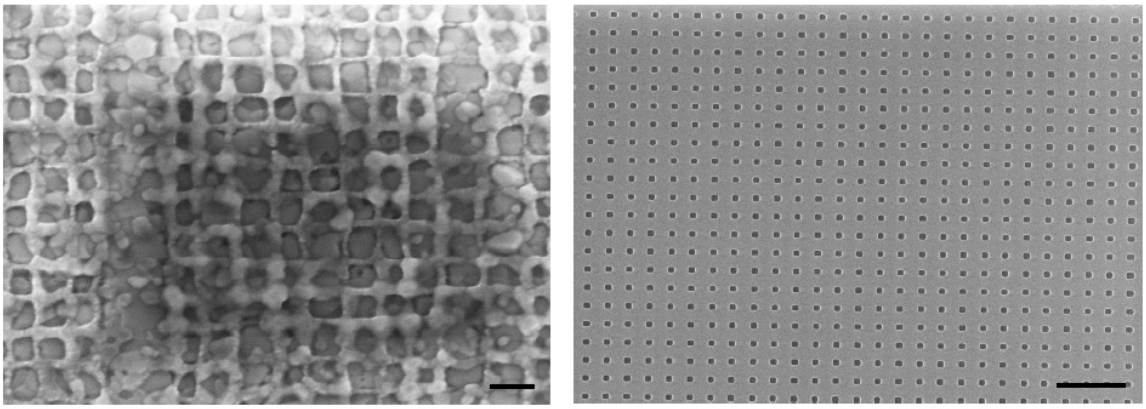

Figure 5.5: (a) Strong reaction of 2-MOE (PZT precursor solvent) with ma-N 2403 soft-template when in direct contact (i.e. without Al_2O_3 layer) (100 nm scale bar) and (b) pristine template after coating with 10 nm of aluminum oxide to prevent chemical reaction between template and PZT (1μm scale bar).

[24] Lack of dangling bonds to react with precursors can result in difficulty in atomic layer deposition.

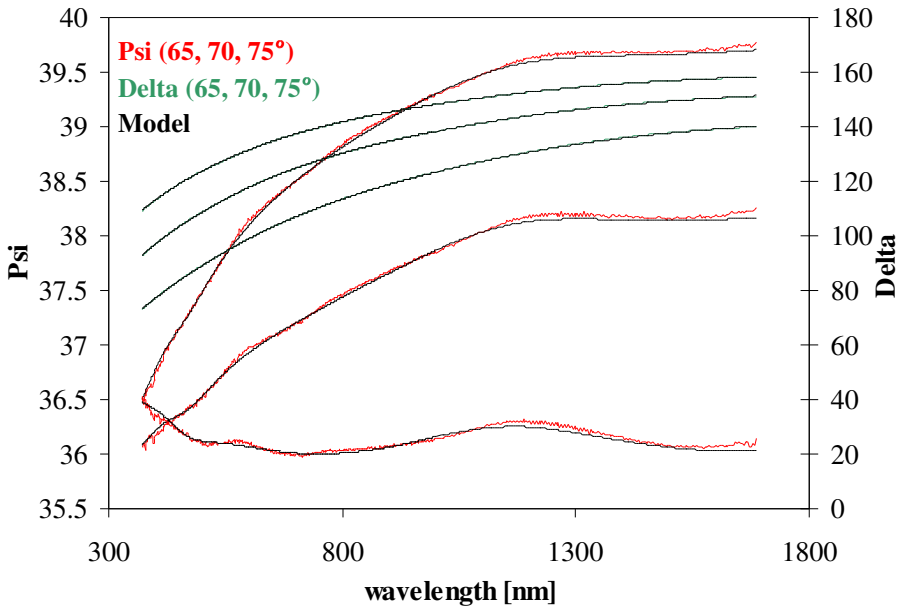

Figure 5.6: Psi and delta measurements for 100 cycles of ALD-deposited Al_2O_3 via a Woollam Variable Angle Spectroscopic Ellipsometry (VASE).

Table 5.2: Cauchy fitting parameters for 100 cycles ALD-deposited Al_2O_3

Thickness (nm)	A	B	C	MSE
9.88	1.326	0.01349	-0.00060856	0.927

10 nm was the lower boundary for the ALD layer thickness as thinner films resulted in loss of pattern definition (i.e. ripples were observed in regions between consecutive tubes and the tubes buckled) (Figure 5.7). Thicker layers of Al_2O_3 would result in an undesired increased voltage drop when performing PFM measurements (see section 6.8). In addition, as the thickness of the ALD layer increases the through pinholes decrease. These through pinholes provide means for organic vapor produced

during thermal decomposition to escape. Therefore, during thermal decomposition of the resist with 20 nm ALD-deposited coating, the lack of an escape path resulted in partial pattern release from the underlying substrate due to organic vapor pressure build-up (Figure 5.8a). In larger patterns (i.e. total pattern area of 200 μm by 200 μm instead of 50 μm by 50 μm), the increase in organic vapor pressure due to an increased amount of resist thermally decomposing resulted in the pattern bursting (Figure 5.8b).

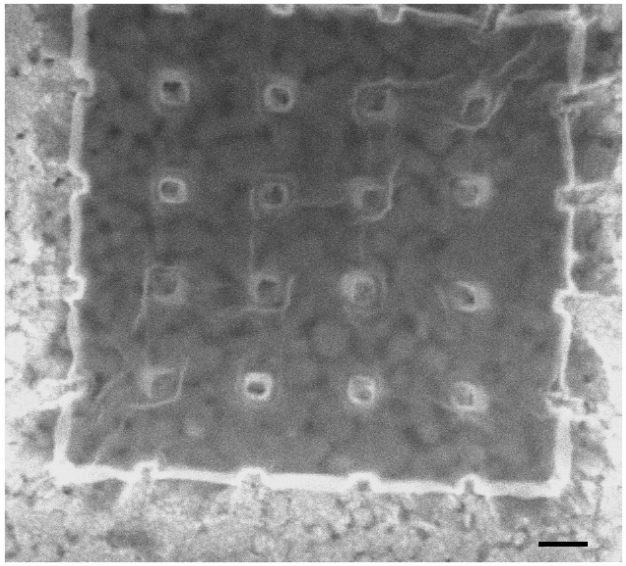

Figure 5.7: SEM micrograph of PZT-infiltrated Al_2O_3-coated template. The template was coated via ALD with 60 cycles (~6 nm thickness), resulting in loss of pattern definition (200 nm scale bar).

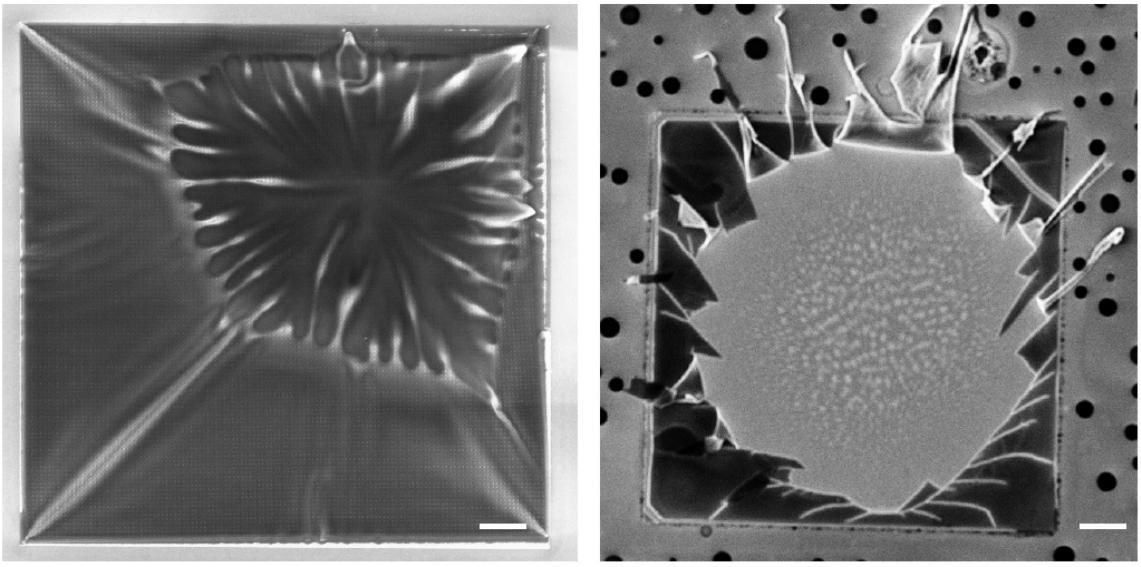

Figure 5.8: (a) SEM micrograph of pattern "lifting" from underlying substrate after heat treatment subsequent to PZT infiltration due to organic byproducts' pressure in a 50 μm by 50 μm patterned area (5 μm scale bar); (b) SEM micrograph of pattern "burst" after heat treatment subsequent to PZT infiltration due to organic vapor pressure build-up in a 200 μm by 200 μm patterned area (20 μm scale bar).

The pinhole density of the 10 nm ALD-deposited coating is demonstrated via SEM imaging of the PZT nanotubes patterned via a hierarchical patterning scheme (see section 5.5) after thermal cycling (Figure 5.9a,b). Regions with high contrast are locations where the decomposed polymer is unable to escape due to the lack of pinholes. Eventually with thermal cycling, the build-up of organic vapor in these regions resulted in pattern removal from the underlying substrate. Thus, with an increase in the overall pattern size, the increased probability that the patterned structure will posses a pin hole in which the organic vapor can escape without damaging the PZT structures. However, with larger pattern size, there is also an increase in organic vapor pressure due to an

increased amount of polymer decomposing. Therefore, optimal pattern definition is a balance between pinhole density and increased organic vapor pressure.

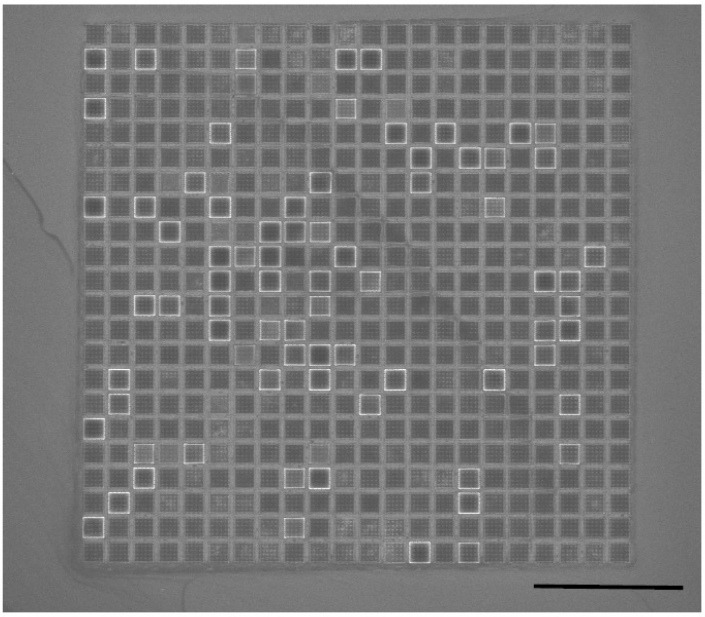

(a)

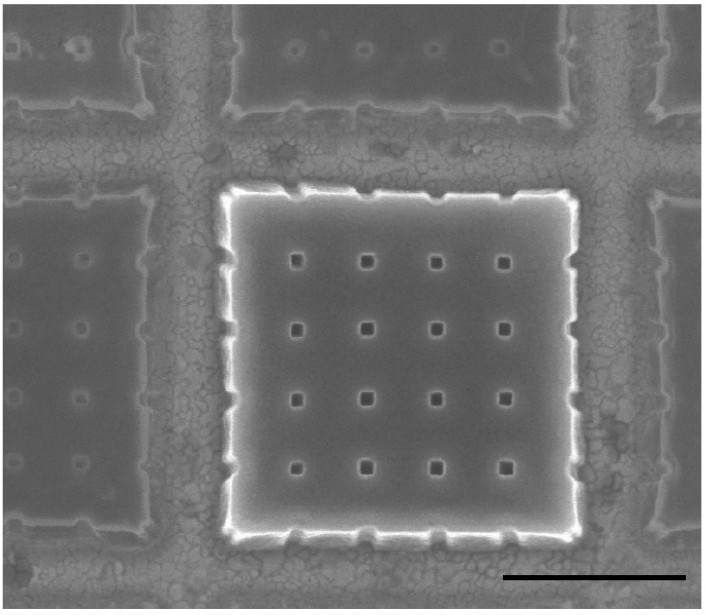

(b)

Figure 5.9: (a) SEM image of a large patterned area demonstrating the pinhole density of 10 nm ALD coating. High contrast regions lacked the sufficient density of pinholes for organic byproduct removal (10 μm scale bar). (b) Detailed view of a high contrast area where the resist was not removed during thermal treatment (1 μm scale bar).

5.3 Thermal Heat Treatment

X-Ray diffraction is the standard method used for determination of the crystallographic structure in ferroelectric bulk and thin film samples. However the small patterned area used in this work, in addition to the small amount of PZT material, renders this method ineffective. Thus, in order to determine the optimal crystallization temperature, PZT films with the same in-house prepared sol-gel solution were deposited on platinized substrates coated with a 10 nm ALD-deposited Al_2O_3 in order to emulate similar boundary conditions as the PZT nanotubes. The films were deposited via spin-coating at 4000 rpm for 60 sec followed by pyrolysis and crystallization. The deposition and heat treatment process were repeated two times to ensure a good XRD signal. The pyrolysis step helps the development of medium-range order and removes the solvent [123]. Figure 5.10 shows the effect of pyrolysis temperature on phase formation. The films were pyrolyzed at 250^{o}C, 300^{o}C, and 350^{o}C for 1 min followed by crystallization at 800^{o}C for 1 min. With increased pyrolysis temperatures, an increase in perovskite phase peaks was observed, indicating either an improved crystallinity of the final structure or an increased grain size. A 300^{o}C processing temperature for the pyrolysis step was chosen in order to ensure retention of the soft-template's pattern.

Figure 5.11 shows the x-ray diffraction patterns for films crystallized at various temperatures for 1 min. Increasing crystallization temperatures led to an increased amount of perovskite phase up to ~800 ^{o}C. Further increase in the crystallization temperature was undesirable as previous studies show a decrease in the relative amount of perovskite phase and formation of non-ferroelectrically-active secondary phases for

heat treatment at temperature ≥800°C due to increased Pb volatility at higher temperatures [124].

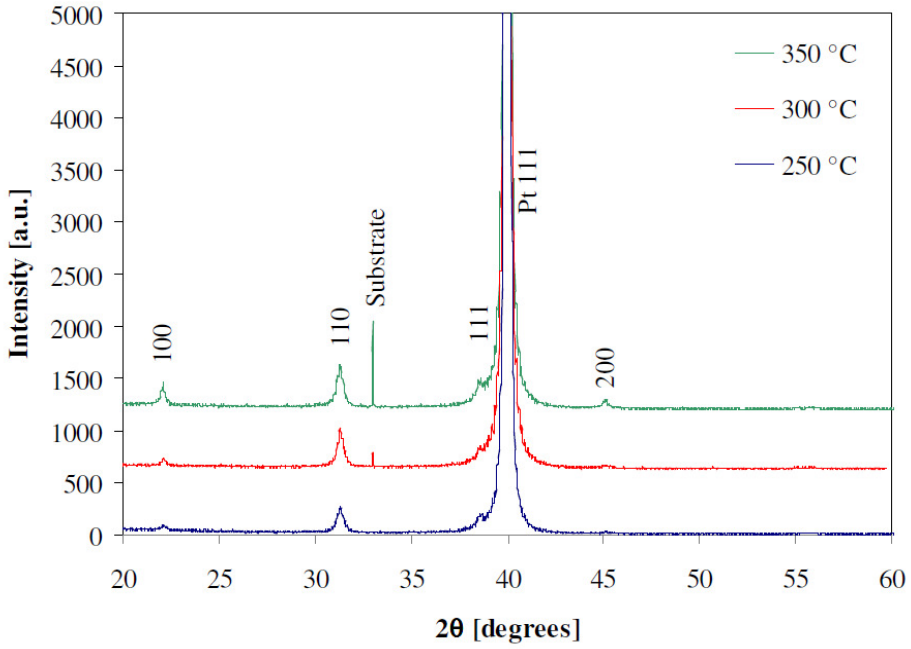

Figure 5.10: X-Ray diffraction pattern of ~45 nm-thick PZT films on Al_2O_3 coated platinized Si substrates, pyrolyzed at various temperatures for 1 min. All samples were subsequently crystallized at 800°C for 1 min.

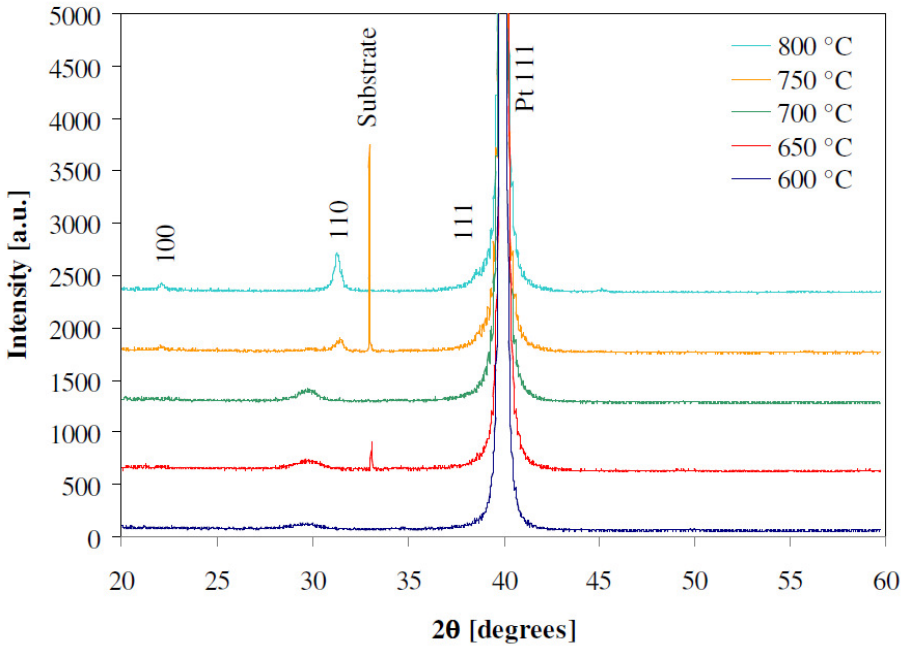

Figure 5.11: X-Ray diffraction pattern of ~45 nm-thick PZT films for samples crystallized at different temperatures. PZT films were deposited on Al_2O_3 coated platinized (100)-Si substrates and pyrolyzed at 300°C for 1 min.

5.4 Heating Rate

Rapid thermal annealing PZT nanotubes with a single-step crystallization led to stiction between adjacent PZT nanotubes. Strong adhesion forces between nanotubes formed due to rapid vaporization/removal of the organic polymer between the PZT tubes. In order to circumvent this issue, a two step crystallization process was developed which allowed a slower and more gradual decomposition of the resist and alleviation of stiction issues (i.e. slower ramp rate). The samples were initially placed in a furnace at 600°C and ramped to 800ºC at 25ºC/min. To ensure perovskite phase formation was not compromised via a two-step crystallization process, XRD was performed on PZT thin

film deposited on an Al_2O_3 coated platinized silicon wafer with such a two step process (Figure 5.13). No pyrochlore phase-related peaks were detected in the XRD pattern. Therefore, the slight increase in dwell time at higher temperature did not lead to dramatic increase in lead loss. However, a slight increase in (111) orientation of the films was observed.

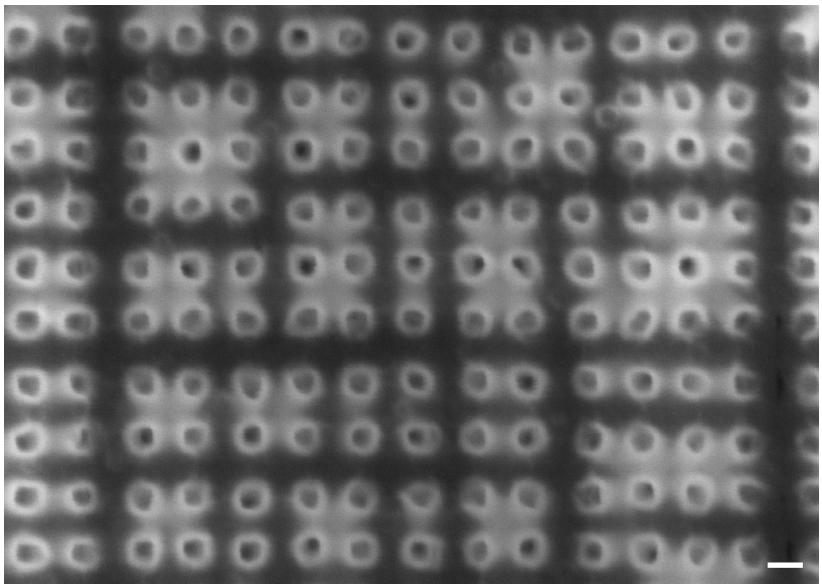

Figure 5.12: SEM micrograph of stiction between adjacent nanotubes when rapid thermal annealed in a single-ramp, single dwell time heat treatment process (100 nm scale bar).

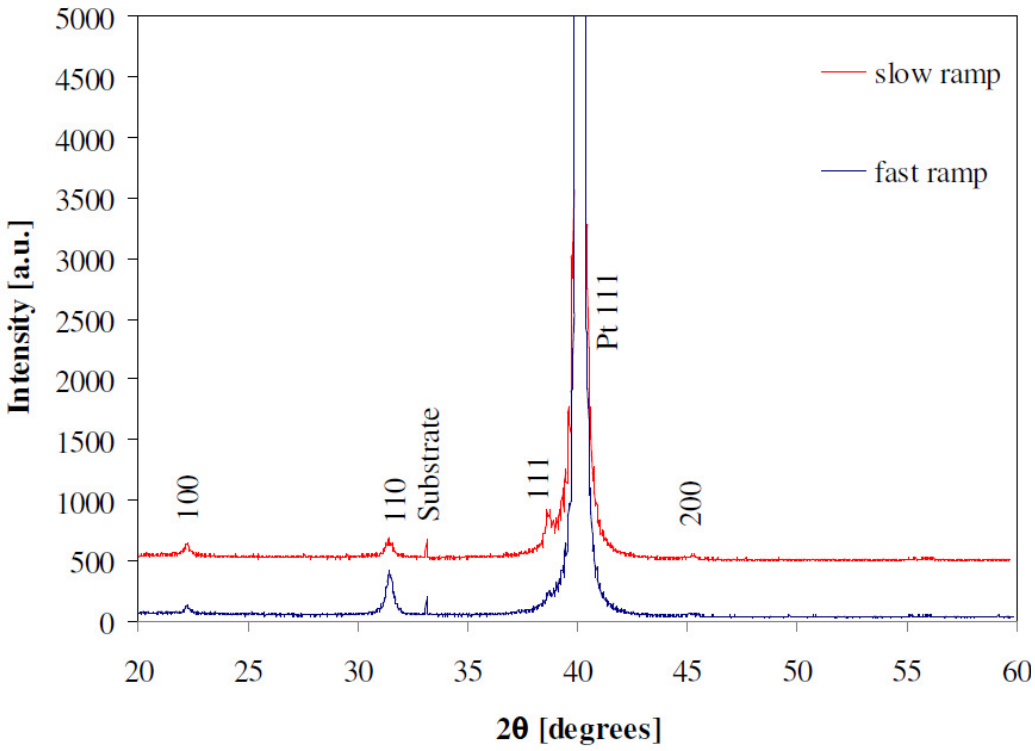

Figure 5.13: X-Ray diffraction pattern of ~45 nm-thick PZT films on Al_2O_3 coated platinized Si substrates, pyrolyzed at 300°C for 1 min and crystallized with two heating rates.

5.5 Hierarchical Patterning Scheme

Delamination and cracking were observed in many samples after the thermal treatment, when the total pattern area was superior to 10 μm x 10 μm. It is expected that organic decomposition of the soft-template during the high temperature anneal can lead to creation of residual stress in the nanostructures, causing the observed delaminating and cracking (Figure 5.14a). Observation of the cracking patterns and dimensions of the crack-free locations, showed the presence of a natural stress accumulation and release pattern, suggesting a redesign of the polymeric templates' organization. Gaps were

added between patterned features at similar distances as the cracks that appeared in the original template to alleviate stress (Figure 5.14b).

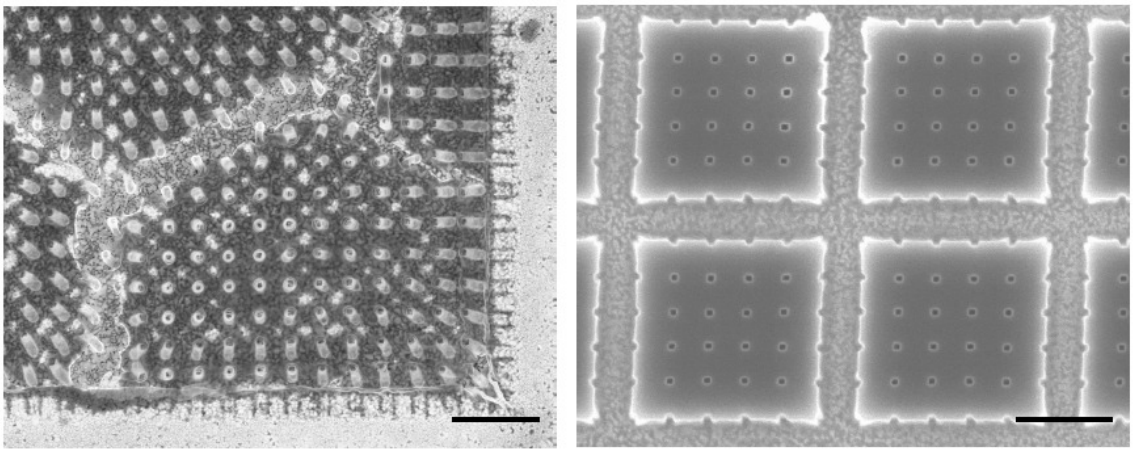

Figure 5.14: (a) Surface cracking due to residual stress formation in large patterned area, and (b) hierarchical patterned area eliminating surface cracking and delamination (1μm scale bar).

Additional stresses in the structures are due to ferroelectric distortion at the Curie temperature, as well as thermal expansion coefficient mismatch between the PZT, Al_2O_3, and the substrate. To help alleviate the stress concentration at sharp corners of rectangular patterned features (Figure 5.15a), hexagonal patterns were later developed (Figure 5.15b).

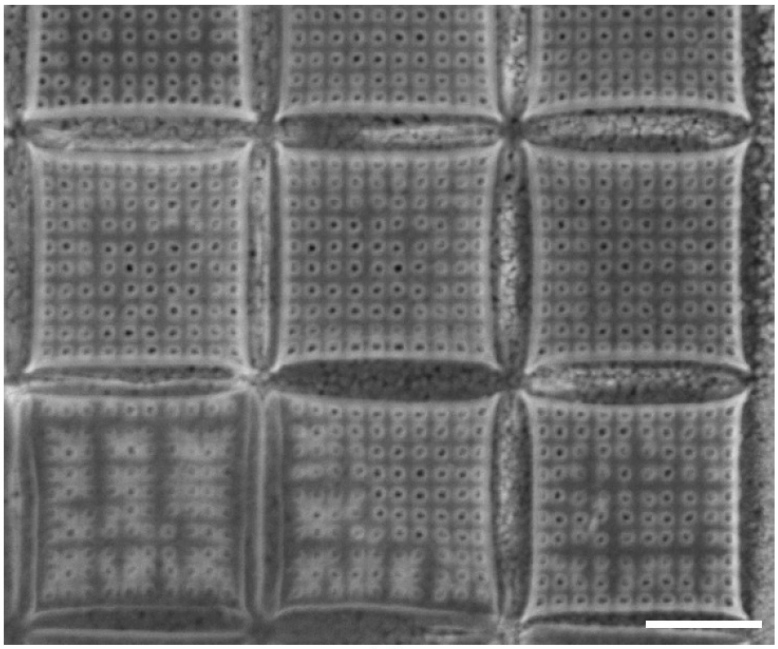

(a)

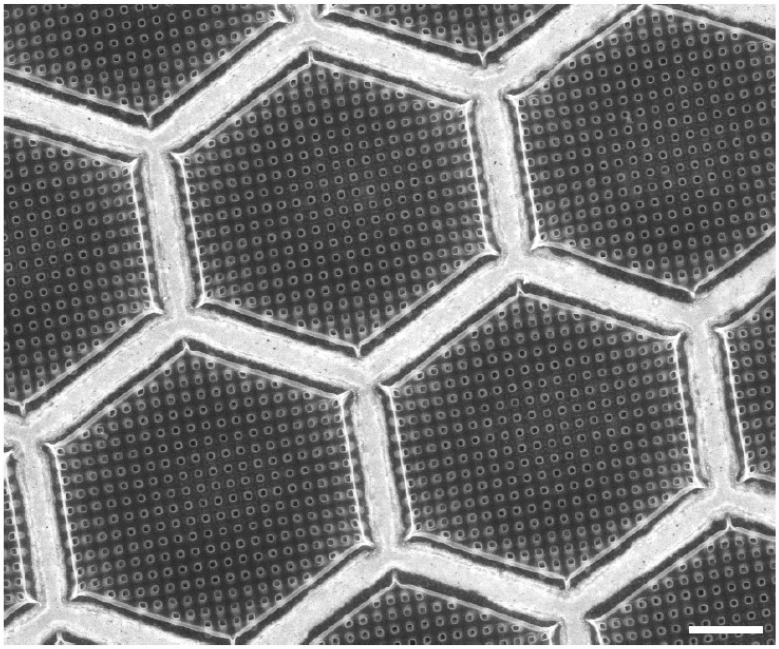

(b)

Figure 5.15: SEM micrograph of PZT nanotubes arrays with (a) square and (b) hexagonal hierarchical patterning scheme. The square patterning scheme had pulled-in edges, while the hexagonal pattern retained its shape (1μm scale bar).

CHAPTER 6

PZT NANOTUBE CHARACTERIZATION

This chapter details the characterization of PZT nanotubes in terms of chemical composition, crystallographic structure, and basic piezoelectric response. Crystallographic information regarding the PZT tubes is obtained via micro-Raman microscopy by comparison with reference PZT thin films, while EDS analysis was performed to verify chemical composition. In addition, characterization of the piezoelectric and ferroelectric nature of the tubes was performed via piezoresponse force microscopy.

6.1 Reference PZT thin film preparation

Throughout this chapter, PZT thin films are used for reference for several different measurements. Films were prepared on platinized Si wafers, with and without 10 nm Al_2O_3 coating, with PZT thicknesses ranging from ~20 nm to ~250 nm in order to emulate the wall thickness and height of the nanotubes, respectively.

The PZT films were deposited by spin coating the same PZT sol-gel precursor as the nanotubes at 4000 rpm for 1 min onto platinized Si substrates, followed by pyrolysis and crystallization at the exact processing conditions as the PZT nanotubes. The spin coating and thermal treatment sequence were repeated as needed until the desired film thickness was achieved (Figure 6.1). To measure the resulting film thickness, the edge of

each sample was etched by a 10:1 aqueous NH_4: HF etchant solution (buffered oxide etchant, BOE). The created step, i.e. film thickness, was measured via a Veeco Dektak 150 Surface Profilometer (stylus contact). Additionally, the etched corner allowed for contact to the bottom electrode for the subsequent PFM measurements. The film thickness as a function of layers deposited is shown in Figure 6.2.

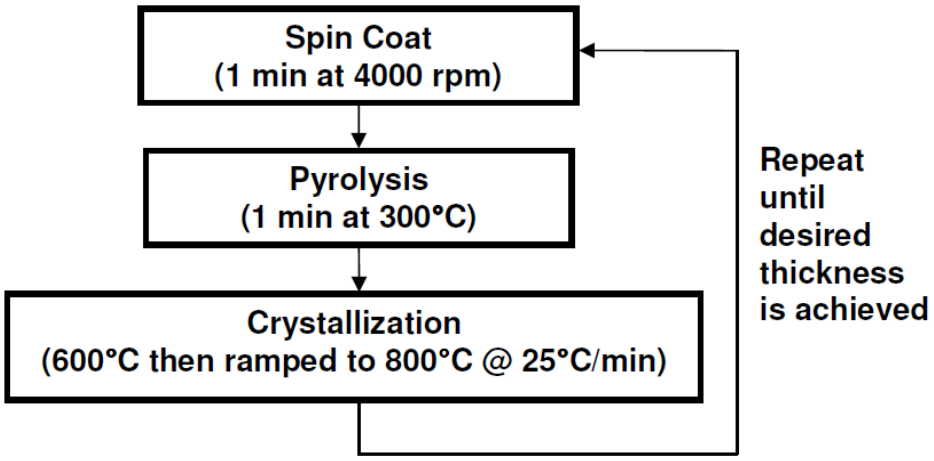

Figure 6.1: Flowchart illustrating PZT thin film deposition steps.

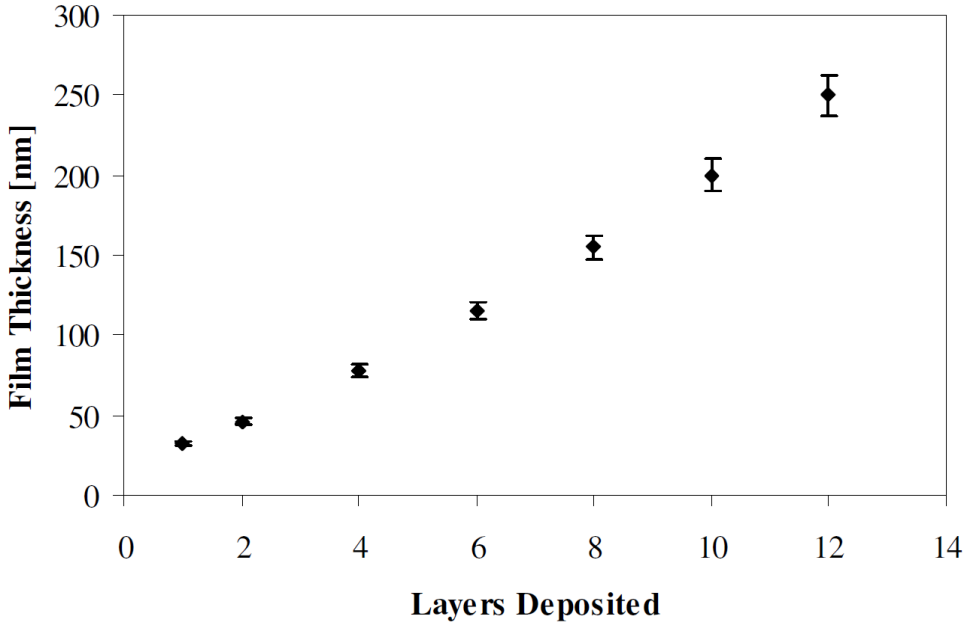

Figure 6.2: PZT film thickness as a function of number of layers deposited using a 0.2 M precursor solution and spin coating at 4000 rpm for 1 min.

6.2 Chemical Composition: EDS Analysis

To verify the chemical composition of the 0.2 M PZT precursor solution prepared in-house, energy-dispersive x-ray spectroscopy (EDS) was performed on a reference PZT film deposited on a platinized Si wafers. PZT thin films were used for chemical analysis as the tool's resolution is volume limited, thus preventing the direct use of PZT nanotubes due to their small volume of PZT.

The EDS spectra for a 200 nm PZT film at an acceleration voltage of 20 keV is shown in Figure 6.3 and the data are tabulated in Table 6.1. Si and Pt energy peaks are from the underlying substrate. Based on the atomic percentages from the EDS spectra,

the ratio of Zr to Ti with respect to Pb is ~58/49. The targeted composition was 52/48, close to the morphotropic phase boundary due to the expected enhancement of the ferroelectric and piezoelectric response at this composition. The measured atomic percentage of Ti matches the desired percentage (<2% error), however the measured atomic percentage of Zr compared to the targeted composition has a much larger disparity (13% error). The excess Zr detected with respect to stoichometric requirements is possibly due to the energy peak overlaps of Pt's M_{α} peak (2.050 keV) (underlying substrate) and Zr's L_{α} peak (2.042 keV), which causes the relatively large uncertainty (i.e. weight % σ>5 for Zr and Pt) and could possibly lead to an artificially high Zr reading.

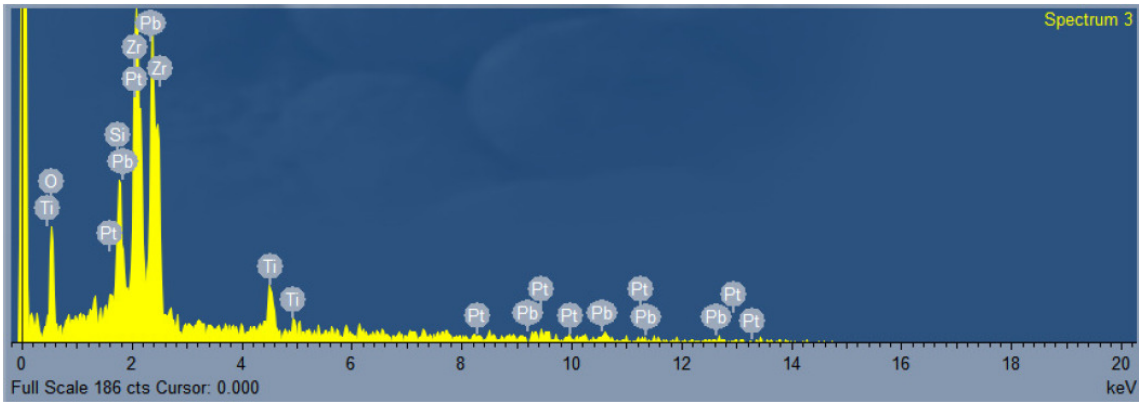

Figure 6.3: EDS spectra of a 200 nm-thick PZT thin film deposited on a platinized Si substrate.

Table 6.1: EDX elemental analysis of a 200 nm thick PZT thin film deposited on a platinized Si substrate.

Element/Peak	Weight%	Weight% σ[25]	Atomic%
O K_α	0.18	0.03	58.23
Si K_α	0.05	0.02	8.72
Ti K_α	0.06	0.02	6.38
Zr L_α	0.14	0.08	7.65
Pt M_α	0.23	0.10	6.02
Pb M_α	0.53	0.05	13.01

6.3 Micro-Raman Spectroscopy

The crystallographic structure of the PZT nanotubes was characterized by micro-Raman spectroscopy (Figure 6.4). Spectra from 270 nm-thick PZT thin film (similar thickness to PZT nanotubes' heights and phase-verified via x–ray diffraction) were used for reference. Because micro-Raman is a volume sensitive technique, the micro-Raman spectra of the PZT nanotubes was slightly attenuated; however, the spectra matched relatively well with (100)-orientated PZT thin films with peaks at 120 cm^{-1}, 190 cm^{-1}, and 280 cm^{-1}. The locations of the observed peaks are consistent with those reported by Burns and Scott for perovskite PZT [125].

[25] Weight% σ is the standard deviation used to quantify the uncertainty in the weight percentage for each element detected.

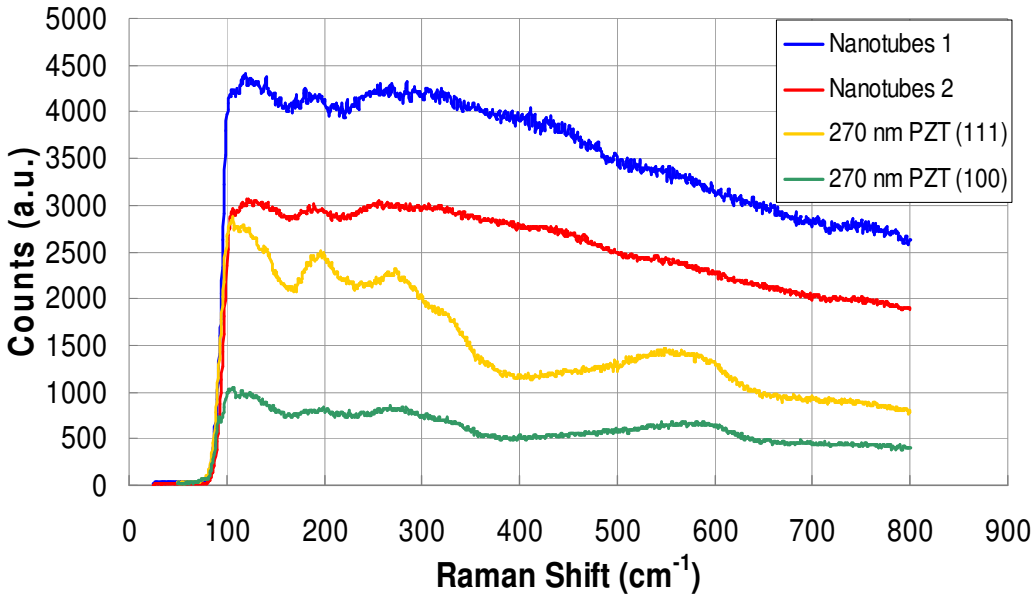

Figure 6.4: Micro-Raman spectra for PZT nanotubes and PZT thin films with thickness similar to the nanotubes' height.

6.4 Piezoelectric Force Microscopy Limitations and Challenges

The piezoelectric and ferroelectric nature of the PZT nanotubes was characterized via PFM (see section 3.13). In typical PFM scans, a single excitation frequency is used. However, the high aspect ratio of the PZT nanostructures, in addition to the piezoelectrically-active nature of the PZT vs. inactive nature of the alumina layer, led to large variations in the contact resonance frequency, causing the piezoresponse to be a function of the chosen excitation frequency (Figure 6.5). Use of BE-PFM allows deconvolution of the piezoresponse from the chosen excitation frequency via collection

of the response amplitude at resonance[26] for each point in a scanned image, leading to more accurate characterization of the structures.

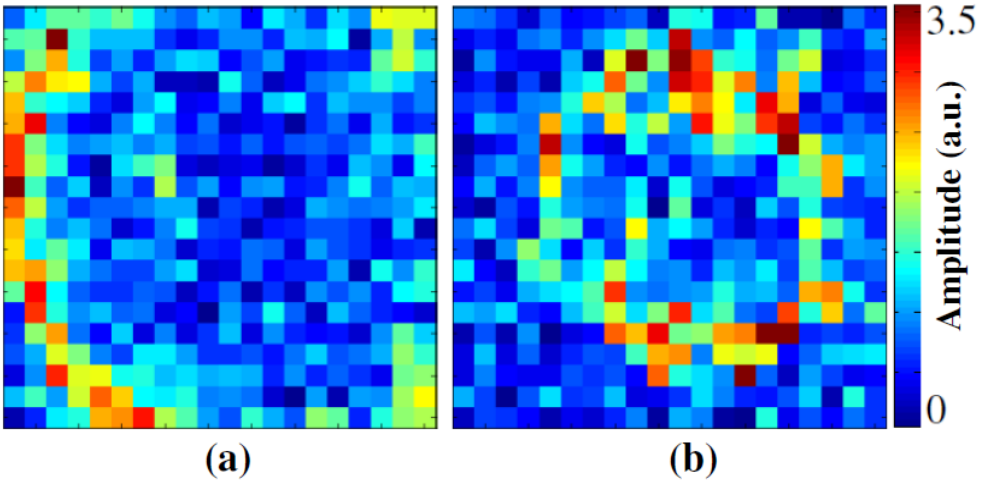

Figure 6.5: PFM amplitude response for a single PZT nanotube (300 nm by 300 nm scanned area) measured at 3 V_{ac} and (a) 255 kHz and (b) 275 kHz, showing a clear convolution of the piezoresponse with the excitation frequency.

One limitation of any scanning probe technique is the ability to correctly trace the structure's topography. A large-area AFM scan of the nanotubes showed that the conical-shaped AFM tip is unable to trace the bottom of the high aspect ratio tube (Figure 6.6). Also, the apparent width of protruding features (in this case, PZT nanotube walls) is broadened by approximately the diameter of the probes (Figure 6.7) [126], and sharp

[26] During BE-PFM, the piezoresponse for a specific location is measured for a band of frequencies. An algorithm is then used to find the frequency with the maximum strain response (i.e. contact resonance frequency).

step-like topographical features are registered as more gradual inclines/declines with the slope determined by the AFM tip's sidewalls.

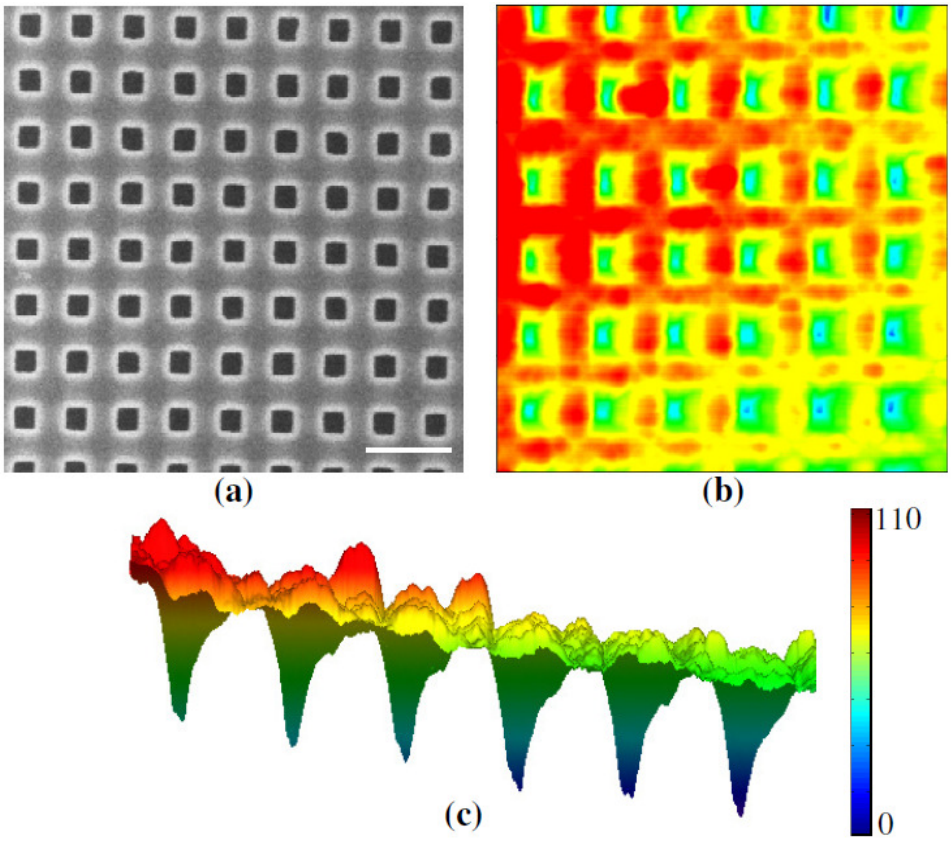

Figure 6.6: (a) SEM image of the 135 nm-wide, square-shaped PZT nanotubes (500 nm scale bar). AFM contact mode topography scan of a 2 μm x 2 μm of the same sample in (b) top view and (c) cross-sectional view (scale in nm). The fact that the slope is not symmetric suggests asymmetry in the AFM tip's sidewalls.

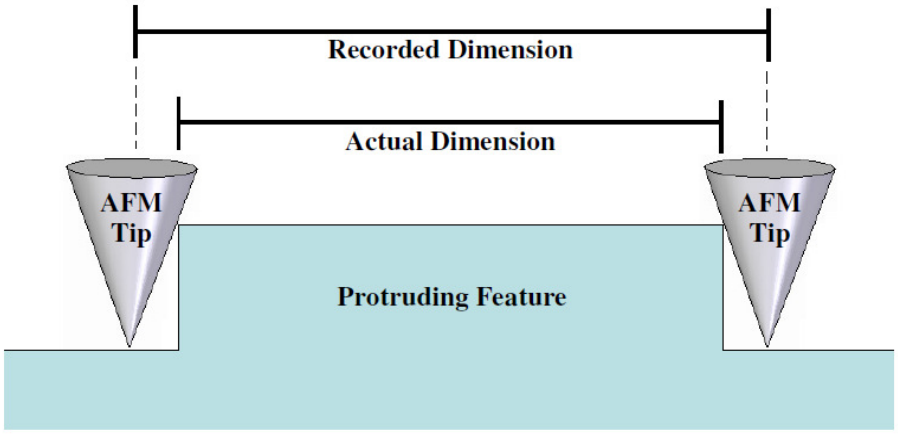

Figure 6.7: Illustration of the overestimation of the width of the protruding features during an AFM scan.

Completely free-standing pillars (Al_2O_3 layer moved via RIE (see section 4.2.3)) presented further difficulties for AFM-based measurements. During contact mode scanning (necessary for BE-PFM or SS-PFM analysis), as the tip scanned over the structure, the tip's force caused the structure to bend and eventually break (Figure 6.8). Attempts were made to circumvent this issue by lowering the contact setpoint. However, a contact setpoint less than 0.4 V resulted in the tip losing contact with the structure, which was made evident by the loss of topography information and the z-scanner voltage[27] maxing out. Thus, all PZT PFM scans were performed on PZT nanotubes connected via a 10 nm-layer of alumina unless otherwise noted.

[27] The z-scanner voltage is a read-out of the voltage applied to piezoelectric motor, which controls the height of the cantilever's base.

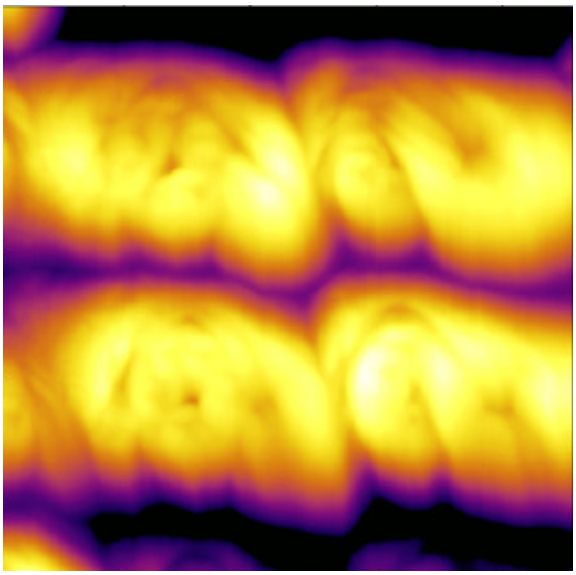

Figure 6.8: AFM contact mode topography scan (top-view) of 500 nm x 500 nm area with 100 nm-diameter, free-standing PZT nanotubes. The bottom of the tube is fixed to the underlying substrate while the top of the PZT nanotubes undergoes bending (in this scanned region from right to left) due to the force applied by the AFM scanning tip.

6.5 BE-PFM PZT Nanotubes in Hollow Alumina Matrix vs. Semi-freestanding

Figure 6.9 shows the BE-PFM response of PZT nanotubes with 100 nm outer diameter, 4:1 aspect ratio, and ~10 nm wall thickness. Adjacent tubes were connected by a continuous 10 nm-thick layer of alumina. The amplitude of the PFM response on a PZT nanotube was 8 times larger than on the suspended alumina film, which is expected due to PZT's piezoelectric nature. The maximum PFM response corresponded to the inner portion of the tube. In such a configuration, i.e. the AFM tip in contact with the inner top edge of the nanotube, the registered PFM response can be a mixture of longitudinal and radial piezoelectric excitation of a free-standing tube. Based on the spatial resonance frequency plot, the resonant frequency changed by more than 30 kHz

on the scanned region, therefore stressing the importance of performing BE-PFM rather than single frequency PFM.

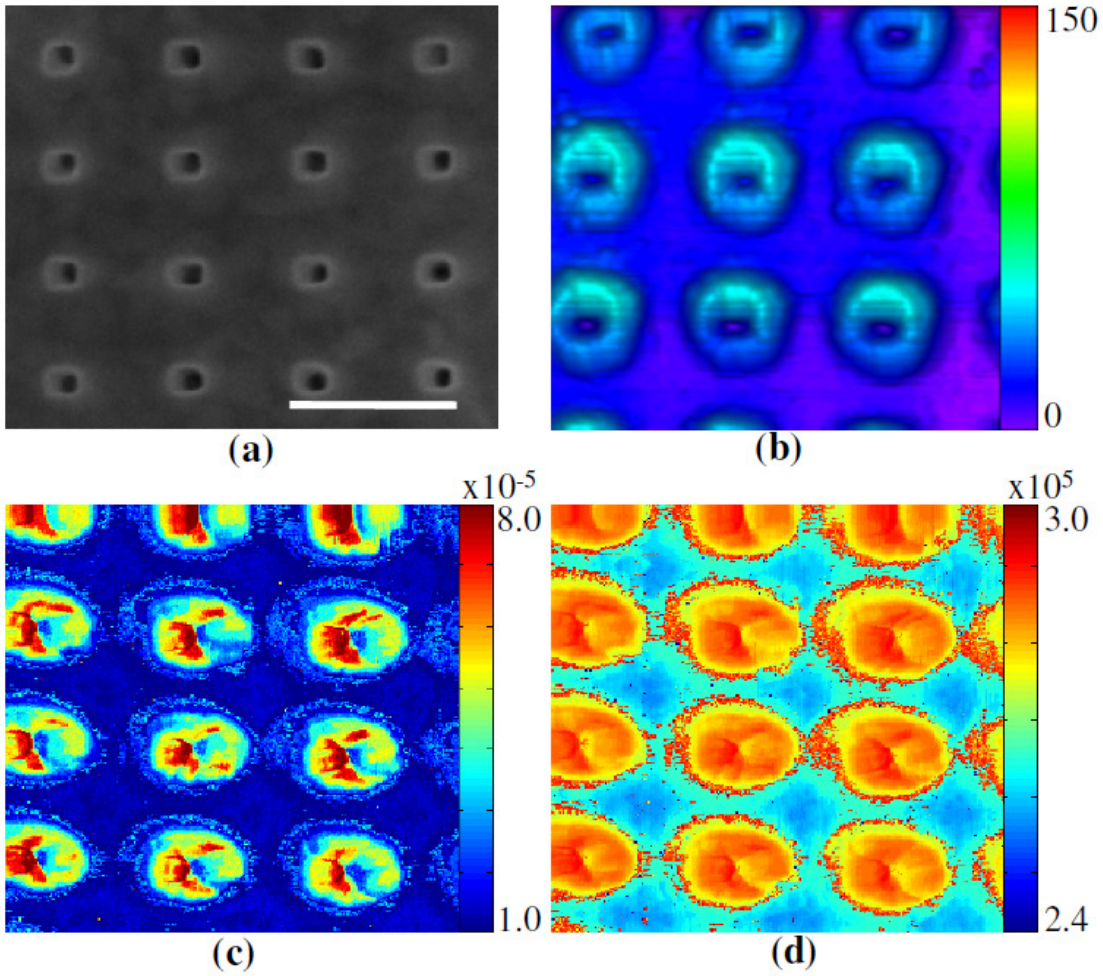

Figure 6.9: BE-PFM output response for 100 nm-diameter PZT nanotubes with a 4:1 aspect ratio connected by a 10 nm-layer of alumina. (a) SEM micrograph of PZT nanotubes with a 400 nm pitch between adjacent tubes (500 nm scale bar). (b) AFM topography scan (nm scale), (c) amplitude response (arbitrary units), and (d) resonance frequency (Hz scale) for PZT nanotubes with a 200 nm pitch between adjacent tubes. All AFM-based scans are 600 nm by 600 nm.

The BE-PFM response for "semi-freestanding" nanotubes with similar diameter, aspect ratio, and tube thickness is shown in Figure 6.10. These nanotubes were "released" from the Al_2O_3 film due to cracking around the top outer edge of the nanotubes, specifically at the corners of each nanotube, which is consistent with stress concentration regions. Higher than average stress could have developed due to a residual PZT layer on the top of the surface Al_2O_3 layer. Residual stress can develop in such bilayers due to the thermal expansion coefficient mismatch between PZT and Al_2O_3 when cooling from the high processing temperatures. Excess surface PZT is also consistent with the relatively large PFM response observed in the regions between adjacent PZT nanotubes and is probably due to incomplete removal of surface PZT during the 2-MOE rinse. For these semi-freestanding nanotubes, as opposed to the PZT nanotubes connected by the thin alumina layer, the maximum PFM response was recorded in an outer edge region of the tubes. The topography was underestimated in the same regions by the AFM. It is probable that the two effects (underestimated topography and large piezoelectric response on the outer edge of the nanotubes) are correlated and caused by the AFM tip pushing through the cracks on the top PZT/Al_2O_3 layer, and becoming entrapped in the crack in the proximity of the nanotube. As the tip then attempts to ascend the steep sidewall of the tube, the force of the AFM tip causes the tube to bend[28], resulting in a "measured" reduced topography as well as a larger contact area between the tip and the tube. The improved contact reduces the voltage drop at the tip-to-sample junction and ultimately results in a higher piezoelectric response due to an increased electric field in this region.

[28] Unlike the completely free-standing tubes previously discussed, the amount the tube bends is somewhat limited by the surrounding matrix.

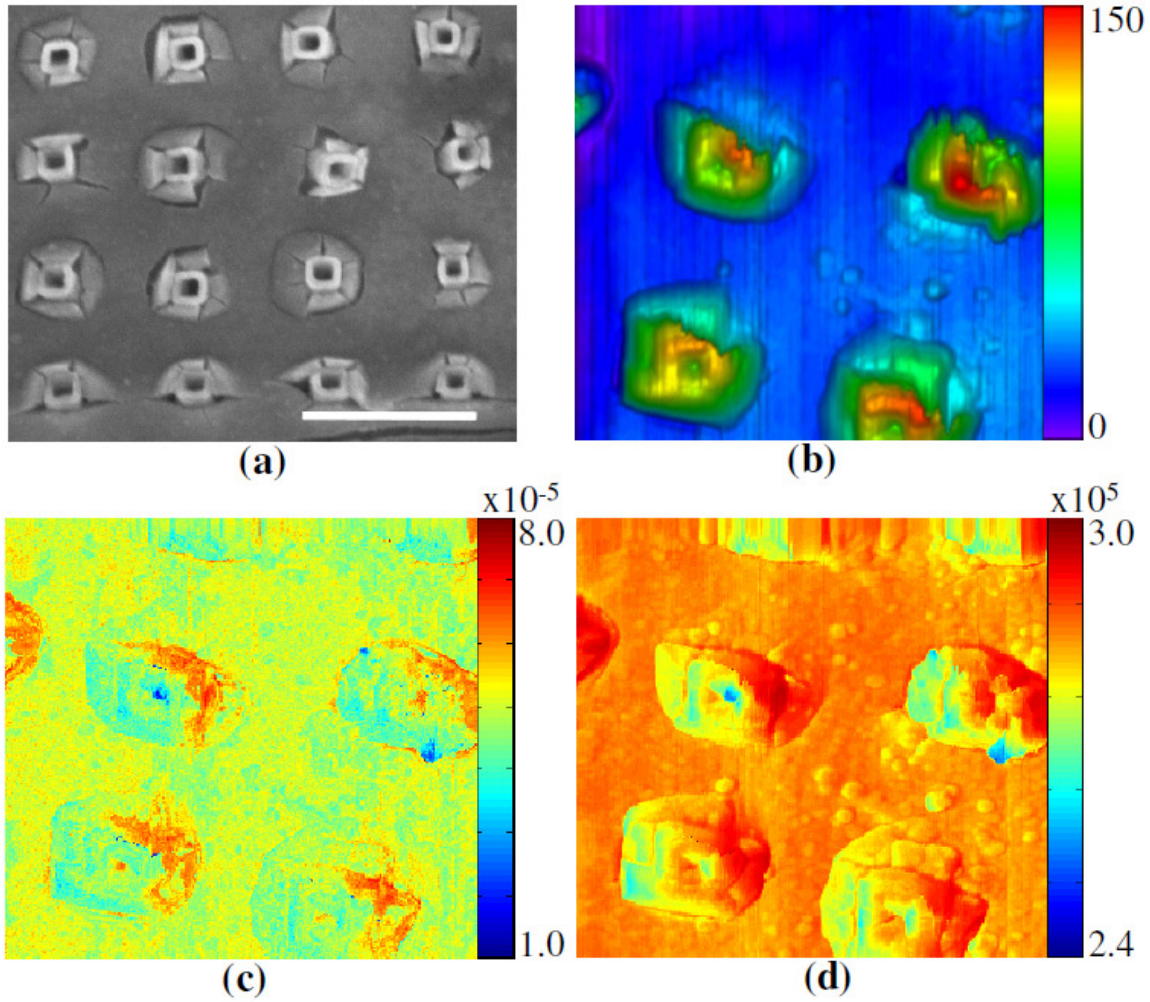

Figure 6.10: BE-PFM output response for 100 nm diameter semi-freestanding PZT nanotubes with a 4:1 aspect ratio. (a) SEM micrograph (500 nm scale bar), (b) AFM topography scan (nm scale), (c) amplitude response (arbitrary units), and (d) resonance frequency (Hz scale). All AFM scans are 800 nm x 800 nm.

6.6 BE-PFM Write and Read Experiment

The ferroelectric nature of the nanotubes was demonstrated by write and read experiments. The samples were first scanned with positive or negative DC voltages (+15 V_{dc} and -15 V_{dc}, respectively). The BE-PFM amplitude response was recorded after each applied bias (Figure 6.11). The resonance frequency remained substantially unchanged,

while the amplitude of the PFM response showed a clear change with the sign of the bias voltage applied (i.e. write voltage), which is evidence of ferroelectric behavior[29]. An invariable resonance frequency is indeed expected, as it is mostly governed by the mechanics of contact between the AFM tip and sample, as well as the topography of the sample itself. The variation of the PFM amplitude with the sign of the write voltage could indicate either the presence of a strong internal bias[30] in the PZT nanotube or the applied voltage was below the saturation value. Indeed, at saturation, the amplitude of the PFM response should be identical for positive and negative write voltage.

[29] If no change in the strain-response was recorded, then the study would have been inconclusive as the applied DC voltage could have been large enough that saturation occurred. Therefore, another scan set would have had to be performed with a lower +/- V_{dc}.

[30] Studies in thin films indicate that internal bias is mainly due to an internal space charge fields resulting from trapped electronic charges near the ferroelectric-electrode interface. Oxygen vacancies associated with defect dipoles can enhance charge trapping and thus leading to an increase in internal bias [127].

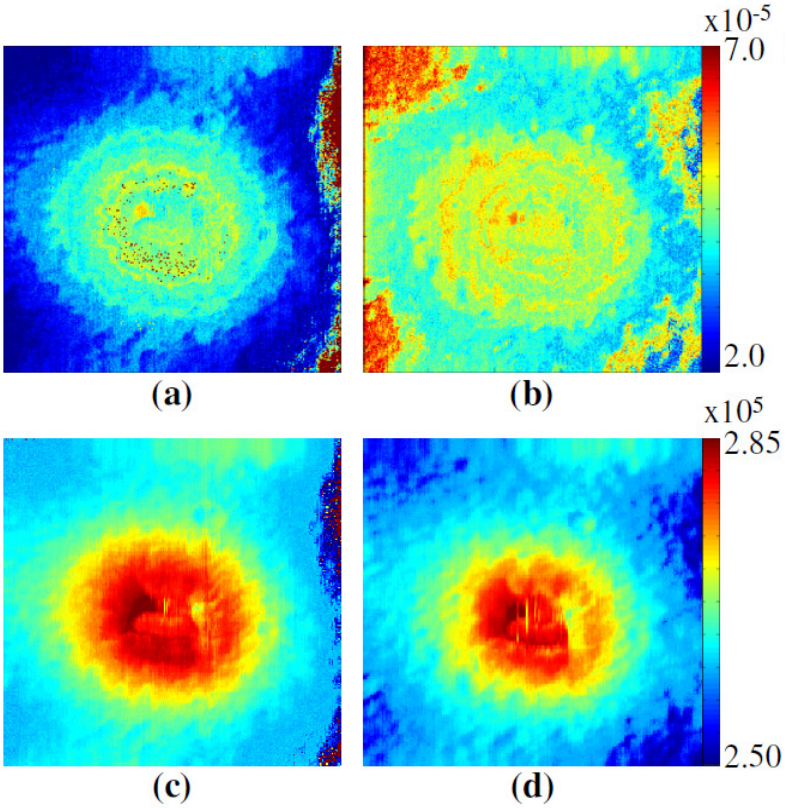

Figure 6.11: BE-PFM response for a 300 nm by 300 nm scanned area illustrating (a,b) amplitude response and (c,d) frequency response after poling the PZT nanotube at (a,c) +15 V_{dc} and (b, d) -15 V_{dc}.

6.7 SS-PFM

To further study the switching behavior of the nanotubes, electromechanical hysteresis loops were collected by measuring the PFM amplitude and phase response of a single PZT nanotube after applying a DC bias in a triangular waveform (SS-PFM) (see section 3.13.3). The change in amplitude (A) and the phase (Ψ) at resonance after each applied DC bias are a direct result of the nucleation and growth of domains. The piezoelectric response (*PR*) is determined via Equation 6.1.

$$PR = A_{max} \sin\psi \qquad \text{Equation 6.1}$$

The phase and amplitude were recorded after DC bias removal to avoid complications associated with the DC bias dependence of the piezoelectric response, as a large enough DC bias can stabilize the domains configuration [128].

The average phase, amplitude, and piezoresponse were determined for the on-tube and inside-tube locations (Figure 6.12). The on-tube location demonstrated a typical butterfly-like electromechanical response and phase saturation, corresponding to ~180^o switching. The above observations, in addition to a saturated hysteretic piezoresponse, suggest ferroelectric behavior for the on-tube location. The asymmetry observed in the butterfly loop for the on-tube locations is a clear indication of bias, which is consistent with the results of write/read experiments (see section 6.6). The bias is possibly due to dissimilar boundary conditions between top and bottom electrodes and/or an internal bias, due to presence of point defects or asymmetry in the Al_2O_3/PZT configuration within the probed sample. It is also noteworthy to add that the presence of a butterfly-shaped strain-voltage curve for the inside-tube locations is consistent with an almost continuous contact between AFM tip and the tubes across the scanned area. As previously discussed, the AFM tip is not capable of complete tracking of the features and can not fully penetrate the nanotubes (Figure 6.6). Therefore, the observed butterfly-loop piezoelectric response is partially a measure of the lateral excitation of the nanotubes.

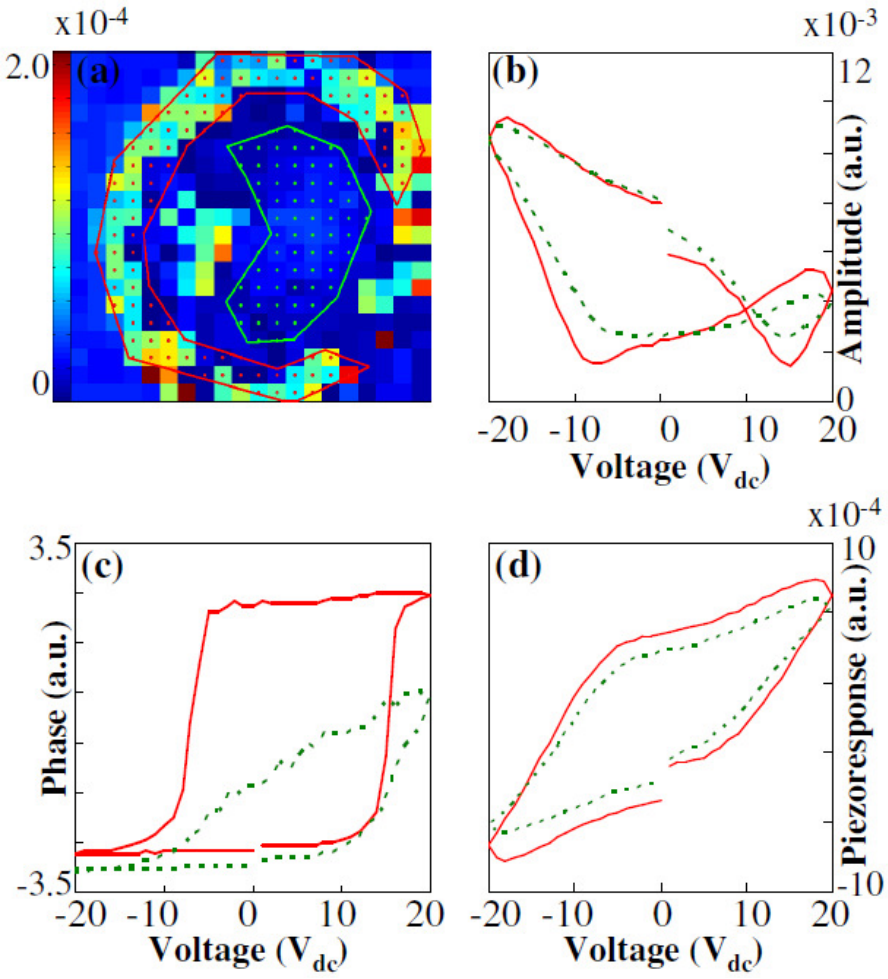

Figure 6.12: SS-PFM response of a single PZT nanotube: (a) amplitude at resonance resolved-spatially under a 20 V_{dc} applied voltage, illustrating the areas for the averaged response shown in (b-d); and (b) amplitude, (c) phase, and (d) piezoresponse for on-tube average response (solid red) and inside-tube average response (dashed green) with 20 V_{dc} amplitude triangular wave applied.

Figure 6.13 shows the piezoresponse loops for on-tube locations with increasing DC bias excitations. The measured switchable response (area inside the piezoresponse curve) represents the change in electromechanical response due to alterations of the domain state within the probed region. The switchable response is limited for small

electric field ranges, which is expected for excitation fields below the coercive field. As the excitation bias increased, larger volumes of the PZT beneath the AFM probe switched as indicated by the progressive opening of the hysteresis loops.

SS-PFM data was also collected for reference templates simply coated with Al_2O_3 (without PZT) with increasing voltage from 0 to 60 V_{dc}. No hysteretic response was observed in these electromechanical measurements (Figure 6.14), thus suggesting that the measured response for the PZT tube is due to the converse piezoelectric effect and not electrostriction or geometric anomalies.

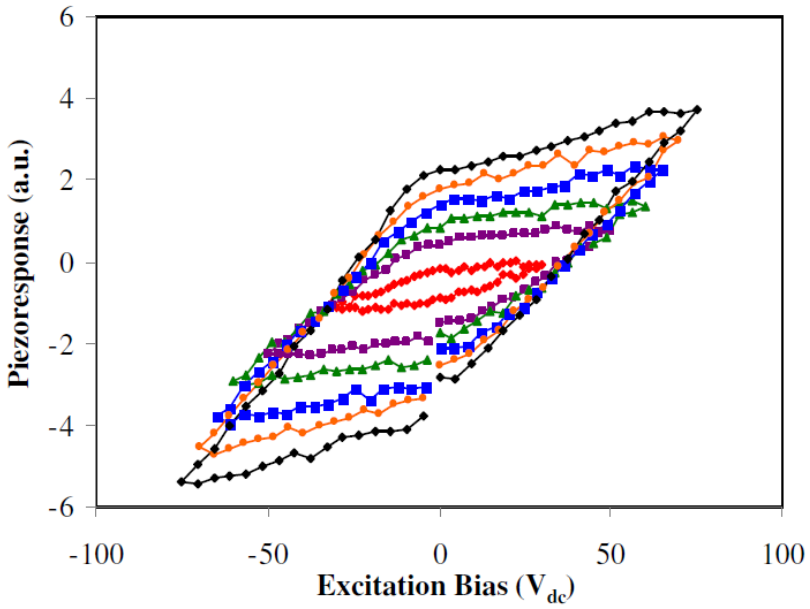

Figure 6.13: Piezoresponse hysteresis loops for on-PZT-tube locations with increasing excitation bias.

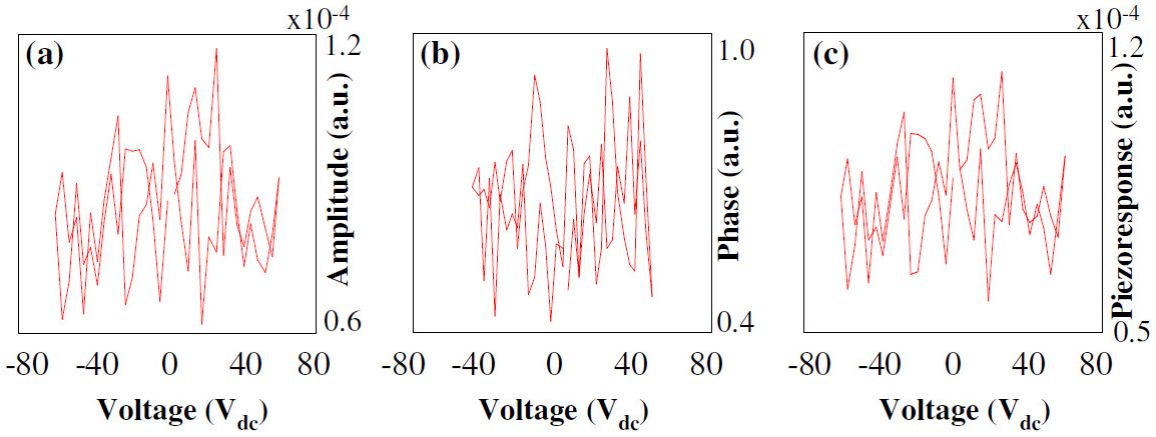

Figure 6.14: SS-PFM output response for reference templates simply coated with Al_2O_3 (without PZT) (a) amplitude, (b) phase, and (c) piezoresponse, showing complete absence of piezoresponse signal even from higher order electrostrictive behavior.

6.8 Comparison of SS-PFM for PZT Nanotubes vs. PZT Thin Films

In order to explore the cause of the relatively high DC bias voltages necessary for switching the PZT nanotubes, SS-PFM data was collected for reference PZT films and compared to the PZT nanotubes (Figure 6.15a,b). The measured coercive voltage in the PZT film was nearly one order of magnitude lower than in the PZT nanotubes. Previous studies have shown that the presence of a low permittivity layer, such as impurities, between the PFM tip (electrode) and ferroelectric materials can lower the effective electric field in the ferroelectric [90, 129]. However, both thin film and nanotube configurations have low permittivity Al_2O_3 present in the material stacks between the bottom Pt electrode and PZT material, thus the origin of such large variation in the coercive voltage need to be sought elsewhere.

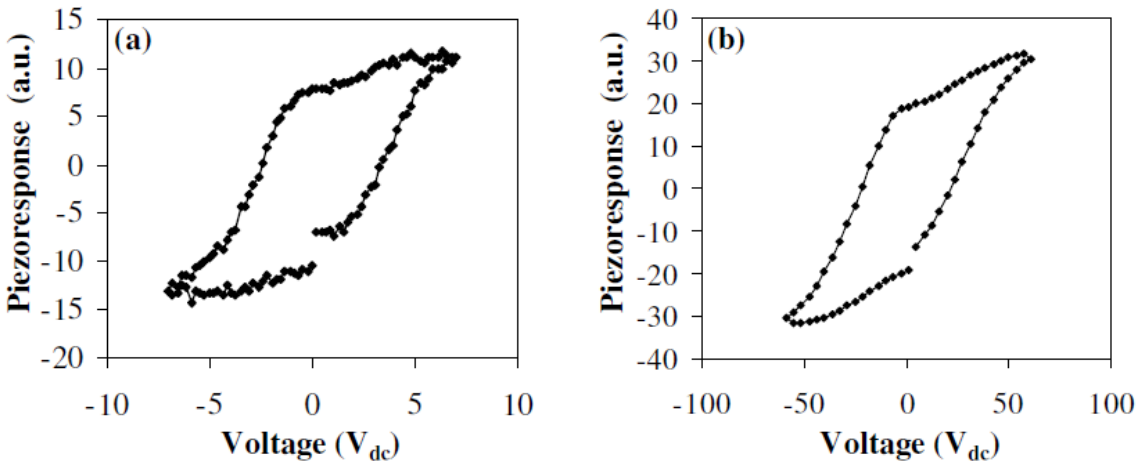

Figure 6.15: Measured SS-PFM piezoresponse for (a) ~250 nm-thick PZT film and (b) ~250 nm-high PZT nanotube with 20 nm wall thickness.

To study the electric field distribution through the thickness with a very localized top electrode (AFM conductive tip), finite element models (COMSOL Multiphysics®) of the electric field distribution in the vicinity of the tip were performed for the thin film and PZT nanotube configurations (Figure 6.16a,b). The following boundary conditions were used in the simulations: zero potential at the bottom surface (i.e. platinized silicon substrate) and zero charge at distances infinitely far away from the PZT tube/film. The AFM tip was modeled as a 30 nm diameter Pt disk, and the voltage drop between the AFM tip and the bottom electrode was set at 1 V. The electric field distribution in the PZT nanotube showed a sharp drop in potential at the Al_2O_3/PZT interface, with the electric field mostly concentrated in the alumina layer (Figure 6.17b). This concentration of electric field in proximity of the Al_2O_3 for the nanotubes is due to the dramatic differences in the relative dielectric permittivities of the PZT (ε_r =750) and alumina (ε_r

=12). For the PZT thin films, no such field enhancement in the alumina layer is observed due to the film's infinite lateral dimension (Figure 6.17a).

During the SS-PFM scans, the electric field created in the ferroelectric materials in contact with the PFM tip's apex is responsible for nucleation of domains with opposite polarization. The large field enhancement observed at the edges of the disk representing the AFM tip can be discarded as a geometric artifact of the model as real AFM tips lack sharp edges (Figure 6.18 a,b). From the FEM results, it is clear that for the same applied voltage, the resulting electric field underneath the tip's apex in the PZT films (79 kV/mm) is approximately 10 times larger than in the PZT nanotubes (7.8 kV/mm). This is in excellent agreement with the experimental SS-PFM results that show an order of magnitude increase in the required switching voltage for the PZT nanotubes compared to the PZT films (20 V and 2 V, respectively).

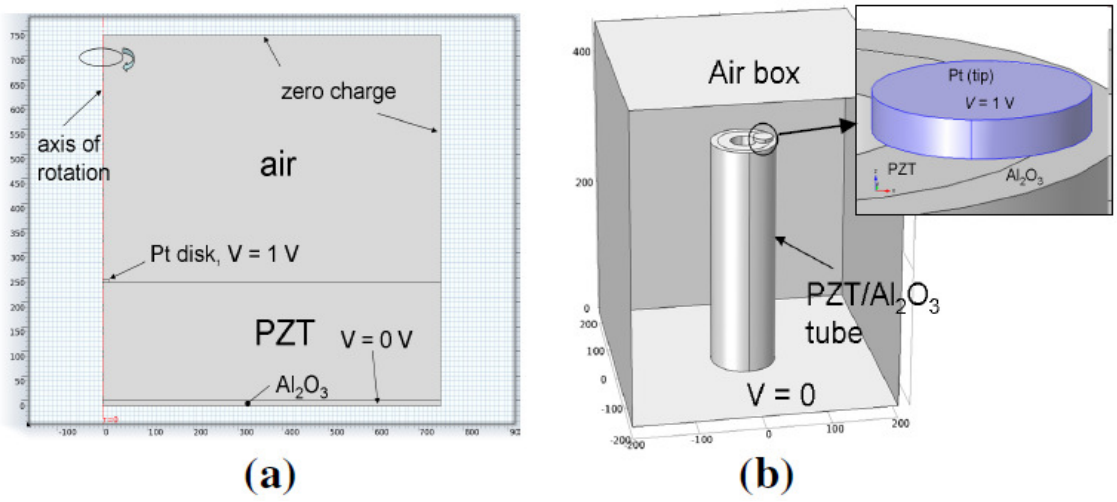

Figure 6.16: Finite element modeling (Comsol®) layouts for calculations of the electric field distributions in (a) 250 nm PZT / 10 nm Al_2O_3 bilayer film on platinized Si substrate and (b) ~250 nm high PZT/Al_2O_3 nanotube (20nm-thick PZT, 10 nm-thick Al_2O_3). The model in (a) is axi-symmetric two-dimensional. Units of length are in nm.

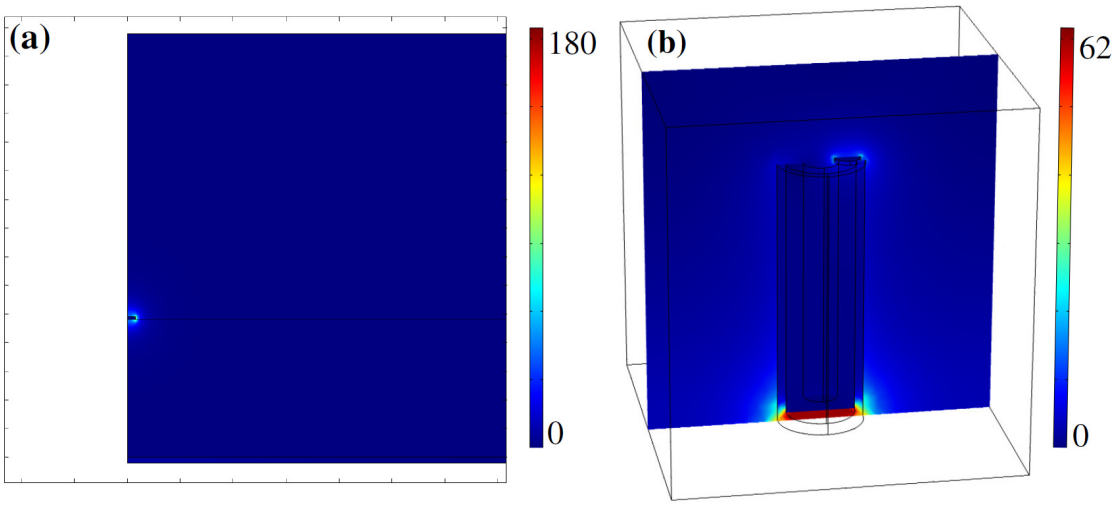

Figure 6.17: Electric field distribution for 1 V applied in (a) ~250 nm PZT/ 10 nm Al_2O_3 bilayer film on platinized Si substrate via an axi-symmetric two dimension FEM model with the AFM tip located at left edge and (b) ~250 nm high PZT/Al_2O_3 nanotube (20 nm-thick PZT, 10 nm-thick Al_2O_3) with the AFM tip located at the top right corner of the tube (scales in kV/mm).

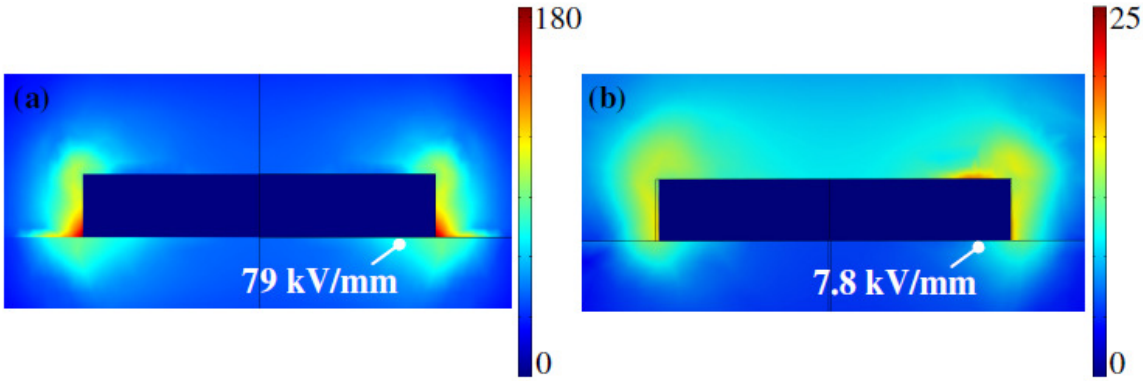

Figure 6.18: Localized view of the electric field distribution directly below the AFM tip in (a) ~250 nm PZT/ 10 nm Al_2O_3 bilayer film on platinized Si substrate and (b) ~250 nm high PZT/Al_2O_3 nanotube (20 nm-thick PZT, 10 nm-thick Al_2O_3) (scales in kV/mm).

6.9 Nonlinear Measurements

In order to compare the $d_{33,f}$ in the sub-switching regime for on- and off-tube locations, the maximum strain-amplitude is determined as a function of AC voltage amplitude (Figure 6.19a,b) and fitted via a quadratic equation (Equation 6.2). The increase in strain-amplitude response for the off-tube locations implies that a small amount of residual PZT remains on the top of the Al_2O_3 layer between adjacent tube tops.

$$A_{\max} = a_1 + a_2 V_{ac} + a_3 V_{ac}^2 \qquad \text{Equation 6.2}$$

The instantaneous slope of the strain response versus voltage (i.e. differentiation of Equation 6.2 with respect to AC voltage) corresponds to $d_{33,f}$. It is important to note that the maximum strain response recorded via the photodiode depends on the cantilever sensitivity (Equation 6.3)[31]. Thus, the measured $d_{33,f}$ coefficient depends on the probing cantilever used and its condition (i.e. sharpness); however, the cantilever's sensitivity is expected to remain relatively constant throughout a scan, therefore allowing a comparison of $d_{33,f}$ for the on-tube and off-tube locations.

$$\frac{A_{\max}}{V_{ac}} = a_2 + 2a_3 V_{ac} = \beta d_{33,f} \qquad \text{Equation 6.3}$$

The average $\beta\, d_{33,f}$ for the on-tube location was more than 3 times greater than the average of the off-tube location. To determine the relative amounts of intrinsic and extrinsic contributions to the piezoelectric response, differentiation of the quadratic equations can further be analyzed using the Rayleigh law (Equation 6.4).

[31] $a_1 \approx 0$

$$\beta d_{33,f} = \beta' d_{33,init} + \beta' \alpha E_{field} \qquad \text{Equation 6.4}$$

$d_{33,init}$ is the piezoelectric activity extrapolated to zero field and α is a measure of the level of extrinsic contribution. The intrinsic contribution for the on-tube location was more than 5 times the amount measured for the off-tube location (Figure 6.19c). The intrinsic response is the response that would be obtained in a single domain, single crystal ferroelectric. Thus, the increased intrinsic contribution for the on-tube location is attributed to an increased volume of PZT material beneath the probing tip compared to the off-tube location. The extrinsic piezoelectric contributions for the off-tube locations showed an increase in the extrinsic contribution compared to the on-tube location. The extrinsic contribution is related to domain polarization mechanisms such as domain wall motion.

The off-tube locations are comprised of the suspended alumina film and residual PZT on the surface. The small thickness in the off-tube region (~10 nm of suspended Al_2O_3 and at most ~20 nm of residual PZT) compared to the on-tube location (~350 nm tube height) results in an increased electric field in this region[32] with the same probing voltage applied. The higher electric field results in enhanced irreversible domain wall motion in the surface/residual PZT: with the effectively higher electric fields seen in the off-tube location the potential energy barriers for domain wall motion are more easily overcome leading to irreversible, rather than reversible, domain wall motion.

[32] Assuming a uniform field distribution, the electric field between electrodes is approximately equal to the voltage applied divided by the material's thickness (i.e. the separation distance between electrodes).

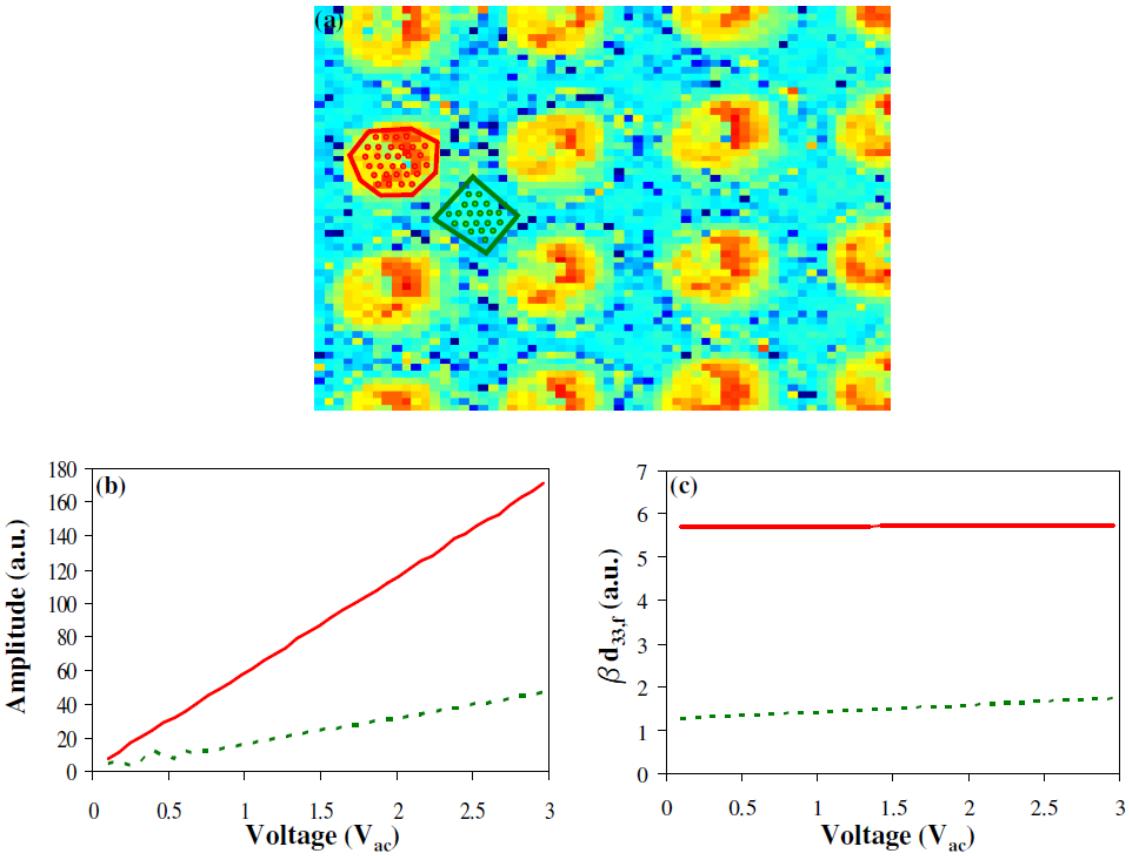

Figure 6.19: (a) Strain-amplitude spatially with 3 V_{ac} applied. (b) Average nonlinear strain-amplitude response and (c) convoluted $d_{33,f}$ response for on-tube (solid red) and off-tube (dashed green) locations.

6.10 Calibration of the $d_{33,f}$ Response

To calibrate the output response of the PFM tool, the $d_{33,f}$ response of a quartz sample was measured by a double-beam laser interferometer and compared to the PFM PRS amplitude. The sensitivity of the PFM detector can then be determined via Equation 6.5.

$$\beta = \frac{h_w}{d_{33} A_w} \qquad \text{Equation 6.5}$$

In Equation 6.5, β is the sensitivity of the photodiode, h_w is the amplitude of the PRS, and A_w is the amplitude of the probing voltage.

For the quartz sample, the double-beam interferometer measured $d_{33,f}$ was ~3 pm/V and the strain amplitude response[33] recorded by BE-PFM was ~2.3×10^{-5} (Figure A.1). Thus, the calculated sensitivity for the Cypher™ Atomic Force Microscope (Asylum Research) and AC240TM cantilever (Olympus) was ~0.0767 V/nm.

The maximum strain amplitude response of the PZT nanotubes was determined via SS-PFM measurements. Due to tool limitations, an arbitrary offset in the PFM response is often observed. Therefore, the strain amplitude vs. voltage (i.e. butterfly loops) are mathematically repositioned such that the minimum response recorded corresponds to zero. The maximum saturation response after repositioning was ~1.6×10^{-4} (Figure A.2). Thus, the calculated $d_{33,f}$ response for a single-infiltration PZT nanotube was ~210 pm/V, which is greater than the macroscopic $d_{33,f}$ reported for PZT thin films of similar thickness to the nanotubes' height (Table 6.2). However, it has to be noted that contact mechanics of the tip-surface junction have a vital role in the measured response. Differences in quartz sample (film) and PZT nanotubes due to geometric and mechanical disparities can alter the sensitivity factors for the two samples. For instance, roughness in the contact area between the sample surface and AFM tip can give origin to stray capacitors and/or additional electrical losses. Similarly, the AFM cantilever's interaction with sample surfaces of differing hardness can lead to different amounts of mechanical loss. Specifically, changes in the contact resonance frequency can alter cantilever dynamics and lead to large variations in sensitivity due to material or geometry variations,

[33] The strain amplitude response is the PRS divided by the AC probing voltage applied.

and hence invalidate the calibration. The above factors can in part justify the very high measured piezoelectric response in the PZT nanotubes.

Table 6.2: Measured $d_{33,f}$ for PZT thin films of various thicknesses

Composition	Deposition Method	Measurement Method	Thickness	$d_{33,f}$ (pm/V)
$PbZr_{0.52}Ti_{0.48}O_3$	Sol-gel	Double beam laser interferometer	2.8 μm	61 [130]
$PbZr_{0.52}Ti_{0.48}O_3$	Sputter deposition and released from substrate	Optical vibrometer	2 μm	300 [131]
$PbZr_{0.52}Ti_{0.48}O_3$	Sol-gel	Pneumatic pressure charge technique[34]	1.5 μm	105 [132]
$PbZr_{0.50}Ti_{0.50}O_3$	Sol-gel	Piezoelectric Force Microscopy	720 nm	68 [133]
$PbZr_{0.53}Ti_{0.47}O_3$	Sol-gel	Double beam laser interferometer	40 nm	20 [134]

6.11 Relaxation

The dynamic behavior of the PZT nanotubes was probed via D-SS-PFM (see section 3.13.4). The delay-time dependent amplitude, resonance frequency, and Q-factor after bias voltage application were determined by fitting the response in the frequency domain to a simple harmonic oscillator model (see section 3.13.2). The relaxation dynamics of the PRS after each bias pulse is shown in Figure 6.20. The internal bias of

[34] In the pneumatic pressure charge technique, a static stress is applied perpendicular to the film, and the surface induced charge is measured.

the PZT nanotubes was demonstrated by the ease of switching the PRS amplitude for negative excitation biases compared to positive biases.

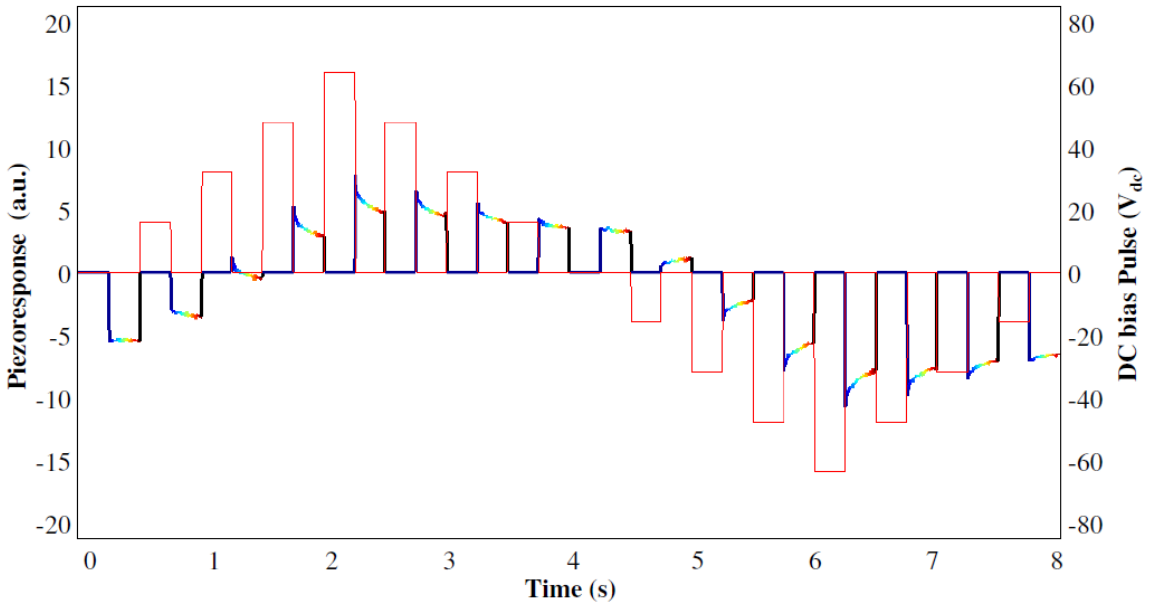

Figure 6.20: D-SS-PFM tip bias waveform (red) with time dependence piezoresponse (shading corresponds to delay time after pulse).

In order to provide a better insight into the relaxation dynamics, the response is fitted to a phenomenological model (Equation 6.6).

$$A_r(t) = A_{r0} + A_{r1} f(t) \qquad \text{Equation 6.6}$$

In Equation 6.6, A_{r0} is the offset, A_{r1} is the relaxation magnitude, and $f(t)$ is the relaxation function. Specifically, an exponential phenomenological model ($f(t) = \exp(-t/\tau_d)$) was chosen because it satisfies both boundary conditions $f(0) = 1$

and $f(t) = 0$ for $t \to \infty$. Furthermore, an exponential decay provides a better description of observed phenomena than, for instance, a power law model, in which the uncertainty of the data exceeded the model's uncertainty [119]. The hysteretic behavior as a function of delay time is shown in Figure 6.21a, and the fit parameters are shown in Figure 6.21b-d.

The offset (non-relaxing) parameter in the model (A_{r0}) forms a distinct hysteresis loop whereas the relaxation amplitude (A_{r1}) does not show any hysteresis. The relaxation time (τ_d) is independent of the bias voltage applied, thus suggesting homogeneity of the relaxation mechanism. The exact mechanism of this rapid relaxation is still not well understood. One study suggests that the observed response is due to either charge injection by the tip, local relaxor-like dynamics, or tip-induced polarization rotation; however, further investigation is still required [119].

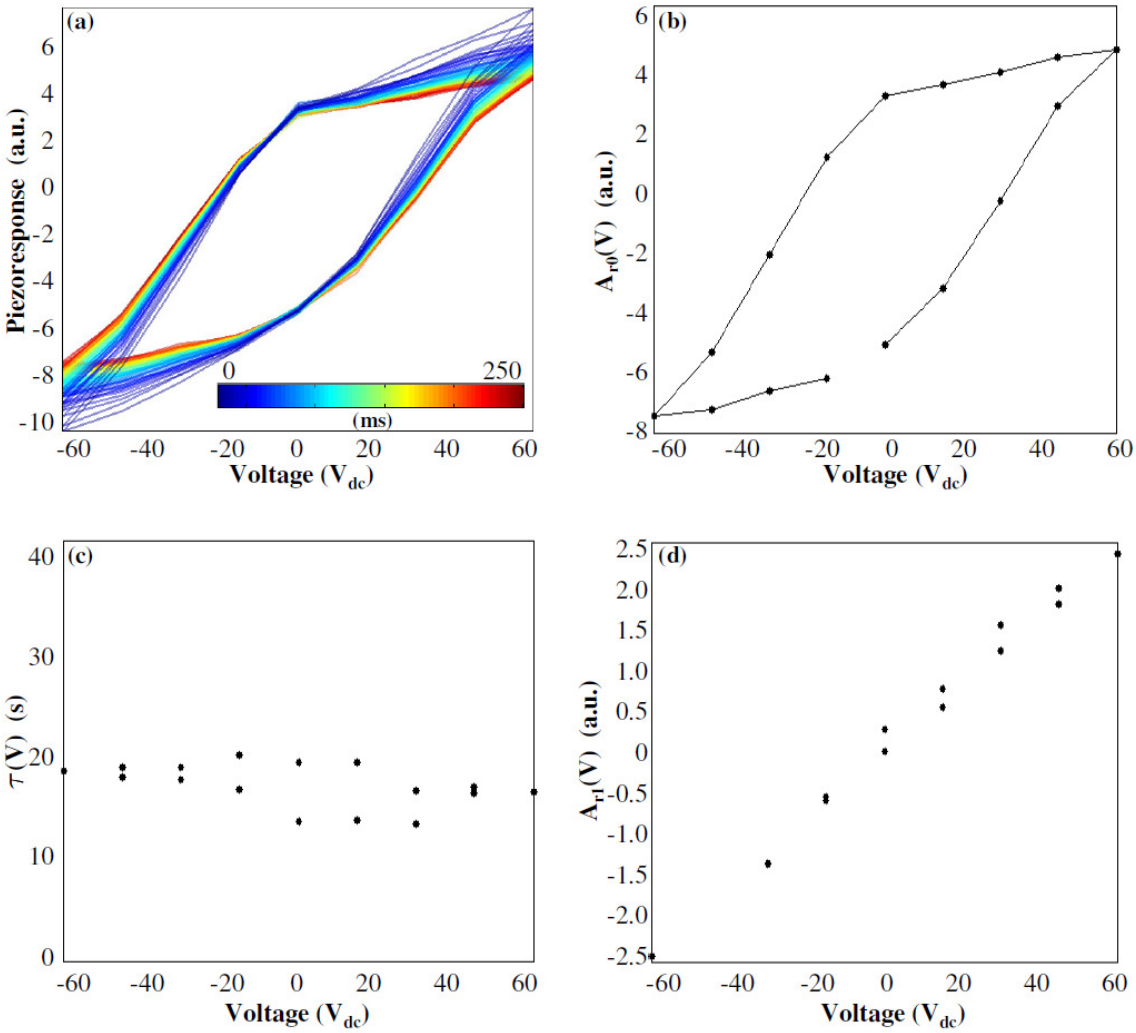

Figure 6.21: (a) D-SS-PFM piezoresponse loops for PZT nanotubes as a function of delay time and bias voltage applied. Phenomenological relaxation parameters showing the bias dependence of (b) A_{r0} (c) τ, and (d) A_{r1}.

CHAPTER 7

NANOSCALE PHENOMENA

This chapter is dedicated to the investigation of extrinsic contribution to the piezoelectric response in PZT nanotubes. Extrinsic contributions in ferroelectric materials mainly originate from vibration and displacement of domain walls, which give rise to field dependent dielectric and piezoelectric coefficients (nonlinearity) and hysteresis. Understanding such phenomena is vital from an applications point of view for optimum device performance, especially as the reduced device size translates into higher electric fields. Thus, factors effecting domain wall motion such as substrate clamping, critical size, and lateral constraint are studied in detail.

7.1 Experimental Procedure

In the following sections of this chapter, the piezoelectric response is compared for PZT nanotubes with different aspect ratios, wall thicknesses, and boundary conditions via SS-PFM and nonlinear piezoresponse measurements. To collect SS-PFM data for each PZT nanotube studied, a minimum of 25 hysteresis loops were collected, averaged, and mathematically centered[35]. For nonlinear measurements, the maximum AC voltage amplitude applied was 9.5 V_{ac}, which is less than half the coercive voltage. At voltages higher than ~0.5 V_C, nucleations of new domains are often observed. Hence any measurements at higher voltages would see a convolution of extrinsic contributions from

[35] Mathematical centering is required due to the tool's arbitrary offset.

domain wall mobility and increased domain wall density [128]. To quantify extrinsic contributions to the piezoelectric response, the nonlinear piezoresponse (measured by BE-PFM) was analyzed using the Rayleigh law (see section 6.9 for converting the strain-amplitude response into piezoelectric coefficient, $d_{33,f}$). For piezoresponse measurements through BE-PFM, the Rayleigh parameters are convoluted with the photodiode's and cantilever's sensitivities (see Equation 6.4). However, the ratio of the irreversible to reversible piezoelectric Rayleigh coefficients (considered as a measure of the extrinsic contributions to the piezoelectric properties under the assumption that the reversible extrinsic contributions are limited with respect to intrinsic contributions) is remarkably independent of the photodiode's and cantilever's sensitivities, thereby allowing local nonlinearity to be measured quantitatively.

7.2 The Effect of Substrate Clamping on the Piezoelectric Response

"Clamping" describes the constraint of a piezoelectrically-active material to a non-active material such as the substrate, inhibiting deformation (i.e. reducing the overall piezoelectric response). Substrate clamping is usually distinguished from lateral constraint, as the former affects mostly the longitudinal piezoelectric response, whereas the latter modifies the lateral/radial response of a piezoelectric material, mostly in a symmetric fashion. Difficulties in studying substrate-clamping effects arise due to lack of available processing techniques for patterning piezoelectric materials with defined aspect ratios, which would provide the means for alteration of the volume percent of

material clamped to the substrate. Thus far, nanoscale manufacturing of ferroelectrics has mostly leveraged focused ion beam (FIB) milling, which can induce surface damage. In Pb-based ferroelectrics, this damage cannot be overcome by high temperature heat treatments as studies have shown the presence of an amorphous layer even after annealing, which degrades the ferroelectric and piezoelectric response [72]. Additionally, while high aspect-ratio nanoscale ferroelectrics have been previously processed in hard templates, there has been no control over the lateral size or the overall aspect ratio of the nanotubes obtained [57, 95]. The development of the soft-template infiltration technique enables alteration of the aspect ratio of the PZT nanotubes, without inducing surface damage, thus providing the means for studying the effect of substrate-clamping on the final piezoelectric properties of ferroelectric nanostructures.

To vary the aspect ratio of the PZT nanotubes, the thickness of the resist (which ultimately determines the height of the PZT nanotube) was varied by adjusting the spin coating conditions, while the PZT wall thickness and diameter were held constant at ~20 nm and ~100 nm, respectively.

Figure 7.1a shows the piezoresponse hysteresis loops for PZT nanotubes with aspect ratios ranging from 2.5:1 to 5:1. PZT nanotubes with lower aspect ratio did not show a clear polarization switching and therefore were excluded from this analysis. The electric field rather than voltage was used in this analysis as the effective response is field rather than voltage dependent. The electric field generated in the PZT nanotubes via the application of the external voltage through the AFM tip was estimated based on results from finite element modeling (see section 6.8).

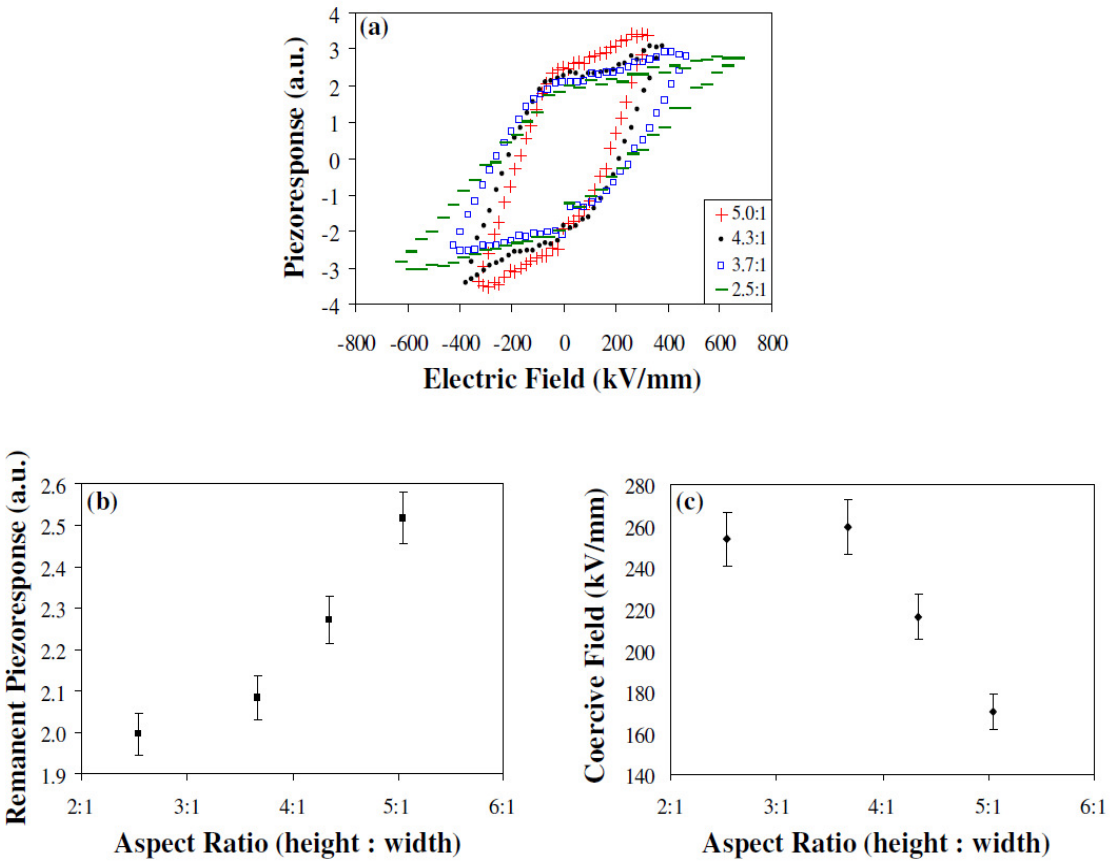

Figure 7.1: (a) SS-PFM piezoresponse-electric field hysteresis loops and (b) the extracted remanent piezoresponse and (c) coercive field for PZT nanotubes with aspect ratios ranging from 2.5:1 to 5:1.

As the aspect ratio of the PZT nanotubes increased, the remanent piezoresponse increased (Figure 7.1b) and the coercive field decreased (Figure 7.1c). The remanent piezoresponse is the response after removal of the electric field and is an index of the ability to pole the ferroelectric material (i.e. reorient domains in a direction close or parallel to the applied electric field) [6]. The coercive field (E_c) is the electric field required to switch the overall (macroscopic) polarization of the material.

The reduction in the remanent piezoresponse at decreasing PZT nanotubes' aspect ratio is a possible effect of a larger percentage of the overall volume of material clamped

to the substrate. The clamping of domains to the substrate has been previously observed for ferroelectric thin films with large residual stress. Biaxial, tensile residual stresses are often present in ferroelectric thin films on platinized substrates due to differences in the coefficient of thermal expansion of the ferroelectric and underlying substrate, as well as ferroelectric distortion at the Curie temperature [135]. Due to the tensile nature of the residual stresses in the PZT in proximity of the platinized substrate, it is expected that a large volume of the PZT in the same locations would adopt a polarization direction with a large in-plane component (Figure 7.2a). It is plausible that even with the application of high electric fields, such as those supplied during SS-PFM measurements, the domains with a large the spontaneous polarization component parallel to the substrate will remain "pinned to the substrate", without switching to a more "vertically" aligned polarization, i.e. with a larger component parallel to the direction of the applied electric field (Figure 7.2b). Thus, this lack of alignment in the volume of material in close proximity of the substrate will effectively behave as "clamped to the substrate", leading to an overall lowered polarization, as well as a reduced remanent and saturation piezoresponse. As the aspect ratio in the ferroelectric nanostructures increases, there is a larger volume of material that is (at least partially) unclamped from the substrate and therefore can be partially deformed, i.e. undergoes ferroelastic domain wall switching via an appropriately high applied electric field.

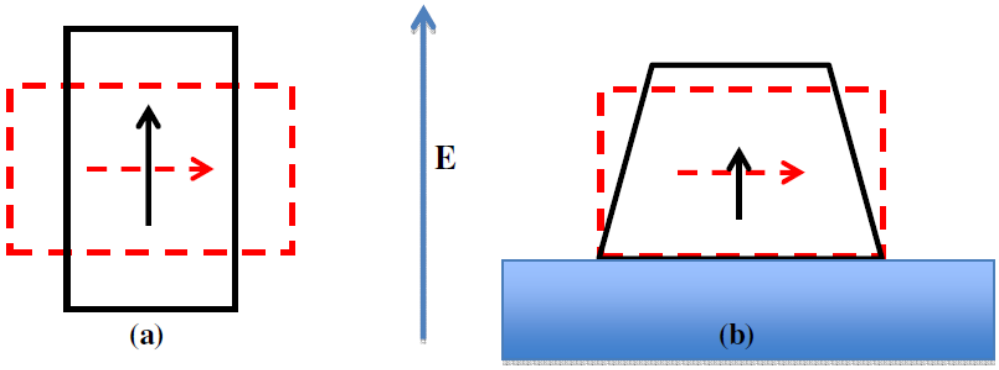

Figure 7.2: Schematic illustration of (a) an unconstrained domain with in-plane polarization switching to out-of-plane polarization under applied electric field; (b) a constrained domain clamped to the underlying substrate due to residual stress, showing minimal out of plane deformation under the same applied electric field. Red, dashed curves represent the domain before application of the external electric field and the black, bold lines the structures under applied electric field.

Difficulty in switching domains with large in-plane spontaneous polarization components has been previously reported in PZT thin films. In a study performed on a 400 nm-thick, epitaxially grown $PbZr_{0.2}Ti_{0.8}O_3$ film, the application of +10 and -10 V_{dc} bias via an AFM tip did not alter the number and position of *a*-domains while *c*-domain exhibited 180° switching [136]. The *a*-domains are domains with in-plane spontaneous polarizations, while *c*-domains show polarization direction normal to the substrate (see Figure 2.25).

This same mechanism, i.e. substrate clamping, could also be responsible for the decrease in the coercive field with increasing nanostructures' aspect ratio. As previously discussed, the coercive field (E_c) is the electric field required to switch the polarization of the material. The polarization reversal in a ferroelectric material is a gradual process, in which the unit cells within a domain do not all switch simultaneously. During SS-PFM

measurements, the switching process typically begins with nucleation of one or more new domains beneath the AFM tip, with a well-aligned polarization direction with respect to the applied electric field. The nucleation event is then followed by growth (i.e. domain wall motion to increase the domain's volume). The growth of nucleated domains normally proceeds via a faster elongation in the direction of the applied electric field and a much slower expansion in the transverse direction [137]. The continued growth of nucleated domains beneath the AFM tip eventually results in overall polarization reversal of the material. Clearly, any process that inhibits domain wall motion (i.e. prevents growth) affects the coercive field.

As shown in Figure 7.1b, the coercive field is relatively invariable for PZT nanotubes with aspect ratios below 4:1. For aspect ratios greater than 4:1, the coercive field decreases substantially. The decrease in the coercive field with increasing aspect ratio is possibly due to a reduction in the overall volume percentage of material clamped to the substrate. Clamped material act as pinning sites that inhibit domain wall motion and can prevent the growth of nucleated domains. In thin films, previous studies have shown the existence of a stress field that reduces in amplitude with distance from the underlying substrate [138]. This stress field ultimately alters the effective pinning strength in the material. Low aspect ratio structures have a larger average stress concentration than high aspect ratio structures. Thus, to switch the overall polarization direction in low aspect ratio structures, an increased amount of energy is required, leading to an increase in the coercive field as the aspect ratio decreases.

Previous literature reports of PZT films patterned via FIB [100-101] have not observed any clear trend in the coercive field with changing the ferroelectric structure's

aspect ratio. These inconclusive results for the coercive field could possibly be due to the inability to control the amount of gallium contamination introduced during FIB milling, as well as a constant volume percentage of materials rendered amorphous at the surface due to the interaction with the high energy particles. Surface defects (Ga inclusions or amorphous regions of material) can affect the ability of domains to nucleate and grow, thus altering the coercive field.

In a very different and original approach, McLachlan et al. also have studied the effect of substrate clamping by measuring the piezoresponse for a continuous films and a macroporous PZT structure, fabricated via coating an ordered array of polystyrene spheres with PZT sol (Figure 7.3a,b). The continuous PZT films exhibited a reduced remanent piezoresponse and an increased coercive field compared to the PZT walls of macroporous arrays (Figure 7.3c) [139]. The small piezoresponse and large coercive values for the continuous film were attributed to clamping while the square-shaped loops of the macroporous PZT was indicative of strain-free ferroelectric structures. These results are in agreement with those herein reported for the PZT nanotubes: low aspect ratio structures showed a reduced remanent and saturation piezoresponse and an increased coercive field compared to high aspect ratio structures.

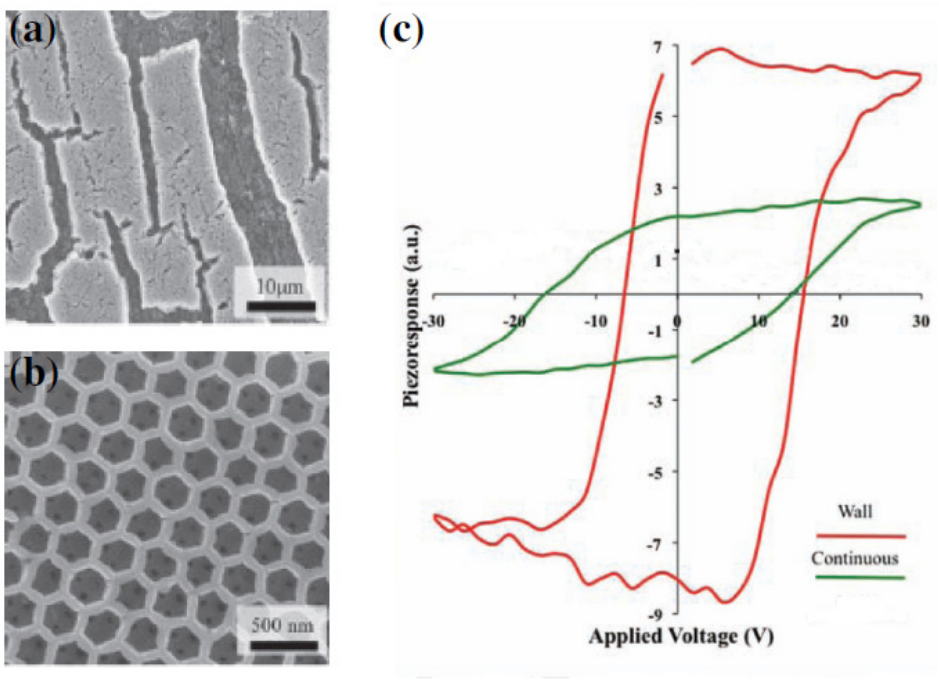

Figure 7.3: SEM images of the macroporous PZT array: (a) large view and (b) higher detailed view of the hexagonal wall structure. (c) Piezoresponse hysteresis loops obtained from a continuous PZT film (green) and wall of macroporous PZT (red). [139]

To further investigate the origin of the increase in the remanent piezoresponse and the decrease in coercive field, nonlinear measurements were performed and analyzed using the Rayleigh law. To verify that the extrinsic contribution is strongly dependent on the aspect ratio of the tube and not simply the height of the tube, nanotubes with the same heights but with 200 nm-outer dimension were fabricated, yielding aspect ratios ranging from 1.25:1 to 2.5:1. The outer diameter of the tubes was altered by changing the lateral dimension in the resist during electron beam patterning. Figure 7.4 shows SEM images of the two extreme aspect ratios studied in this research, 1.25:1 and 5:1.

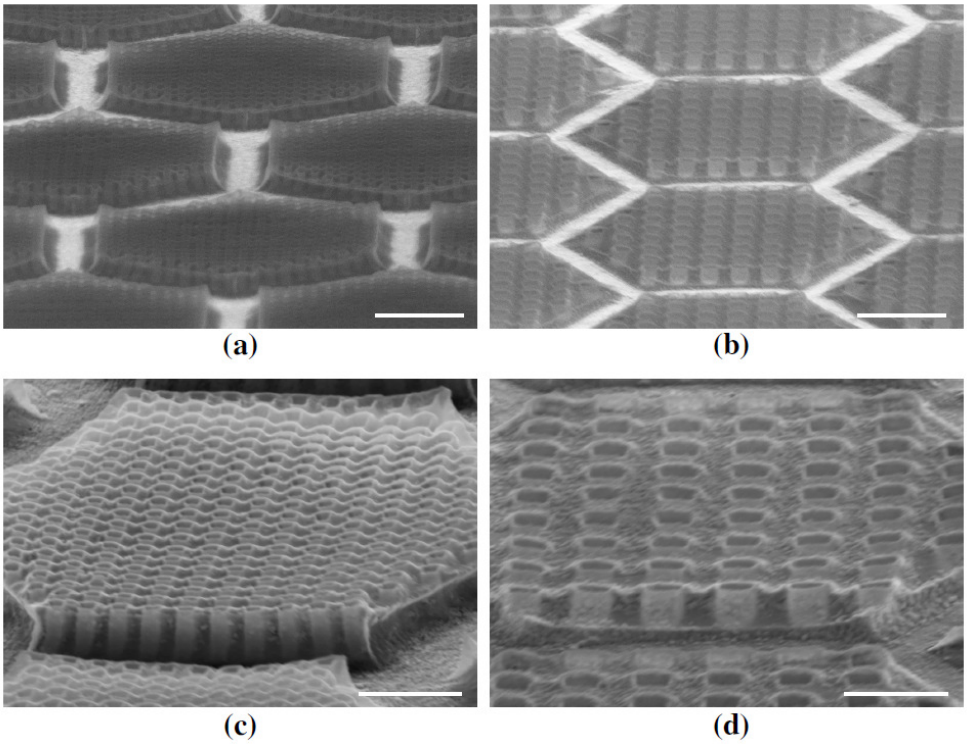

Figure 7.4: SEM images of PZT nanotube arrays: (a) and (c) 100 nm-outer diameter with aspect ratio of 5:1; (b) and (d) 200 nm-outer diameter with aspect ratio of 1.5:1 (top: 1 μm scale bars; bottom: 500 nm scale bars).

Figure 7.5 shows the piezoelectric Rayleigh parameters' ratio, α/d_{init}, as a function of PZT nanotubes' aspect ratio. For nanotube aspect ratios below 3:1, the α/d_{init} ratio was close to null, which indicates negligible extrinsic contributions to the piezoresponse in these samples. This observation is consistent with the inability to switch the piezoresponse (and therefore the polarization) in low aspect ratio PZT nanotubes (<2.5:1) via SS-PFM measurements. As the aspect ratio of the tube increased from 3:1 to 5:1, the Rayleigh parameters' ratio increased, thus identifying a significant enhancement of extrinsic contributions, possibly through ferroelastic, non-180^o domain wall motion due to a reduction in the percentage (i.e. average strength) of material clamped to the

substrate. It is important to note, that the 200 nm diameter tubes with similar heights as the 100 nm diameter tubes, showed a similar trend with reduced extrinsic contribution for aspect ratios below 3:1. This indicates that the height of the nanotube doesn't solely determine the piezoelectric response but rather its aspect ratio. Theoretical calculations have also shown that strain relaxation in epitaxially $PbTiO_3$ patterned films' dependence on the scaling ratio and not only the lateral dimension (i.e. film thickness). As the scaling ratio decreased (width: height), the in-plane strain drop drastically according to finite element simulations [99].

It is interesting to note that the Rayleigh parameters for the PZT nanotubes did not show any saturation within the studied aspect ratio range. It is expected that α will eventually saturate when a threshold aspect ratio is reach, beyond which the substrate-clamping effects have negligible influence on the material's response. It is also noteworthy that d_{init} was relatively invariant (less than 0.5% variation) for PZT nanotubes with aspect ratio > 3:1. This is a clear indication that the d_{init} is mostly due to the intrinsic response of the ferroelectric rather than the (reversible) extrinsic contributions. It also further underlines the fact the continuous increase observed in the Rayleigh parameters' ratio is indeed a direct effect of the reduction of substrate-clamping on the overall behavior of the material. Further studies are required to determine the threshold aspect ratio beyond which PZT nanostructures on platinized Si substrates will behave as effectively free-standing (see 8.2.3).[36]

[36] It is important to note that this future (yet to be demonstrated) threshold aspect ratio is expected to be dependent on PZT nanotube's wall thickness.

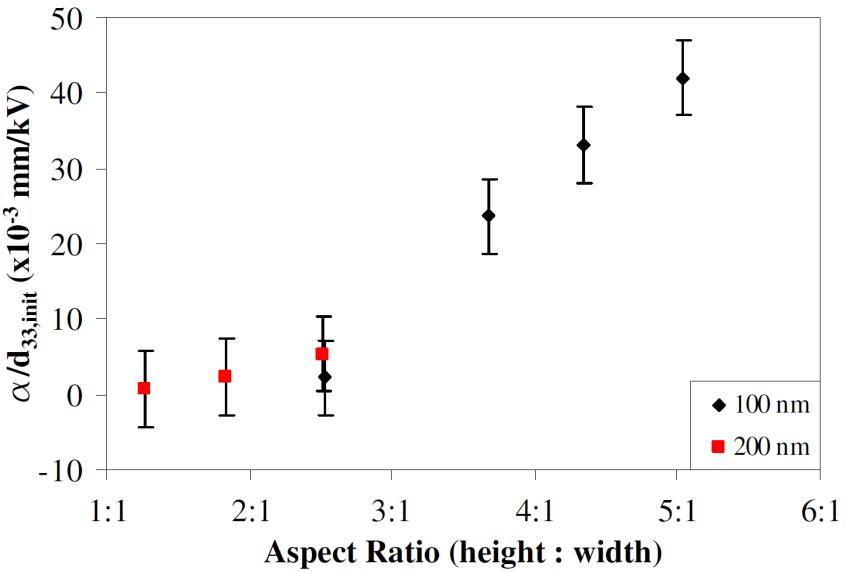

Figure 7.5: Irreversible to reversible Rayleigh parameters' ratio as a function of aspect ratio for 100 nm (black diamond) and 200 nm (red square) outer diameter PZT nanotubes.

7.3 The Extrinsic Contribution as a Function of Tube Wall Thickness

The electromechanical response in ferroelectrics is strongly dependent on physical size (i.e. volume of material). The sources of size effects in ferroelectrics are both intrinsic and extrinsic in nature. Intrinsic size effects describe the critical thickness below which ferroelectricity vanishes, i.e. the material shows paraelectric behavior. Intrinsic size effects have been extensively studied via theoretical and experimental approaches in ceramic and single crystalline samples [106, 140-143]. Conversely, extrinsic size effects describe the reduction in electromechanical response due to energetic limitations in creation or motion of internal interfaces such as domain walls and eventual phase boundaries. Specifically, the ferroelastic, non-180^{o} domain walls, are one of the major contributors to the extrinsic piezoelectric response in ferroelectric materials.

Extrinsic size effects have been much less studied and mostly limited to thin films clamped to the underlying substrate [98], which inherently reduces the mobility of non-180^{o} domain walls. The use of soft-templates to fabricate PZT nanotubes eliminates mostly the (substrate and lateral) clamping effects and provides the means to study extrinsic size effects with minimal residual stress.

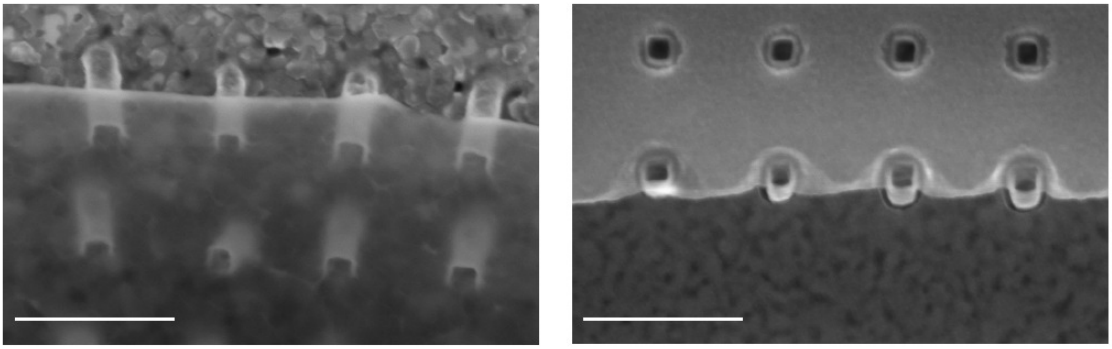

Figure 7.6: (a) Single infiltration of soft-template with 0.2 M PZT solution; (b) two infiltrations of the soft-template with 0.2 M PZT solution (500 nm scale bars). Doubling the number of infiltrations leads to nanotube structures with slightly thicker walls and therefore decreasing electron-transparency.

To study the extrinsic size effects, SS-PFM piezoresponse was collected for PZT nanotubes with wall thickness ranging from 5 nm to 25 nm. The PZT wall thickness was varied by increasing the number of sol-gel infiltrations (Figure 7.6), while the overall aspect ratio of the structures was kept constant at 5:1. A high aspect ratio was chosen in order to minimize substrate clamping effects [1].

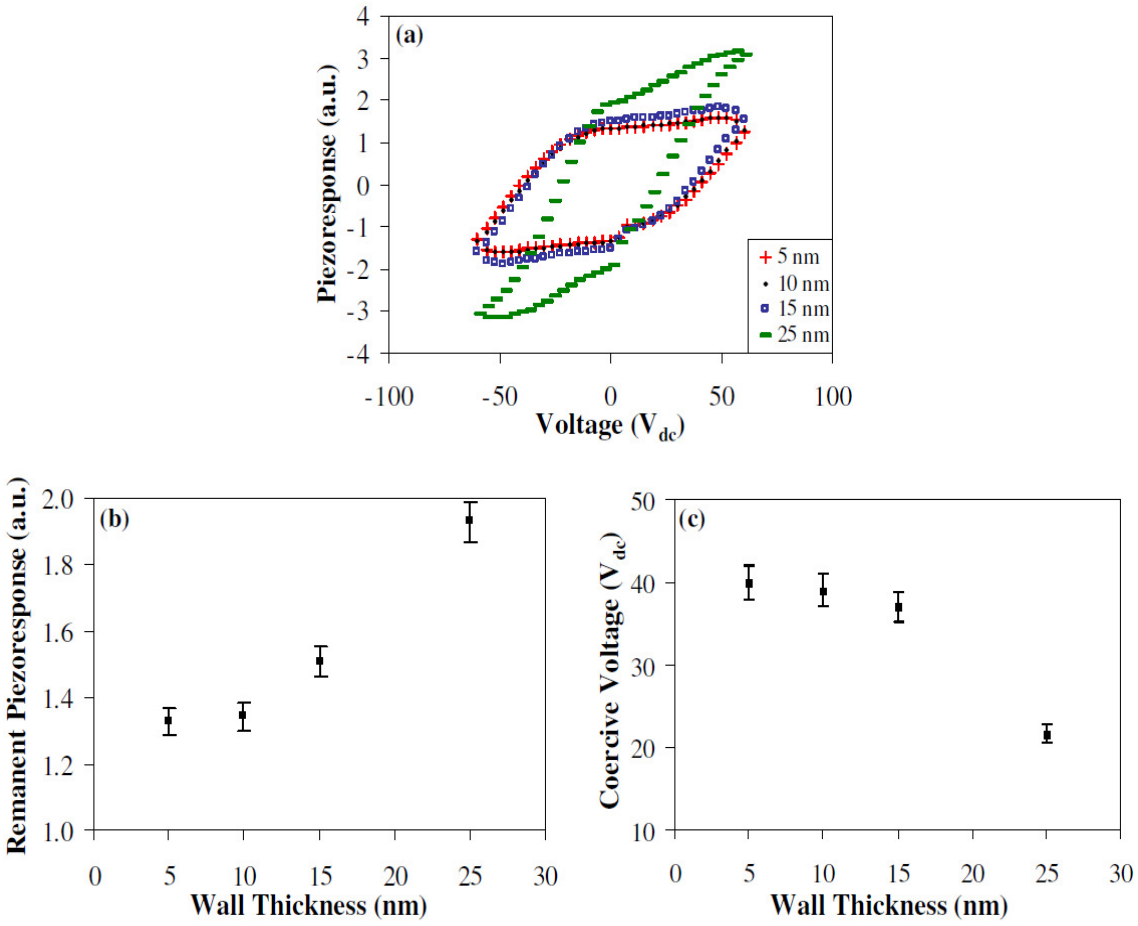

Figure 7.7: (a) SS-PFM piezoresponse-electric field hysteresis loops and (b) remanent piezoresponse and (c) coercive voltage for PZT nanotubes with 100 nm outer diameter, 5:1 aspect ratio, and PZT wall tube thicknesses ranging from 5 nm to 25 nm.

Figure 7.7a shows the piezoresponse as a function of tube thickness. As the PZT tube thickness increased, the remanent piezoresponse increased (Figure 7.7b) and the coercive voltage decreased (Figure 7.7b). The decrease in the remanent piezoresponse and increase in the coercive voltage with decreasing PZT tube thickness could possibly be due to changes in the electric field distribution underneath the AFM tip associated with the wall thickness variation. Thus, COMSOL Multiphysics® finite element models were used in order to simulate the electric field distribution for the two extreme cases (i.e.

wall thickness of 5 nm and 25 nm). In both models, the disk representing the AFM tip is place approximately in the center of the PZT wall thickness. Figure 7.8a shows the electric field distribution as a function of the distance from the top electrode (i.e. AFM tip). The thicker walled PZT nanotube is subject to a smaller electric field in the uppermost material volume in proximity of the AFM tip. For approximately 2/3 of the tube height from the bottom of the tubes, the electric field distribution in both nanotubes is similar. While in the Al_2O_3 layer in immediate contact with the Pt bottom electrode, the electric field is larger in the tubes with thicker walls.

A simplified equivalent circuit for the PZT nanotube is shown in Figure 7.8b. The structure functions as a capacitive voltage divider. As the PZT wall thickness increases, the capacitance associated with the PZT portion of the tube (C_{PZT}) increases and thus leads to a larger overall capacitance associated with the tube height (C_1). Therefore, the voltage drop and consequently the electric field across C_1 is smaller for thicker PZT tube walls. The electric field in the capacitance C_2, associated with the Al_2O_3 near the bottom electrode, also changes with the PZT thickness; however, the electric field in C_1 determines the piezoresponse. A smaller electric field for the same applied voltage means that a higher coercive voltage is required to switch the overall polarization of the material in the thicker PZT-walled samples. However, this result is inconsistent with the observed trend, which shows a reduction in the coercive voltage as the wall thickness increased. Thus, another mechanism that is affected by tubes' wall thickness must be responsible for the observed trend.

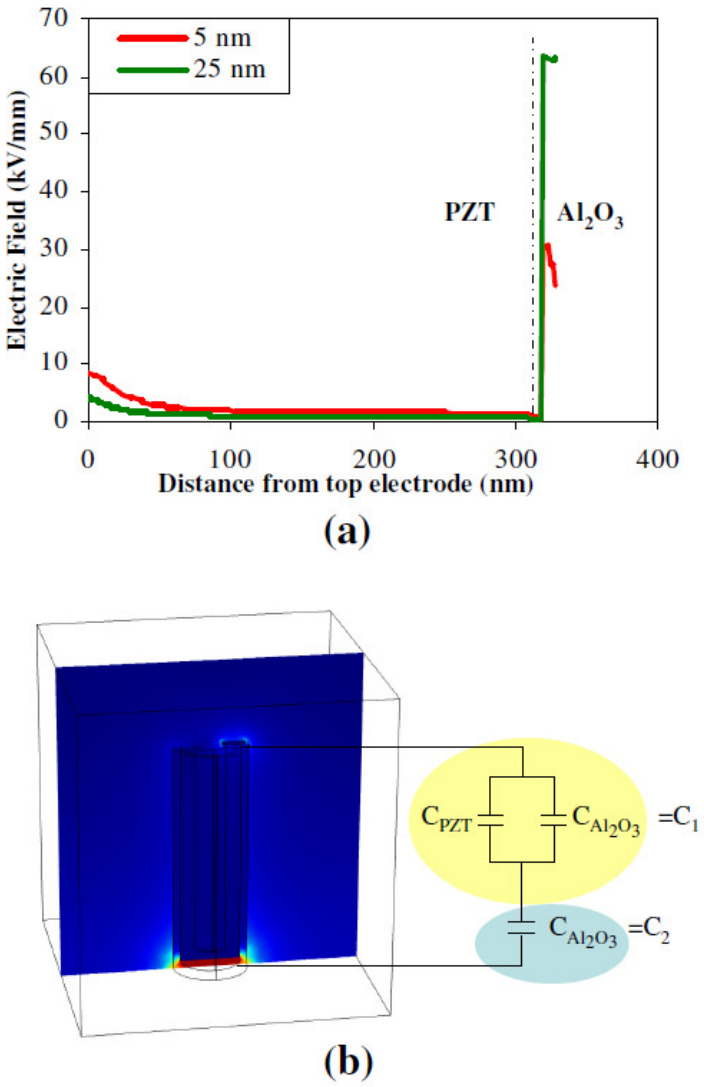

Figure 7.8: (a) Electric field distribution as a function of the distance from the top electrode for PZT nanotubes with 5 nm and 25 nm wall thickness, and (b) simplified equivalent circuit for the PZT nanotube.

With a reduction in the critical dimensions of the ferroelectric phase (i.e. wall thickness), progressively finer domain structures are expected until a critical ferroelectric thickness is reached, at ~10 nm (Figure 7.7b). At the extrinsic critical thickness, the overall energy of the system cannot be further reduced by creation of non-180° domain

walls, and therefore the formation of non-180° domains is no longer energetically favorable [2]. The extrinsic piezoresponse is mostly due to non-180° domain wall motion, thus the absence of non-180° domain walls leads to a large reduction of piezoresponse [144].

The continuous increase in the remanent piezoresponse at wall thicknesses greater than 10 nm is attributed in part to an increased grain size in the nanotubes. An increase in the grain size can contribute to piezoelectric response through extrinsic effects, as indeed both domain density and domain wall mobility are affected by grain size. As the size of the ferroic phase (i.e. grain size) increases, the concentration of grain boundary decreases. Grain boundaries act as pinning sites for internal interface motion. Therefore, a reduction in concentration of grain boundaries translates into an increase in domain wall mobility. Thus, grain growth can result in an increase in non-180° domain mobility, which ultimately leads to the increase in the remanent piezoresponse and saturation through extrinsic contributions.

The reduction in coercive field as the wall thickness decreased can also be explained by reduction, and ultimately absence of non-180^o domain walls' density at critical length scales. Although switching can occur via 180^o reorientation of polarization, more detailed studies (both experimental and theoretical) over the last decade have suggested that switching occurs by reorientations of dipoles through an intermediate non-180° "rotation" [145-146]. This mechanism of switching, rather than the direct 180^o, is believed to be more energetically favorable. If the formation of non-180° domain walls is unfavorable energetically at room temperature (without externally applied electric field but in presence of only thermal energy), it is also quite probable that

similarly under applied electric field, a larger amount of electrical energy is required for the onset of switching through intermediate non-180° polarization rotation. This implies that either a higher amount of energy is required for polarization switching events in nanotubes with thinner PZT walls, as the non-180° has a higher energy threshold or otherwise that the switching will need to happen through direct 180° rotation. Additionally, switching in the tubes whose critical dimension i.e. thickness is below the critical size must occur mostly via 180° reorientation, requiring higher energies and therefore higher coercive fields.

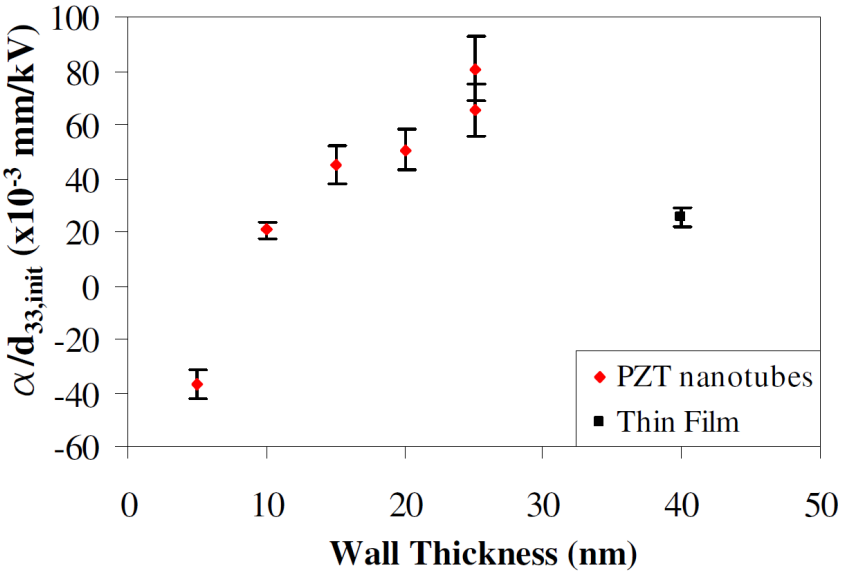

Figure 7.9: Rayleigh parameters' ratio as a function of wall thickness for PZT nanotubes and for a PZT thin film of similar thickness.

In order to quantify the extrinsic contributions to the piezoelectric response as a function of tube thickness, as well as verify the extrinsic origin of the observed behavior, nonlinear BE-PFM measurements were performed and analyzed using the Rayleigh law.

Figure 7.9 shows the ratio of the irreversible to reversible Rayleigh parameters as a function of wall thickness. For PZT wall thicknesses below 10 nm, the α/d_{init} ratio is close to null, which indicates negligible irreversible extrinsic contributions to the piezoelectric response in these samples.

Such critical thickness for ferroelectric materials have been previously studied theoretically and estimated at ~10 nm for $PbTiO_3$ [109]. Experimental observations in ferroelectric films have also highlighted the extrinsic ferroelectric critical size, although limited to much larger values: ~60 nm for $PbTiO_3$ thin films on (001) $LaAlO_3$ substrates [147], ~50 nm for $PbTiO_3$ thin films on (001) $SrTiO_3$ substrates [148], and ~60 nm for $Pb(Zr_{0.53}Ti_{0.47})O_3$ on platinized Si wafers [134]. However, the results from thin films are in part convoluted with the effects of lateral constraints due to inactive surrounding film, residual stresses formed at cooling from processing temperatures, grains size effects in polycrystalline films, and stress relaxation for single crystalline samples. The values observed in the free-standing PZT nanotubes are in excellent agreement with the theoretical studies, which indeed exclude residual stress effects and lateral constraints.

At increasing wall thickness (from 15 nm to 25 nm), the Rayleigh parameters' ratio increased, thus identifying a significant enhancement of domain wall motion contributing to the piezoelectric response. At 25 nm, the grain growth on-top of the PZT nanotubes (Figure 7.10a,b) alters the effective nanotube height and thus changes the electric field. Because of this grain growth, the assumed electric field was adjusted via a 20 nm increase in the height of the tube (approximate PZT grain size). Thus, Figure 7.9 shows two data points at 25 nm thickness (with and without this electric field adjustment).

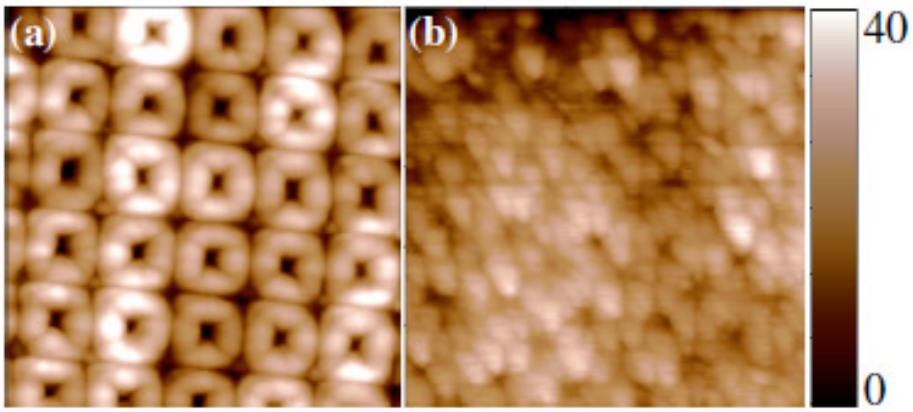

Figure 7.10: 1 μm x 1 μm AFM contact mode topography scan of PZT nanotubes with (a) 20 nm wall thickness and (b) 25 nm wall thickness where extensive grain growth on top of the nanotubes was observed (scale bar in nm).

For reference, the irreversible to reversible Rayleigh parameters' ratio was also determined for PZT thin films (see section 6.1 for deposition procedure) with similar thickness as the PZT nanotube walls (the minimum film thickness is limited by the maximum possible spin-coat speed and the molarity of the precursor solution). SS-PFM hysteresis loops and Rayleigh-like nonlinear behavior were observed only for PZT films with thicknesses greater than 40 nm (shown in Figure 7.9). The Rayleigh parameters' ratio is substantially larger for the PZT nanotubes than the PZT films, thus confirming a substantial increase in extrinsic piezoelectric response in PZT nanotubes due to reduction of lateral and substrate clamping effects on domain wall motion in the high aspect-ratio nanotubes.

7.4 The Effect of Lateral Constraint on the Piezoelectric Response

Non-180^{o} domain wall motion is not only affected by critical length scales and restricted by substrate clamping but can also be reduced by lateral constraints. In thin films, when measuring dielectric properties via locally deposited top electrodes, lateral clamping is present mostly through the interaction with the inactive volume of the film circling the active portion subject to external fields. To study the effect of lateral constraint for nanotubes, the piezoelectric response is compared for PZT nanotubes manufactured using the soft-template infiltration method with those created in a hard-template.

7.4.1 Hard-Template Preparation

A hard-template was fabricated by spin coating Flowable Oxide Resist 16® (FOX 16) followed by patterning using electron beam lithography. FOX 16 is based on a silicone resin and does not thermally decompose during the high temperature anneals required to crystallize PZT, unlike the soft-template comprised of ma-N 2403. The spin-speed curve for FOX 16 is shown in Figure 7.11. To fabricate tubes with height similar to tubes processed in the soft-template, the resist was deposited by spin coating at 5000 rpm for 1 min followed by a hotplate bake at 80^{o}C for 4 min to remove excess solvent, which resulted in a final template thickness of ~500 nm.

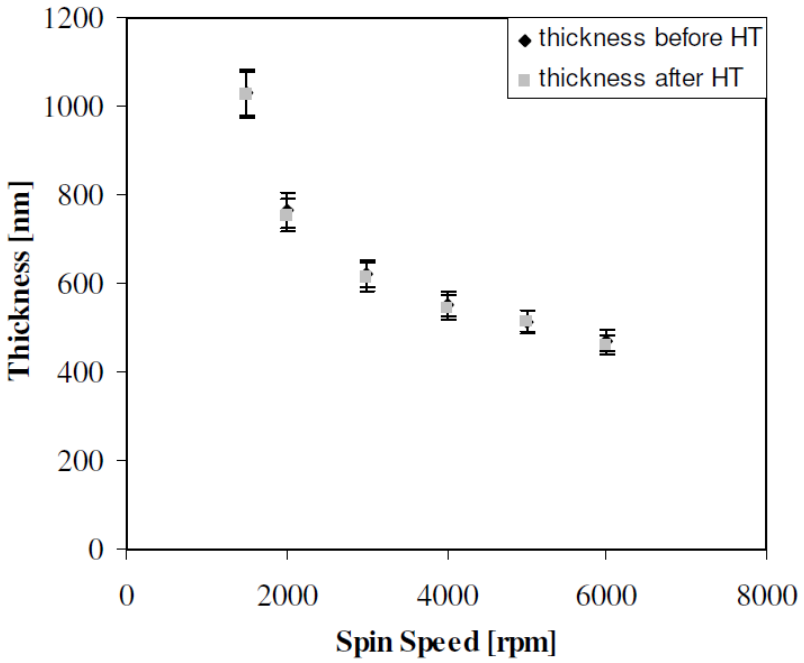

Figure 7.11: Resist thickness as a function of spin speed for FOX 16®, before and after heat treatment (HT) at 80°C for 4 min.

FOX 16 was e-beam exposed directly after spin coating, as previous studies have shown the resist's sensitivity to the time elapsed between coating and exposure [149]. An exposure dose of 2000 μC/cm^2 was used to fabricate 100 nm diameter holes with 400 nm pitch. After exposure, the resist was developed in 25% TMAH at 80^{o}C and rinsed with gently flowing DI water[37] for 30 sec.

The hard template then undergoes the exact same infiltration processing conditions (including ALD alumina coating) and heat treatments to create PZT nanotubes as in the soft-template processing. Creation of small amounts of secondary phases are also possible in the hard templates, however, the same amount of secondary phases

[37] Flowing water was used rather than stagnant DI water in order to reduce residue.

should form in both the soft-template and hard-template manufacturing approaches[38], allowing a comparison of the piezoresponse between the two systems.

7.4.2 Lateral Constraint Results

The high field piezoresponse of nanotubes processed in hard- and soft-templates are reported in Figure 7.14 and the characteristic values are summarized in Table 7.1. The piezoresponse was plotted as a function of electric field, based on finite element modeling (see section 6.8 for more information regarding the COMSOL model layouts).

The major difference in configuration for the soft- and hard-template-grown nanotubes is the replacement of the air-gap (ε_r=1) between adjacent tubes with FOX 16 (ε_r =3). This exchange in surrounding material is expected to affect the dielectric properties and electric field distribution, as well as the electromechanical properties of the nanotubes as FOX 16 has a finite mechanical stiffness. From the FEM results for the same applied voltage (1 V), the resulting electric field underneath the AFM tip for the PZT nanotube embedded in the hard-template (12.4 kV/mm) (Figure 7.12a,b) is significantly larger than for the PZT nanotube created in the soft-template (7.8 kV/mm) (Figure 7.12c,d). Therefore, the material surrounding the PZT nanotube has a crucial impact on electric field strength in the nanotube itself.

[38] It is important to note that no secondary phase was observed in the micro-Raman spectra for the PZT nanotubes or in XRD analysis for PZT thin films deposited on Al_2O_3 coated platinized wafers. However, crystallographic phases with less than 5% volumetric percentage or low crystallinity could remain undetected by XRD.

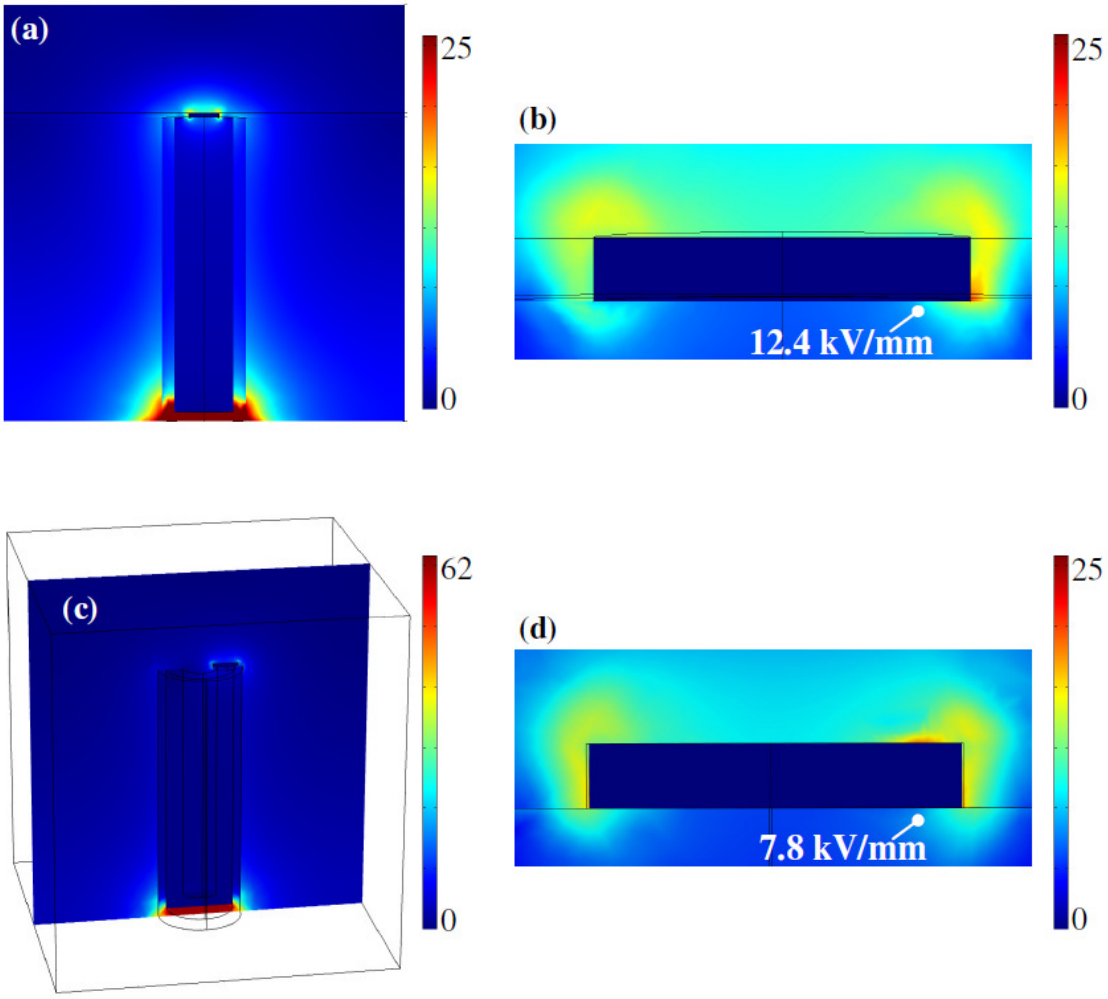

Figure 7.12: Electric field distribution for 1 V applied in a ~250 nm high PZT/ Al_2O_3 nanotube (20nm-thick PZT, 10 nm-thick Al_2O_3) (a) a hard-template-grown and (c) a soft-template-grown. Localized view of the electric field directly below the AFM-tip for the PZT nanotube (b) hard-template-grown and (d) soft-template-grown.

The PZT nanotubes in the hard- and soft-template used in this study have analogous dimensions (20 nm tube width and 5:1 aspect ratio). This tube geometry was chosen based-on previous results: a PZT thickness of 20 nm is greater than the critical size, and a high aspect ratio ensures that substrate clamping does not dominate the piezoelectric response.

The hard-template's piezoresponse loop shows a significant reduction in the remanent piezoresponse and saturation compared to the soft-template. The reduction in remanent and saturation polarization is attributed to lateral constraint. When an electric field is applied to the top of the PZT nanotube via the AFM tip, the material deforms longitudinally due to the d_{33} piezoelectric response. However, any longitudinal response is also accompanied by lateral deformation through d_{31} piezoelectric response (Figure 7.13). However, in the case of the hard-template-grown nanotubes, the adjacent ~300 nm-thick FOX 16 (non-piezoelectrically active surrounding media) prevents the 20 nm PZT wall from radial elastic deformation, thus leading also to a reduced longitudinal piezoelectric response, and hence reduced remanent and saturation piezoresponse. The inability of the PZT material to deform (i.e. freely expand) also results in an increased coercive field.

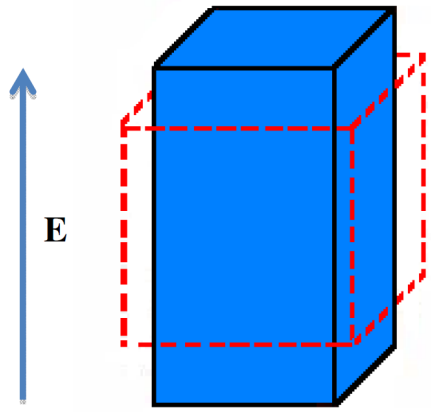

Figure 7.13: Schematic illustration of the longitudinal and lateral response of a piezoelectric material when an electric field is applied. Red, dashed curves represent the structure before application of the external electric field (E) and the black, bold lines the structures under applied electric field.

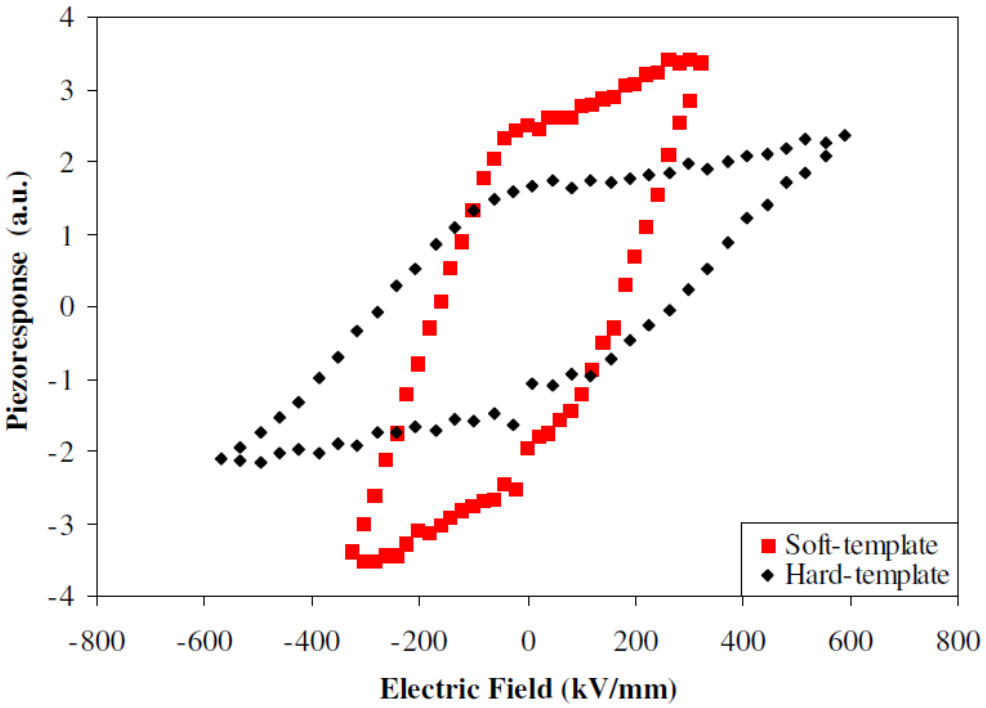

Figure 7.14: SS-PFM piezoresponse hysteresis loops (arbitrary units) for hard-template (red square) and soft-template (black diamond) grown 5:1 PZT nanotubes with 20 nm-thick PZT walls.

Table 7.1: Piezoresponse parameters for hard- and soft- template grown 5:1 PZT nanotubes with 20 nm-thick PZT walls.

	Coercive Field (kV/mm)	Remanent Piezoresponse (a.u.)	Saturated Piezoresponse (a.u.)
Hard-Template	264	1.6	2.4
Soft-Template	144	2.5	3.4

A comparison of the Rayleigh parameters and their ratios for the hard-template and soft-template grown PZT nanotubes is shown in Table 7.2. The hard template had a lower irreversible Rayleigh parameter, a higher reversible Rayleigh parameter, and a

lower ratio of irreversible to reversible Rayleigh parameters. The lower irreversible Rayleigh parameter and Rayleigh parameters' ratio is attributed to a reduction in irreversible domain wall motion because of lateral constraint.

The increased reversible Rayleigh parameter for the tubes embedded in the hard template could be due to an increased extrinsic contribution from reversible domain wall vibration and motion. Figure 7.15 illustrates the potential energy landscape for strong and weak domain wall pinning. For strong pinning, deep energy wells prevent irreversible motion and cause the domains to only vibrate within the energy wells, while under the same external fields for weak pinning the shallow wells lead to enhanced irreversible motion. Therefore, the increase in the reversible contribution for the PZT tubes in embedded in the hard template is possibly a result of extensive pinning caused by lateral constraint, which can result in enhanced reversible extrinsic contribution.

Table 7.2: Reversible and irreversible Rayleigh parameters for hard- and soft- template grown 5:1 PZT nanotubes with 20 nm-thick PZT walls.

	$\beta d_{33,init}$ (a.u.)	$\beta\alpha$ (a.u.)	$\alpha/d_{33,init}$ (x10^{-3} mm/kV)
Hard-Template	7.9	41.5	5.3
Soft-Template	2.3	95.5	41.5

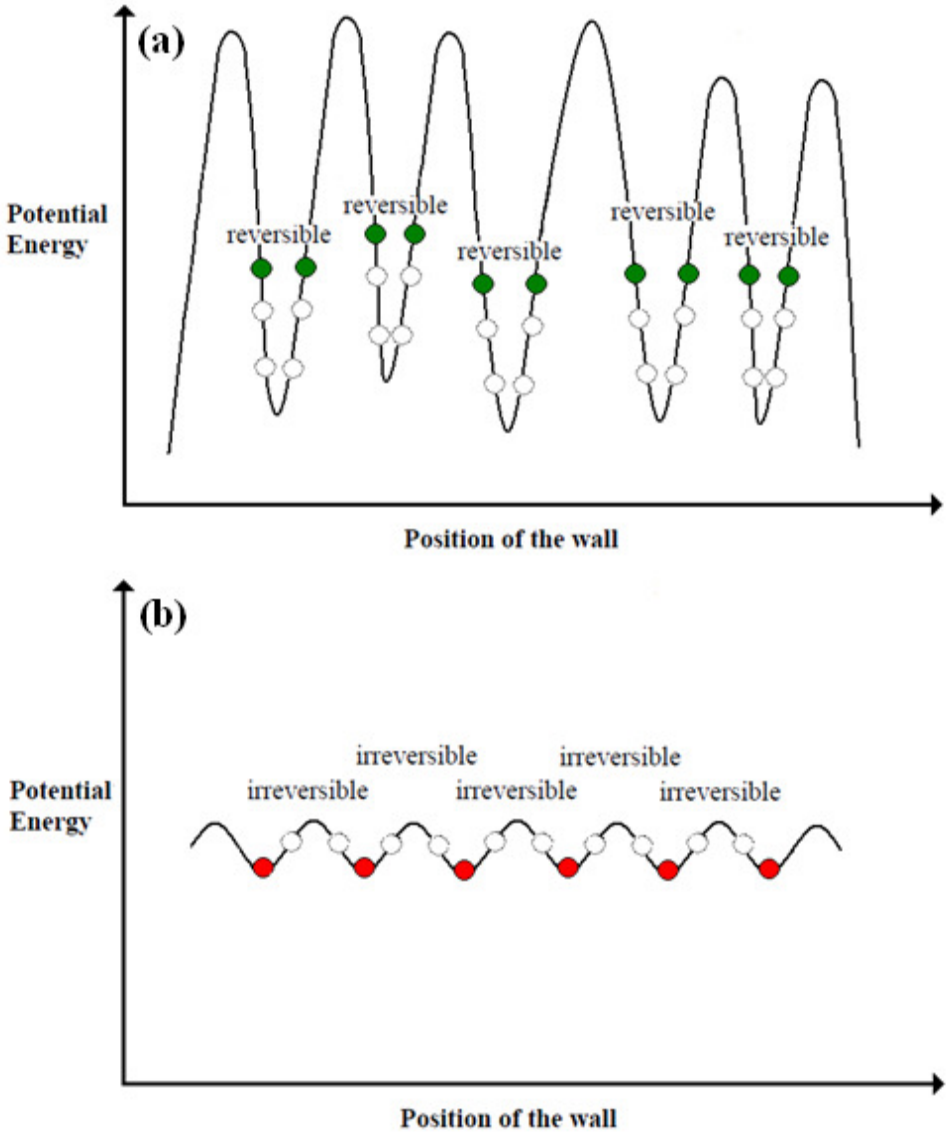

Figure 7.15: A schematic illustration of the potential energy landscape for (a) strongly pinned domain walls and (b) weakly pinned domains. The dotted circles represent the motion of the walls. Ultimately, the wall will shift to the minimum potential energy.

The effects of mechanical constraints on the piezoelectric response in ferroelectrics have been previously studied theoretically. For instance, Ahluwalia and Cao studied the influence of surface constraint, i.e. semi-infinite (corner free) geometry vs. a square-shaped finite sized constrained ferroelectric, during polarization switching

using a time-dependent Ginzburg-Landau model with the addition of gradient electrostatic and elastic energy terms. For modeling the bulk system, a periodic boundary condition was employed in the x- and y-direction corresponding to an infinite system, while for the finite-sized, constrained ferroelectric structure, a boundary condition of vanishing polarization at the surface was used. Results from the model predicted a reduction in saturation and remanent polarizations for the finite-sized, constrained ferroelectric systems with respect to bulk systems [146].

Li et al. also developed a finite element model for constrained domain switching in polycrystalline ceramics. The model assumes that the polycrystalline ferroelectric is comprised of numerous oriented grains, each containing N types of domains, where N=6 for a tetragonal case and N=8 for a rhombohedral case. For an unpoled ferroelectric, the fraction of each type of domain in a single grain is assumed to be 1/N, resulting in a zero remanent polarization in each grain. In this model, charge-screening effects typically observed in real ceramics is also taken into account by assuming the depolarization field induced by a polarization gradient is completely compensated by free charges. These free charges are trapped by unbalanced polarization until the polarization in the material switches. In addition, the internal stress induced by non-180^{o} domain switching is considered in an Eshelby inclusion manner: each grain in a polycrystalline ceramic is treated as a spherical inclusion in an infinite elastic matrix and the strain induced by non-180^{o} domain switching is averaged over the entire grain. Numerical results from this model for the tetragonal case indicated that during electric poling only a few percent (~3 to 4%) of 90^{o} switching occurred in a constrained polycrystalline ceramic as compared to 180^{o} switching [150].

The results of both of the above mentioned theoretical models are consistent with the experimental trends observed for laterally constrained PZT nanotubes: the embedded PZT nanotubes exhibited reduced saturated and remanent piezoresponse in addition to limited extrinsic contributions to the nonlinear response, an indication of reduced irreversible domain wall motion in the small scale ferroelectrics.

In summary, clear trends were observed in the extrinsic contribution to the piezoelectric response as a function of aspect ratio and wall thickness. As the aspect ratio (height: width) of the PZT nanotube increased, the extrinsic contributions increased, conceivably through a reduction in the percentage (i.e. average strength) of the material clamped to the underlying substrate. As the wall thickness of the nanotubes increased, an enhanced extrinsic contribution was also realized, possibly due to an increase in grain size, leading to a reduction in grain boundaries, which act as pinning sites for domain wall motion. Furthermore, lateral constraint also affected the extrinsic contribution to the piezoelectric response. A severe reduction in the extrinsic contribution was observed for PZT nanotubes created in a hard-template compared to a soft-template and was most likely due to the inability of the PZT nanotube to deform radially, leading to a reduced longitudinal piezoelectric response.

CHAPTER 8

CONCLUSIONS AND FUTURE WORK

This chapter briefly summarizes the major findings in this thesis. Based on experimental observations, possible directions for future work are recommended.

8.1 Summary and Conclusions

One of the major limitations of the technological advancement of micro- and nano-scale piezoelectric devices is the current lack of manufacturing methods that would allow tailoring of the shape, aspect ratio, and fill factor of the piezoelectric material on a single, given substrate. Many of these limitations are overcome with the soft-template infiltration method herein demonstrated. Specifically, leveraging e-beam lithography to create the soft templates, ferroelectric nanotubes were fabricated on platinized Si substrates. The diameter of the nanotubes can be controlled and varied, within the same sample, by the user-defined e-beam pattern. In addition, the height of the soft-template and wall tube thickness can be altered by modifying the spin-coating conditions and increasing the number of infiltration procedures performed, respectively. $PbZr_{0.52}Ti_{0.48}O_3$ (PZT) nanotubes were fabricated with aspect ratios from 1.25:1 to 5:1 and thicknesses from 5 nm to 25 nm.

Key processing steps for soft-template PZT nanotube fabrication included:

(1) coating the polymeric template with a thin layer of Al_2O_3 via ALD, prior to PZT immersion, for mechanical consolidation and to prevent chemical reactions between the PZT precursor solution and the polymeric template;

(2) infiltration of the PZT sol-gel precursor under vacuum within an ultrasonic bath to overcome the super-hydrophobic nature of the patterned soft-template surface;

(3) development of a hierarchical patterning scheme to prevent cracks and delamination; and

(4) refinement of the heat treatment profile to a two step crystallization process, which allowed a slower and more gradual decomposition of the resist and alleviated stiction issues between adjacent nanotubes.

This work can improve device development by fulfilling alignment requirements necessary for device fabrication. In addition, the high aspect ratio structures with limited lateral constraint (due to the use of vacuum infiltration of soft-templates) have enhanced piezoelectric response compare to thin films of similar thickness, which enables the creation of numerous devices currently unavailable to due to the lack of processing methods. Specifically, an array of nanotubes created via the soft-template infiltration procedure can be used as actively tunable photonic crystals to guide the propagation of electromagnetic waves. The dielectric permittivity can be tuned via the ferroelectric response and the aspect ratio of structures can be altered through the piezoelectric response, thus providing the means for active control of the refractive index of the periodic structures. High aspect ratio PZT nanotubes created via this new manufacturing

approach discussed herein can also possibly be used as THz emitters, which have potential applications in security screening and biological imaging. Piezoelectric nanotubes are also extremely attractive for energy harvesting applications due to their flexibility, low weight, and fail safe mode (if a single nanotube fails the device is still capable of harvesting energy). In addition, by increasing the number of infiltrations performed, the tubes can be nearly transformed into high aspect ratio pillars, thus providing the means for ultrasonic imaging of low depth penetration tissues such as the dermis and cornea[39]. Also, 1-3 patterned piezoelectrics (such as those created via this approach) have shown to exhibit a lower impedance than full piezoelectric ceramics, allowing for more efficient impedance matching with organic tissues, therefore minimizing the reflection of sound waves back to the detector at the interface, thus improving image resolution [71].

The development of this soft-template manufacturing method is not only advantageous for future development of active nanoelectromechanical systems (NEMS), but also provides the means to further characterize size effects in polycrystalline ferroelectric materials at the small scale. The main scientific questions that were addressed by this work included: how the extrinsic piezoelectric contributions in nanometer-sized ferroelectric materials are affected by clamping (via lateral constraint as well as by the underlying substrate) and what is the critical value (wall thickness) for ferroelectric nanostructures below which absence of non-180^o domain walls can lead to reduced extrinsic contributions to the piezoelectric response.

[39] The frequency of the emitted sound wave is dependent on the aspect ratio of the piezoelectric material. High aspect ratio materials produce higher frequency sound waves than low aspect ratio structures. These high frequency waves emitted are used for low depth penetration tissue imaging with high resolution.

Results from this research showed an increase in the extrinsic contributions to the piezoelectric response as the aspect ratio of the tube increased: for aspect ratios below 3:1, the extrinsic contributions were negligible. Only at higher aspect ratios (greater than 3:1), any extrinsic contribution was observed (low and intermediate-field piezoelectric nonlinearity). Above this critical aspect ratio, the extrinsic contributions to the piezoelectric response continuously increased with increased height-to-width of the nanostructures. This increase was attributed to a reduction in the substrate clamping conditions. No saturation in the extrinsic contribution to the piezoelectric was observed for the range of aspect ratios studied (1.25:1 to 5:1), thus surprisingly, even at aspect ratios of 5:1, substrate clamping is still influencing the overall piezoelectric response of the ferroelectric nanostructures.

The effect of lateral constraint was studied by comparing the piezoresponse of PZT nanotubes created in hard- and soft-templates. A reduction in the extrinsic contributions was observed for PZT nanotubes embedded in the hard-template, which indicates reduced mobility of the internal interfaces in a laterally constrained geometry. This reduction in mobility is attributed to presence of lateral constraints that reduce the ferroelastic deformation through the motion of non-180^{o} domain walls. Thus, the soft-template infiltration method is not only advantageous from a manufacturing perspective but also produces PZT nanotubes with enhanced piezoelectric response. Future studies will include quantitative studies to determine whether substrate clamping or lateral constraints have a larger impact on the piezoelectric response of ferroelectric materials at sub-micron scales (see section 8.2.3).

Minimal lateral constraint and substrate clamping in the soft-template-processed samples also led to a substantially larger amount of extrinsic contributions to the piezoresponse for PZT nanotubes when compared to PZT thin films of similar stack configuration and thickness. Furthermore, the observed extrinsic critical thickness (i.e. critical length scale above which ferroelastic domain formation is energetically favorable) in PZT nanotubes was in superior agreement with previous theoretical predictions. The experimentally observed critical thickness for the PZT nanotubes was ~10-15 nm, while theoretical studies have previously estimated the critical thickness for $PbTiO_3$ at ~10 nm [109].

It has to be pointed out that in addition to enabling creation of a range of new optoelectromechanical nano/micro-scale devices and empowering the study of nanoscale phenomena in ferroelectric materials, the proposed nanomanufacturing method is adaptable for a variety of ceramic materials by appropriate choice of chemical solution precursors and thermal processing profiles. Furthermore, this manufacturing method is easily scalable to large patterned areas, by use of nanoimprint lithography (NIL) instead of EBL for creation of the soft templates (see section 8.2.1). Finally, any substrate capable of withstanding the ferroelectric material's processing temperature (800 ^{o}C) can be used, due to the lack of epitaxial growth requirements.

8.2 Future Work

The following sections detail suggested future works for the advancement of the PZT nanotubes' manufacturing procedure, as well as further characterization, and future scientific studies.

8.2.1 Manufacturing Advancements

In order to increase throughput for device fabrication and reduce overall processing cost, parallel-processing through nanoimprint lithography (NIL) is a more advantageous approach with respect to in-series processing as offered by EBL for creation of the soft-templates. The NIL process is schematically shown in Figure 8.1. A nanostructured-surface mold is pressed into a thin layer of polymer/resist (for example ma-N 2403) under appropriate temperature and pressure profiles. After the pattern is appropriately transferred to the polymer, the mold is removed. The patterned polymer and substrate are subjected to a de-scum process in order to remove the residual resist in the compressed region. For creation of PZT nanotubes, the soft-templates are then vacuum-infiltrated in a similar procedure as used for the EBL-created templates (including coating with ALD-deposited alumina or other oxide and vacuum-infiltrating with PZT precursor). The major advantage of this method is that it is an "in parallel" method. Additionally, the mold can be used multiple times, and/or for large surfaces with large translational symmetry, a roll-on nano-imprint approach can be used [151-152].

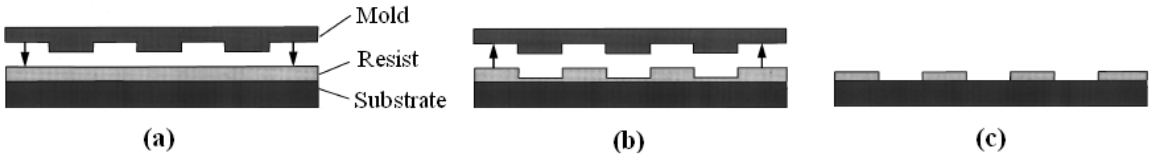

Figure 8.1: Schematic representation of nanoimprint lithography work-flow. (a) Imprinting of the resist via a hard mold, (b) mold removal, and (c) reactive ion etching (i.e. descum) to remove residual resist in the compressed regions.

The NIL Si[40] mold is produced by spin coating an e-resist on a Si substrate. The e-resist is then patterned via EBL, and the pattern is transferred to the underlying silicon wafer by inductively coupled plasma (ICP) etching. An important consideration in etching these small features is selectivity (etch rate of silicon compared to the resist). ZEP520 (Zeon Chemicals L.P.) is a suggested e-resist, because of its high (11:1) selectivity for Si, which allows the creation of high aspect ratio features. Additionally, in order to overcome the scalloped features along the length of the Si pillars as typically observed in the Bosch process, a quick chemical etch might be necessary.

Key parameters requiring optimization for NIL-processing include the imprint temperature, pressure, duration, and de-mold temperature. In addition, if adhesion issues arise, an appropriate anti-stiction coating may need to be developed.

To further develop the soft-template infiltration method for future devices, a means for electroding an array of tubes needs to be developed. One of the most important challenges faced is the possible shorting of top and bottom electrodes through the unpatterned regions (Figure 8.2a,b). One possible way to overcome this issue is to backfill the unpatterned regions with polymer prior to the top electrode material deposition. A lift-off technique can then be leveraged to strip the polymer and remove the platinum from the unpatterned regions. Alternatively the polymer could be kept, leading to the creation of a continuous top (Pt) electrode.

[40] Quartz hard molds could also be produced by appropriate choice of mask material for high selectivity. Often Cr masks are used for etching quartz. To etch chromium, typically HSQ or ZEP520 resist is patterned via EBL and the features are subsequently transferred into the Cr layer via ICP etching with Cl_2 and O_2 process gases. The quartz mold is then etched with CF_4, C_4F_8, and O_2 process gases. Although manufacturing quartz NIL-molds requires two etch steps (Cr mask etch followed by quartz stamp etch) in one respect quartz is even more ideal as a NIL-mold than Si because of its nearly temperature-independent thermal expansion coefficient.

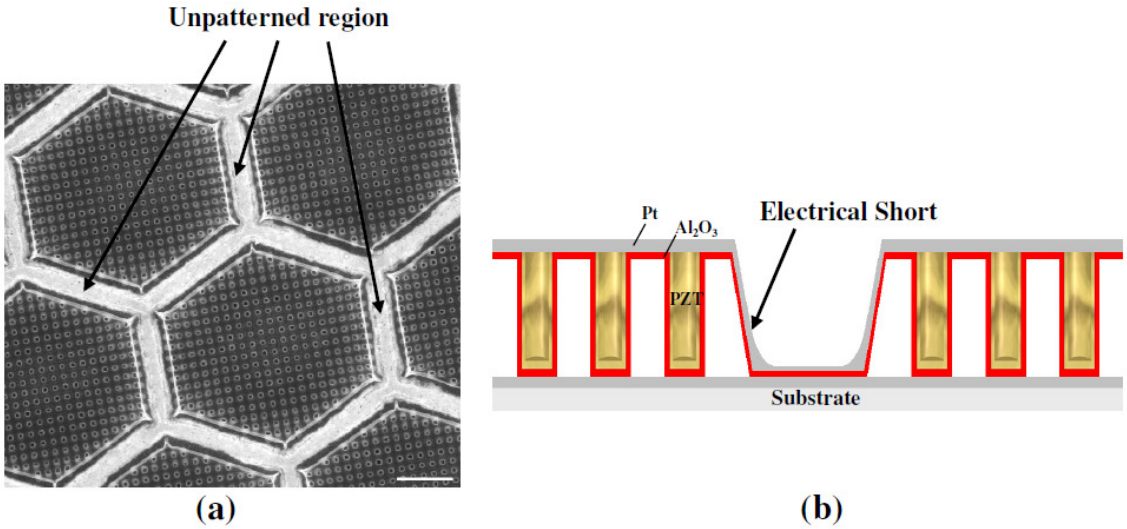

Figure 8.2: (a) Top-view SEM image of PZT nanotubes' array, highlighting the unpatterned regions. (b) Cross-sectional view illustrating possible location of electrical short between top and bottom electrode after platinum sputter deposition without backfilling.

Another suggested manufacturing advancement towards device creation is by replacement of the ALD-deposited Al_2O_3 layer with a different oxide composition. Specifically, TiO_x is recommended as previous literature reports show that a thin layer of titania can be absorbed in the chemically-processed PZT [153]. The improved chemical homogeneity is expected to result in further reduction (or possible elimination) of lateral constraint in the nanotubes, and hence improved piezoelectric response, as well as prevention of the significant drop in the electric field at the current PZT/Al_2O_3 interface. Another possible replacement is ZnO. Although the permittivity of zinc oxide (ε_r=1.7-2.5) is lower than Al_2O_3 (ε_r = 13), ZnO is a piezoelectrically-active material, and thus could contribute to the overall piezoelectric response of the nanostructures. Replacement of the Al_2O_3 layer with either of the aforementioned materials will require optimization of the pulse and purge times during the ALD processing, in order to ensure an adequate

number of pin holes for the removal of the chemical byproducts of the e-resist's decomposition, while still functioning as a chemical barrier between the PZT chemical precursor and the e-resist.

8.2.2 Microstructural Analysis

Transmission electron microscopy (TEM) studies are proposed in order to characterize the PZT grain size in the nanotubes and study the eventual domain formation. TEM imaging is performed by detecting electrons in transmission through the sample. TEM analysis of the PZT nanotubes would provide the capability to further verify the extrinsic size effect via studying the types of domain patterns formed as a function of tube thickness. Based on the current results (section 7.3), it is expected that non-180^{o} domain walls will be observed only in PZT nanotubes with wall thickness superior to ~10 nm.

The primary difficulty with many TEM analyses is sample preparation. Traditional lift-out techniques[41] could be performed, however, these are exceptionally challenging due to the extremely small size of a single PZT nanotubes. A possible alternative is offered by simple "scratching" of the patterned regions with a microprobe, and analyzing the probe's tip. Preliminary results indicate that a small number of tubes remain attached to the probe tip, which can then be analyzed via TEM (Figure 8.3).

[41] Lift-out techniques use a FIB system to mill the sample into thinned pieces followed by freeing a small region of the sample from the underlying substrate. Next, the freed structure is attached to a needle via either electrostatic forces or welded to the needle's tip. The structure is then transported to and placed on a TEM grid.

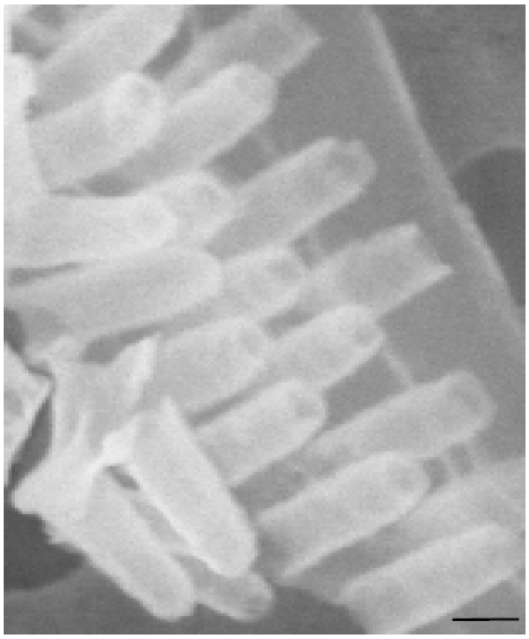

Figure 8.3: FE-SEM of 100 nm diameter PZT tubes, with ~15 nm wall thickness, mechanically removed from the underlying substrate and appended to a microprobe tip (scale bar 100 nm).

8.2.3 Substrate clamping

With the exception of the results discussed in section 7.2, no other experimental studies have been reported for trends in the remanent piezoresponse and coercive field for ferroelectric nanostructures with aspect ratios greater than 2:1. Recommended future studies include altering the soft-templates' material to thicker-deposited e-beam resists[42] or double spinning ma-N 2403 in order to fabricate PZT nanotubes with a range of aspect ratios greater than 5:1, the maximum aspect ratio studied in this research. Nonlinear measurements should be performed and analyzed via the Rayleigh law. It is expected

[42] A possible alternative is Sumika NEB 31, a negative tone resist with high contrast and very high resolution primarily due to a photoacid generator (PAG) that catalyzes molecular chain scission [154].

that the Rayleigh parameters' ratio will continue to increase as the aspect ratio of the ferroelectric nanostructures increases, due to a reduction in the percentage volume of material clamped to the substrate. Ultimately, the Rayleigh parameters' ratio is expected to saturate beyond a critical value. At this critical aspect ratio, substrate-clamping will no longer affect the piezoelectric response (i.e. is negligible), and the ferroelectric structures will behave as "effectively free-standing" nanotubes. The determination of this critical aspect ratio is of great significance in the development of miniaturized ferroelectric devices that require a large piezoelectric response. Furthermore, the results would allow to shed light into the stress-release length scale in free-standing versus laterally clamped ferroelectric structures, by a direct comparison with thin films of similar thickness.

Additional future studies should also include investigating whether substrate clamping or lateral constraint is the dominant factor controlling the effective piezoelectric coefficient in partially constrained ferroelectrics. To perform these studies PZT nanotubes will be processed in hard-templates with a range of aspect ratios similar to those created by soft-template infiltration[43]. The aspect ratios of the PZT nanotubes embedded in the hard-template can be altered with the same approach used for the soft-template-grown samples, i.e. by adjusting the spin coating conditions of FOX 16 e-beam resist, which ultimately determines the height of the PZT nanotubes. Nonlinear piezoelectric measurements should be performed and studied via the Rayleigh analysis. The Rayleigh parameters' ratio should be studied (rather than solely the irreversible Rayleigh coefficient or other material parameters such as the remanent piezoresponse) because of its independence from the photodiode's and cantilever's sensitivities, allowing

[43] FOX 16 is thicker than ma-N 2403 at similar spin-speeds. Thus, either FOX 16 needs to be diluted to fabricate soft-templates with similar thicknesses or ma-N 2403 needs to be double spun.

a quantitative approach for the study of the extrinsic piezoelectric response, independently from the choice of cantilever and the tip contact mechanics with the sample's surface. The piezoelectric Rayleigh parameters' ratio as a function of the nanotubes' aspect ratio should be compared for PZT nanotubes created in the hard- and soft-template with the same PZT wall thickness. The suggested wall thickness for this study is 20 nm to ensure critical thickness effects do not dominate the response (see section 7.2). The Rayleigh parameters' ratio for the hard-template PZT nanotubes is always expected to be lower than the soft-template PZT nanotubes due to additional lateral constraint. Preliminary results for data collected as a function of aspect ratio for both hard- and soft-templates are shown in Figure 8.4. Of particular interest is the data for aspect ratios ranging from 3.5:1 to 5:1 and higher. Depending on the slope of the trend line for PZT nanotubes manufactured in the hard-template for this range of aspect ratios, conclusions can be drawn regarding whether substrate clamping or lateral constraint is the dominant factor in the reduction of the extrinsic contributions to the piezoelectric response. A lower slope in the Rayleigh parameters' ratio as a function of aspect ratio for the PZT nanotubes grown in hard-templates than those grown in soft-templates would indicate a larger contribution from lateral constraint to the reduction of extrinsic piezoelectric response than substrate clamping in the nanostructures. If the slope of the trend-line for the hard-templates is approximately the same as the soft-template, then both lateral constraint and substrate clamping influence the response in equal measure (i.e. neither dominate).

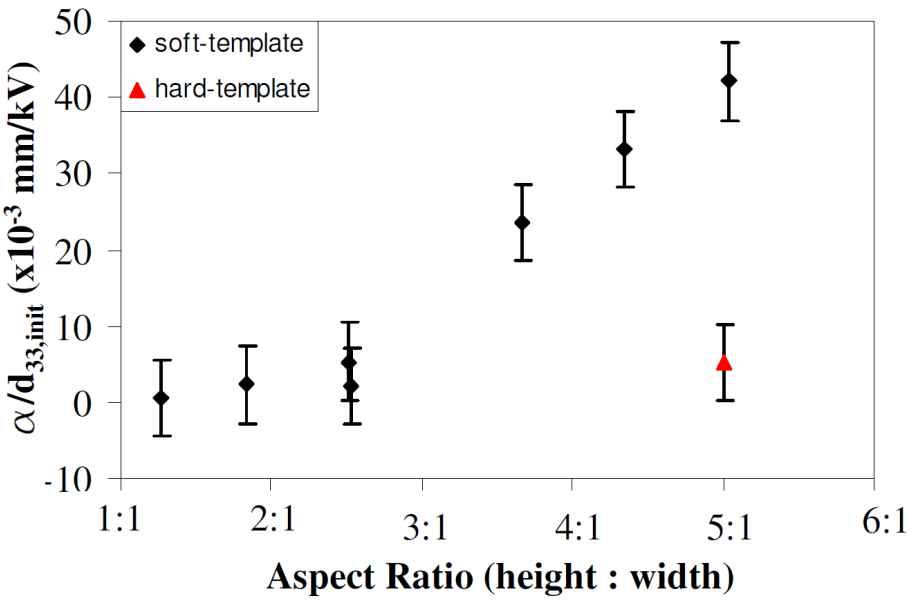

Figure 8.4: Preliminary nonlinear piezoelectric results for PZT nanotubes created in hard- and soft-templates. These results, in addition to future work, will provide the means to determine whether substrate clamping or lateral constraint in the dominant factor controlling the effective piezoelectric coefficient in partially constrained, submicron-sized ferroelectrics

8.2.4 Vortex Domains

Ferroelectricity and domain formation is a collective phenomena resulting from long-range dipole interaction and short-range covalent interaction [155]. In nanostructures, both long-rang dipole and short-range covalent interactions are varied with respect to those in bulk ferroelectrics, at time giving rise to unusual vortex structures. Based on theoretical simulations, it is expected that a critical aspect ratio exists, above which vortex domain formation is no longer energetically favorable.

Experimental evidence of vortex domain formation in PZT nanodots was recently reported in a study performed by Rodriguez et. al [156]. A model called “piezoelectric

surface approach" was used to determine virtual PFM images based on an assumed toroidal moment of polarizations. Vertical PFM (VPFM) and lateral PFM (LPFM) measurements were then performed on PZT (40/60) nanodots to determine the local in-plane and out-of-plane polarization. The agreement of the measured response to the virtual PFM images suggested the existence of vortex polarization. Gruverman et. al have also previously reported a circular domain pattern in 1 μm-diameter circular PZT capacitors [157]. However, a clear understanding of the origin of such polarization patterns in ferroelectric nanostructures is still lacking.

Therefore, it would be interesting to perform similar PFM measurements (both VPFM and LPFM) on PZT nanotubes developed via soft-template infiltration to determine how the aspect ratio (i.e. size of the tube) affects the existence of vortex domains in polycrystalline samples. If vortex domain formation is not observed due to the polycrystalline nature of the samples or for this range of aspect ratios (1:1 to 5:1), then low aspect ratio (<1:1) "shape-controlled" PZT islands grown epitaxially on single-crystalline substrates could be manufactured using a similar approach to soft-template vacuum infiltration method.

In order to create "flat PZT islands", electron-sensitive resist can be patterned on $SrTiO_3$ followed by PZT deposition via vacuum-assisted infiltration or spin-coated deposition. The patterned resist is then removed by chemical or thermal means. Preliminary results using this method indicate the ability to create line-shaped structures in PZT films on platinized Si substrates (Figure 8.5).

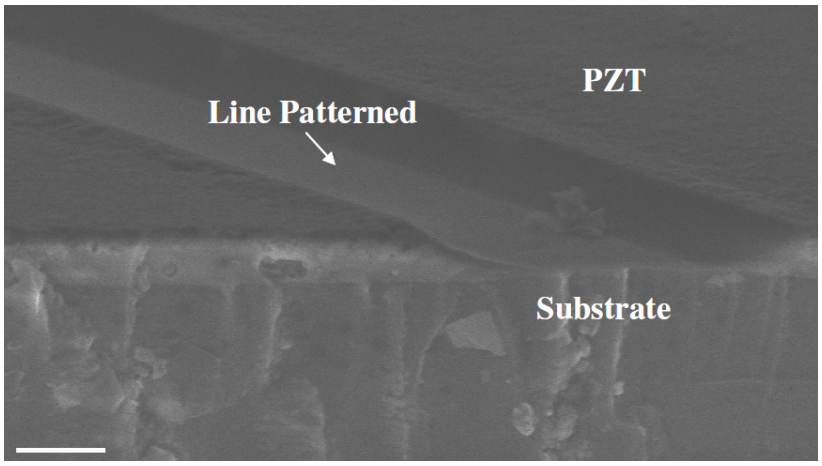

Figure 8.5: SEM image of thermal lift-off process developed to pattern PZT films on platinized Si substrates (scale bar 1 μm). A similar method can be developed for creating low-profile, epitaxial PZT nanostructures by changing the underlying substrate.

In order to study the effect of presence or absence of "corners" and sharp angles on vortex domain formation, the shape of the patterned resist features could be altered during EBL, which ultimately will determine the shape of the PZT. For instance, circular-, hexagon-, and square-shaped PZT patterns could be fabricated. For each of these patterned features, the dose, shot pitch, acceleration voltage, and beam current will require optimization.

Based on theoretical simulations, it is expected that there exists a critical aspect ratio above which vortex domain formation is no longer energetically favorable. In addition, tubular structures with various degrees of angular corners can alter long-range order which can negatively affect vortex domain formation. By investigating tubular PZT nanostructures with various aspect ratios and shapes, a better understanding of the origin of vortex-like polarization patterns can be gained.

APPENDIX

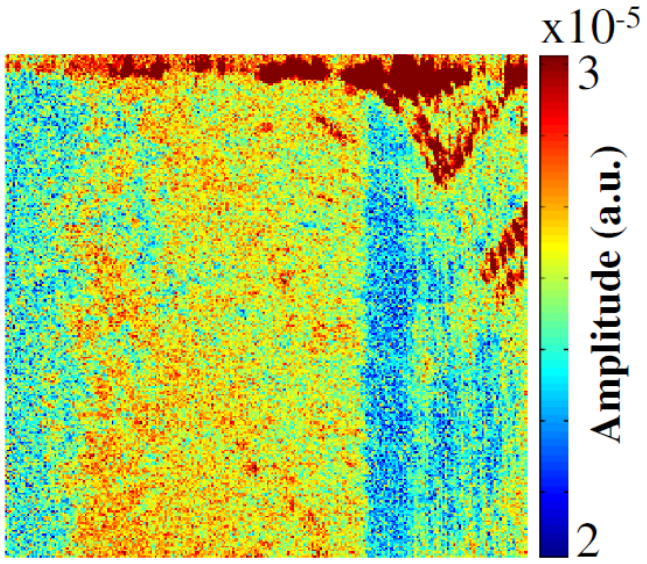

Figure A.1: Spatial BE-PFM output response for quartz calibration sample (1 μm by 1 μm scan area).

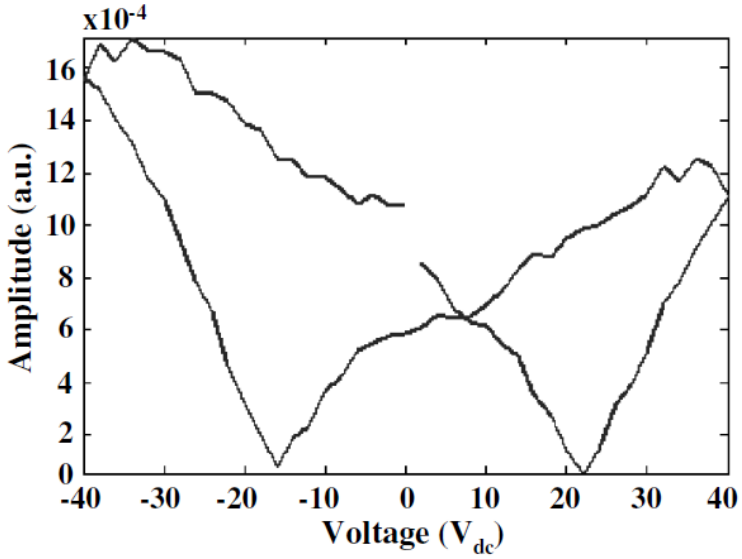

Figure A.2: SS-PFM maximum amplitude output response recorded for 100 nm PZT nanotubes with 5:1 aspect ratio.

REFERENCES

[1] D. A. Hall, "Review nonlinearity in piezoelectric ceramics," *Journal of Materials Science,* vol. 36, pp. 4575-4601, 2001.

[2] M. E. Lines, *Principles and applications of ferroelectrics and related materials*. Oxford: Clarendon Press, 2001.

[3] J. F. Nye, *Physical properties of crystals : their representation by tensors and matrices*. Oxford: Clarendon Press, 1979.

[4] G. Bertotti, Mayergoyz, I. D., *The science of hysteresis*. Amsterdam: Academic Press, 2006.

[5] R. E. Newnham, *Properties of materials : anisotropy, symmetry, structure*. Oxford: Oxford University Press, 2005.

[6] D. Damjanovic, "Ferroelectric, dielectric and piezoelectric properties of ferroelectric thin films and ceramics," *Reports on Progress in Physics,* vol. 61, pp. 1267-1324, 1998.

[7] "An american national standard IEEE standard definitions of terms associated with ferroelectric and related materials," *Ultrasonics, Ferroelectrics and Frequency Control, IEEE Transactions,* vol. 50, pp. 1-32, 2003.

[8] D. Damjanovic and D. V. Taylor, "Contributions to the nonlinear dielectric and piezoelectric response of ferroelectric thin films and ceramics," *Ferroelectrics,* vol. 221, pp. 137-146, 1999.

[9] V. Sundar and R. E. Newnham, "Electrostriction and polarization," *Ferroelectrics,* vol. 135, pp. 431-446, 1992.

[10] C. Kittel, "Theory of the structure of ferromagnetic domains in films and small particles," *Physical Review,* vol. 70, pp. 965-971, 1946.

[11] T. Mitsui and J. Furuichi, "Domain Structure of Rochelle Salt and KH_2PO_4," *Physical Review,* vol. 90, pp. 193-202, 1953.

[12] L. E. Cross, *Ferroelectric ceramics : tutorial reviews, theory, processing, and applications*. Basel Birkhäuser, 1993.

[13] E. I. Bondarenko, *et al.*, "The role of 90 degrees domain-wall displacements in forming physical-properties of perovskite ferroelectric ceramics," *Ferroelectrics Letters Section,* vol. 13, pp. 13-19, 1991.

[14] B. Lewis, "Energy loss processes in ferroelectric ceramics," *Proceedings of the Physical Society of London,* vol. 73, pp. 17-24, 1959.

[15] N. Bassiri-Gharb, "Dielectric and piezoelectric nonlinearities in oriented PYbN-PT thin films," Materials Science and Engineering, Pennsylvania State University, State College, 2007.

[16] R. Herbiet, *et al.*, "Domain-wall and volume contributions to material properties of PZT ceramics," *Ferroelectrics,* vol. 98, pp. 107-121, 1989.

[17] Y. M. Poplavko, *et al.*, "Microwave dielectric dispersion of ferroelectric and paraelectric phases of barium titanate," *Soviet Physics Solid State,Ussr,* vol. 10, pp. 2708, 1969.

[18] A. V. Turik and N. B. Shevchenko, "Dielectric spectrum $BaTiO_3$ single-crystals," *Physica Status Solidi B-Basic Research,* vol. 95, pp. 585-592, 1979.

[19] G. Arlt, *et al.*, "Dielectric-dispersion of ferroelectric ceramics and single-crystals at microwave-frequencies," *Annalen Der Physik,* vol. 3, pp. 578-588, 1994.

[20] Q. M. Zhang, *et al.*, "Direct evaluation of Domain-wall and Intrinsic Contribution to the Dielectric and Piezoelectric Response and Their Temperature-Dependence on Lead-Zirconate-Titanate Ceramics," *Journal of Applied Physics,* vol. 75, pp. 454-459, 1994.

[21] K. Carl and K. H. Hardtl, "Electrical Aftereffects in $Pb(Ti,Zr)O_3$ Ceramics," *Ferroelectrics,* vol. 17, pp. 473-486, 1978.

[22] G. Arlt, H. Dederichs and R. Herbiet, "90^o domain wall relaxation in tetragonally distorted ferroelectric ceramics," *Ferroelectrics,* vol. 74, p. 37-53, 1987.

[23] R. Herbiet, *et al.*, "Domain-wall and volume contributions to material properties of PZT ceramics," *Ferroelectrics,* vol. 98, pp. 107-121, 1989.

[24] A. Kholkin, "Non-linear piezoelectric response in lead zirconate-titanate (PZT) films," *Ferroelectrics,* vol. 238, pp. 799-807, 2000.

[25] Q. M. Zhang, *et al.*, "Domain-wall excitations and their contributions to the weak-signal response of doped lead zirconate titanate ceramics," *Journal of Applied Physics,* vol. 64, pp. 6445-6451, 1988.

[26] S. P. Li*, et al.*, "The extrinsic nature of nonlinear behavior observed in lead zirconate titanate ferroelectric ceramic," *Journal of Applied Physics,* vol. 69, pp. 7219-7224, 1991.

[27] L. Rayleigh, *Philosophy Magazine* vol. 23, 1887.

[28] D. Damjanovic and M. Demartin, "The Rayleigh law in piezoelectric ceramics," *Journal of Physics D-Applied Physics,* vol. 29, pp. 2057-2060, 1996.

[29] D. V. Taylor and D. Damjanovic, "Evidence of domain wall contribution to the dielectric permittivity in PZT thin films at sub-switching fields," *Journal of Applied Physics,* vol. 82, pp. 1973-1975, 1997.

[30] D. V. Taylor and D. Damjanovic, "Domain wall pinning contribution to the nonlinear dielectric permittivity in Pb(Zr, Ti)O_3 thin films," *Applied Physics Letters,* vol. 73, pp. 2045-2047, 1998.

[31] D. Damjanovic and M. Demartin, "Contribution of the irreversible displacement of domain walls to the piezoelectric effect in barium titanate and lead zirconate titanate ceramics," *Journal of Physics-Condensed Matter,* vol. 9, pp. 4943-4953, 1997.

[32] M. Demartin and D. Damjanovic, "Dependence of the direct piezoelectric effect in coarse and fine grain barium titanate ceramics on dynamic and static pressure," *Applied Physics Letters,* vol. 68, pp. 3046-3048, 1996.

[33] D. Damjanovic, "Stress and frequency dependence of the direct piezoelectric effect in ferroelectric ceramics," *Journal of Applied Physics,* vol. 82, pp. 1788-1797, 1997.

[34] M. Davis*, et al.*, "Temperature dependence of the direct piezoelectric effect in relaxor-ferroelectric single crystals: Intrinsic and extrinsic contributions," *Journal of Applied Physics,* vol. 100, pp. 084103, 2006.

[35] A. Bernal*, et al.*, "Effects of orientation and composition on the extrinsic contributions to the dielectric response of relaxor-ferroelectric single crystals," *Applied Physics Letters,* vol. 95, pp. 142911, 2009.

[36] D. Kobor*, et al.*, "Dielectric and mechanical nonlinearities of (001) oriented pure and doped single crystals of PZN-4.5PT," *Journal of Physics D-Applied Physics,* vol. 38, pp. 2258-2264, 2005.

[37] D. A. Hall and P. J. Stevenson, "High field dielectric behaviour of ferroelectric ceramics," *Ferroelectrics,* vol. 228, pp. 139-158, 1999.

[38] S. Trolier-McKinstry and P. Muralt, "Thin film piezoelectrics for MEMS," *Journal of Electroceramics,* vol. 12, pp. 7-17, 2004.

[39] P. Muralt, "Recent progress in materials issues for piezoelectric MEMS," *Journal of the American Ceramic Society,* vol. 91, pp. 1385-1396, 2008.

[40] S. A. Wilson*, et al.*, "New materials for micro-scale sensors and actuators: An engineering review," *Materials Science & Engineering R-Reports,* vol. 56, pp. 1-129, 2007.

[41] B. Noheda*, et al.*, "Phase diagram of the ferroelectric relaxor (1-x)$PbMg_{1/3}Nb_{2/3}O_3$-x$PbTiO_3$," *Physical Review B (Condensed Matter and Materials Physics),* vol. 66, pp. 054104-1, 2002.

[42] M. J. Madou, *Fundamentals of microfabrication: the science of miniaturization*, 2nd ed. Boca Raton: CRC Press, 2002.

[43] B. Jaffe, *Piezoelectric ceramics*. London: Academic Press, 1971.

[44] B. Noheda*, et al.*, "Tetragonal-to-monoclinic phase transition in a ferroelectric perovskite: The structure of $PbZr_{0.52}Ti_{0.48}O_3$," *Physical Review B,* vol. 61, pp. 8687-8695, 2000.

[45] B. Noheda*, et al.*, "Stability of the monoclinic phase in the ferroelectric perovskite $PbZr_{1-x}Ti_xO_3$," *Physical Review B,* vol. 63, pp. 014103, 2001.

[46] D. I. Woodward*, et al.*, "Review of crystal and domain structures in the $PbZr_xTi_{1-x}O_3$ solid solution," *Physical Review B,* vol. 72, pp. 104110, 2005.

[47] M. J. Haun*, et al.*, "Thermodynamic Theory of the Lead Zirconate-Titanate Solid-Solution System,.1. Phenomenology " *Ferroelectrics,* vol. 99, pp. 13-25, 1989.

[48] H. D. Chen*, et al.*, "Electrical-properties maxima in thin-films of the lead titanate solid-solution system," *Applied Physics Letters,* vol. 67, pp. 3411-3413, 1995.

[49] P. Muralt*, et al.*, "In-plane piezoelectric coefficient of PZT thin films as a function of composition," *Ferroelectrics,* vol. 224, pp. 663-670, 1999.

[50] A. Seifert*, et al.*, "Processing optimization of solution derived $PbZr_{1-x}Ti_xO_3$ thin films for piezoelectric applications," *Integrated Ferroelectrics,* vol. 35, pp. 1889-1896, 2001.

[51] R. A. Wolf and S. Trolier-McKinstry, "Temperature dependence of the piezoelectric response in lead zirconate titanate films," *Journal of Applied Physics,* vol. 95, pp. 1397-1406, 2004.

[52] T. Haccart, *et al.*, "Piezoelectric properties of PZT: Influence of (Zr/Ti) ratio and niobium substitution," *Ferroelectrics,* vol. 254, pp. 185-195, 2001.

[53] D. J. Kim, *et al.*, "Evaluation of intrinsic and extrinsic contributions to the piezoelectric properties of $Pb(Zr_{1-x}T_x)O_3$ thin films as a function of composition," *Journal of Applied Physics,* vol. 93, pp. 5568-5575, 2003.

[54] S. P. Palto and Y. A. Draginda, "Photonic Heterostructures with Properties of Ferroelectrics and Light Polarizers," *Crystallography Reports,* vol. 55, pp. 971-975, 2010.

[55] S. G. Kim, *et al.*, "Design of micro-photonic beam steering systems," *Cirp Annals-Manufacturing Technology,* vol. 51, pp. 335-338, 2002.

[56] H. H. Yue, *et al.*, "Distributed shell control with a new multi-DOF photostrictive actuator design," *Journal of Sound and Vibration,* vol. 329, pp. 3647-3659, 2010.

[57] J. F. Scott, *et al.*, "Terahertz Emission from Tubular $Pb(Zr,Ti)O_3$ Nanostructures," *Nano Letters,* vol. 8, pp. 4404-4409, 2008.

[58] J. Banys, *et al.*, "THz Emission from PZT Nanotubes," *Ferroelectrics,* vol. 378, pp. 79-83, 2009.

[59] M. Wilm, *et al.*, "Design guidelines of 1-3 piezoelectric composites dedicated to ultrasound imaging transducers, based on frequency band-gap considerations," *Journal of the Acoustical Society of America,* vol. 122, pp. 786-793, 2007.

[60] J. R. Yuan, *et al.*, "5C-5 High Frequency Piezo Composites Microfabricated Ultrasound Transducers for Intravascular Imaging," in *Ultrasonics Symposium,* vol. 1, pp. 264-268, 2006.

[61] Y. Hirata, *et al.*, "Piezocomposite of fine PZT rods realized with synchrotron radiation lithography," in *Ultrasonics Symposium, IEEE*, vol. 2, pp. 877-881, 1997.

[62] M. Umeda, *et al.*, "Energy storage characteristics of a piezo-generator using impact induced vibration," *Japanese Journal of Applied Physics Part 1-Regular Papers Short Notes & Review Papers,* vol. 36, pp. 3146-3151, 1997.

[63] G. W. Taylor, *et al.*, "The energy harvesting eel: A small subsurface ocean/river power generator," *IEEE Journal of Oceanic Engineering,* vol. 26, pp. 539-547, 2001.

[64] G. K. Ottman, *et al.*, "Optimized piezoelectric energy harvesting circuit using step-down converter in discontinuous conduction mode," *IEEE Transactions on Power Electronics,* vol. 18, pp. 696-703, 2003.

[65] P. Glynne-Jones, *et al.*, "Towards a piezoelectric vibration-powered microgenerator," *IEEE Proceedings-Science Measurement and Technology,* vol. 148, pp. 68-72, 2001.

[66] E. Hausler, *et al.*, "Implantable Physiological Power Supply with PVDF Film," *Ferroelectrics,* vol. 60, pp. 277-282, 1984.

[67] N. S. Shenck and J. A. Paradiso, "Energy scavenging with shoe-mounted piezoelectrics," *Micro, IEEE,* vol. 21, pp. 30-42, 2001.

[68] S. G. Johnson, *Photonic crystals : the road from theory to practice*. Boston: Kluwer Academic Publishers, 2002.

[69] G. M. H. Knippels, *et al.*, "Generation and complete electric-field characterization of intense ultrashort tunable far-infrared laser pulses," *Physical Review Letters,* vol. 83, pp. 1578-1581, 1999.

[70] K. L. Yeh, *et al.*, "Generation of 10 mu J ultrashort terahertz pulses by optical rectification," *Applied Physics Letters,* vol. 90, pp. 171121, 2007.

[71] C. G. Oakley and P. Marsh, "Development of 1-3 ceramic-air composite transducers (Invited Paper)," *Proceedings of the Society of Photo-Optical Instrumentaiton Engineers*, vol. 1733, pp. 274-283, 1992.

[72] A. Stanishevsky, *et al.*, "Radiation damage and its recovery in focused ion beam fabricated ferroelectric capacitors," *Journal of Applied Physics,* vol. 92, pp. 3275-3278, 2002.

[73] A. Stanishevsky, *et al.*, "Focused ion-beam patterning of nanoscale ferroelectric capacitors," *Journal of Vacuum Science & Technology B,* vol. 16, pp. 3899-3902, 1998.

[74] S. Gross, "Micromachined switches and cantilever actuators based on piezoelectric lead zirconate titanate (PZT)," Department of Electrical Engineering, The Pennsylvania State University, State College, 2004.

[75] S. A. Rocks, *et al.*, "Bottom up fabrication of a nickel-lead zirconate titanate piezoelectric microcantilevers," *Materials Letters,* vol. 63, pp. 88-90, 2009.

[76] W. Lee, *et al.*, "Individually addressable epitaxial ferroelectric nanocapacitor arrays with near Tb inch^2 density," *Nature Nanotechnology,* vol. 3, pp. 402-407, 2008.

[77] W. Lee, *et al.*, "Wafer-scale Ni imprint stamps for porous alumina membranes based on interference lithography," *Small,* vol. 2, pp. 978-982, 2006.

[78] J. Choi, *et al.*, "Fabrication of monodomain alumina pore arrays with an interpore distance smaller than the lattice constant of the imprint stamp," *Journal of Vacuum Science & Technology B,* vol. 21, pp. 763-766, 2003.

[79] Z. J. Sun and H. K. Kim, "Growth of ordered, single-domain, alumina nanopore arrays with holographically patterned aluminum films," *Applied Physics Letters,* vol. 81, pp. 3458-3460, 2002.

[80] I. Vrejoiu, *et al.*, "Functional perovskites - From epitaxial films to nanostructured arrays," *Advanced Functional Materials,* vol. 18, pp. 3892-3906, 2008.

[81] H. Han, *et al.*, "Wafer-scale arrays of epitaxial ferroelectric nanodiscs and nanorings," *Nanotechnology,* vol. 20, pp. 015301, 2009.

[82] C. Lu and R. H. Lipson, "Interference lithography: a powerful tool for fabricating periodic structures," *Laser & Photonics Reviews,* vol. 4, pp. 568-580, 2010.

[83] W. H. Ma, *et al.*, "Nanostructure patterns of piezoelectric and ferroelectric complex oxides with various shapes, obtained by natural lithography and pulsed laser deposition," *Nanotechnology,* vol. 17, pp. 2536-2541, 2006.

[84] W. Ma and D. Hesse, "Polarization imprint in ordered arrays of epitaxial ferroelectric nanostructures," *Applied Physics Letters,* vol. 84, pp. 2871-2873, 2004.

[85] A. Seifert, *et al.*, "Microstructural instability in single-crystal thin films," *Journal of Materials Research,* vol. 11, pp. 1470-1482, 1996.

[86] S. P. Alpay, *et al.*, "Can interface dislocations degrade ferroelectric properties?," *Applied Physics Letters,* vol. 85, pp. 2044-2046, 2004.

[87] V. Nagarajan, *et al.*, "Misfit dislocations in nanoscale ferroelectric heterostructures," *Applied Physics Letters,* vol. 86, pp. 192910, 2005.

[88] I. B. Misirlioglu, *et al.*, "Thermodynamic and electrostatic analysis of threading dislocations in epitaxial ferroelectric films," *Applied Physics Letters,* vol. 88, pp. 102906, 2006.

[89] H. Nonomura, *et al.*, "Structural control of self-assembled $PbTiO_3$ nanoislands fabricated by metalorganic chemical vapor deposition," *Applied Physics Letters,* vol. 86, pp. 163106, 2005.

[90] M. Alexe, *et al.*, "Patterning and switching of nanosize ferroelectric memory cells," *Applied Physics Letters,* vol. 75, pp. 1793-1795, 1999.

[91] C. Harnagea, *et al.*, "Mesoscopic ferroelectric cell arrays prepared by imprint lithography," *Applied Physics Letters,* vol. 83, pp. 1827-1829, 2003.

[92] J. Wang, *et al.*, "Large-Scale Fabrication of Titanium-Rich Perovskite PZT Submicro/Nano Wires and Their Electromechanical Properties," *IEEE Transactions on Ultrasonics Ferroelectrics and Frequency Control,* vol. 56, pp. 1813-1819, 2009.

[93] H. M. Cheng, *et al.*, "Hydrothermal synthesis of acicular lead titnate fine powders," *Journal of the American Ceramic Society,* vol. 75, pp. 1123-1128, 1992.

[94] S. Xu, *et al.*, "Piezoelectric-nanowire-enabled power source for driving wireless microelectronics," *Nature Communications,* vol. 1, pp. 1-5, 2010.

[95] S. S. N. Bharadwaja, *et al.*, "Fabrication of high aspect ratio ferroelectric microtubes by vacuum infiltration using macroporous silicon templates," *Journal of the American Ceramic Society,* vol. 89, pp. 2695-2701, 2006.

[96] H. J. Fan, *et al.*, "Concentric metallic-piezoelectric microtube arrays," in *Materials Science and Technology for Nonvolatile Memories*. vol. 1071, pp. 201-206, 2008.

[97] E. D. Mishina, *et al.*, "Ferroelectrics templated in nanoporous silicon membranes," *Ferroelectrics,* vol. 286, pp. 927-933, 2003.

[98] Y. Bastani, *et al.*, "Critical thickness for extrinsic contributions to the dielectric and piezoelectric response in lead zirconate titanate ultrathin films," *Journal of Applied Physics,* vol. 109, pp.014115 , 2011.

[99] K. Lee, *et al.*, "Two-dimensional planar size effects in epitaxial $PbTiO_3$ thin films," *Applied Physics Letters,* vol. 85, pp. 4711-4713, 2004.

[100] V. Nagarajan, *et al.*, "Dynamics of ferroelastic domains in ferroelectric thin films," *Nature Materials,* vol. 2, pp. 43-47, 2003.

[101] S. Buhlmann, *et al.*, "Size effect in mesoscopic epitaxial ferroelectric structures: Increase of piezoelectric response with decreasing feature size," *Applied Physics Letters,* vol. 80, pp. 3195-3195, 2002.

[102] K. Lee and S. Baik, "Ferroelastic domain structure and switching in epitaxial ferroelectric thin films," in *Annual Review of Materials Research*. vol. 36, pp. 81-116, 2006.

[103] J. Ryu, *et al.*, "Enhanced domain contribution to ferroelectric properties in freestanding thick films," *Journal of Applied Physics,* vol. 106, pp. 024108, 2009.

[104] S. Chattopadhyay, *et al.*, "Size-induced phase-transition in the nanocrystalline ferroelectric $PbTiO_3$," *Physical Review B,* vol. 52, pp. 13177-13183, 1995.

[105] K. Ishikawa, *et al.*, "Size effect on the phase transition in $PbTiO_3$ fine particles," *Japanese Journal of Applied Physics Part 1-Regular Papers Short Notes & Review Papers,* vol. 35, pp. 5196-5198, 1996.

[106] C. A. Randall, *et al.*, "Intrinsic and extrinsic size effects in fine-grained morphotropic-phase-boundary lead zirconate titanate ceramics," *Journal of the American Ceramic Society,* vol. 81, pp. 677-688, 1998.

[107] T. M. Shaw, *et al.*, "The properties of ferroelectric films at small dimensions," *Annual Review of Materials Science,* vol. 30, pp. 263-298, 2000.

[108] L. E. Tanner and M. F. Ashby, "On relief of ordering strains by twinning," *Physica Status Solidi,* vol. 33, pp. 59, 1969.

[109] L. D. Madsen, *et al.*, "Domain structures in $Pb(Zr, Ti)O_3$ and $PbTiO_3$ thin films," *Journal of Materials Research,* vol. 12, pp. 2612-2616, 1997.

[110] G. Arlt, "Twinning in ferroelectric and ferroelastic ceramics- stress relief," *Journal of Materials Science,* vol. 25, pp. 2655-2666, 1990.

[111] J. Hlinka, *et al.*, "The piezoelectric response of nanotwinned $BaTiO_3$," *Nanotechnology,* vol. 20, pp. 105709, 2009.

[112] R. Loudon, "Raman effect in crystals," *Advances in Physics,* vol. 13, pp. 423-474, 1964.

[113] T. E. Beechem, "Metrology of GaN electronics using micro-raman spectroscopy," Doctor of Philosophy in Mechanical Engineering, Mechanical Engineering, Georgia Institute of Technology, Atlanta, 2008.

[114] M. Alexe and A. Gruverman, *Nanoscale characterisation of ferroelectric materials : scanning probe microscopy approach*. Berlin: Springer-Verlag, 2004.

[115] J. W. Hong, *et al.*, "Measurement of hardness, surface potential, and charge distribution with dynamic contact mode electrostatic force microscope," *Review of Scientific Instruments,* vol. 70, pp. 1735-1739, 1999.

[116] K. Franke, *et al.*, "How to extract spontaneous polarization information from experimental data in electric force microscopy," *Surface Science,* vol. 415, pp. 178-182, 1998.

[117] S. V. Kalinin and D. A. Bonnell, "Contrast mechanism maps for piezoresponse force microscopy," *Journal of Materials Research,* vol. 17, pp. 936-939, 2002.

[118] S. Jesse, *et al.*, "The band excitation method in scanning probe microscopy for rapid mapping of energy dissipation on the nanoscale," *Nanotechnology,* vol. 18, pp. 435503, 2007.

[119] A. Kumar, *et al.*, "Real-space mapping of dynamic phenomena during hysteresis loop measurements: Dynamic switching spectroscopy piezoresponse force microscopy," *Applied Physics Letters,* vol. 98, pp. 202903, 2011.

[120] M. D. Groner, *et al.*, "Low-temperature Al_2O_3 atomic layer deposition," *Chemistry of Materials,* vol. 16, pp. 639-645, 2004.

[121] C. W. J. Berendsen, *et al.*, "Superhydrophobic surface structures in thermoplastic polymers by interference lithography and thermal imprinting," *Applied Surface Science,* vol. 255, pp. 9305-9310, 2009.

[122] H. Takemura, *et al.*, "Performance of new E-beam lithography system JBX-9300FS," *Microelectronic Engineering,* vol. 53, pp. 329-332, 2000.

[123] C. W. Law, *et al.*, "Effect of pyrolysis temperature on the characteristics of PZT films deposited by the sol-gel method," *Thin Solid Films,* vol. 335, pp. 220-224, 1998.

[124] A. P. Wilkinson, *et al.*, "In-situ x-ray diffraction study of crystallization kinetics in $PbZr_{1-x}Ti_xO_3$ (PZT,x=0.0,0.55,1.0)," *Chemistry of Materials,* vol. 6, pp. 750-754, 1994.

[125] G. Burns and B. A. Scott, "Raman spectra of polycrystalline solids; application to the $PbZr_{1-x}Ti_xO_3$ system," *Physical Review Letters,* vol. 25, pp. 1191-1194, 1970.

[126] L. W. Chen, *et al.*, "Cantilever dynamics and quality factor control in AC mode AFM height measurements," *Ultramicroscopy,* vol. 107, pp. 275-280, 2007.

[127] W. L. Warren, *et al.*, "Degradation mechanisms in ferroelectric and high-permittivity perovskites," *MRS Bulletin,* vol. 21, pp. 40-45, 1996.

[128] N. Bassiri-Gharb, *et al.*, "Domain wall contributions to the properties of piezoelectric thin films," *Journal of Electroceramics,* vol. 19, pp. 47-65, 2007.

[129] S. V. Kalinin and D. A. Bonnell, "Temperature dependence of polarization and charge dynamics on the $BaTiO_3$(100) surface by scanning probe microscopy," *Applied Physics Letters,* vol. 78, pp. 1116-1118, 2001.

[130] Z. Huang, *et al.*, "Piezoelectric PZT films for MEMS and their characterization by interferometry," *Journal of Electroceramics,* vol. 17, pp. 549-556, 2006.

[131] J.-W. Lee, *et al.*, "Thick $Pb(Zr,Ti)O_3$ film without substrate," *Applied Physics Letters,* vol. 91, pp. 072903, 2007.

[132] F. Xu, *et al.*, "Domain wall motion and its contribution to the dielectric and piezoelectric properties of lead zirconate titanate films," *Journal of Applied Physics,* vol. 89, pp. 1336-1348, 2001.

[133] M. W. Liu, *et al.*, "Measurement of longitudinal piezoelectric coefficients (d_{33}) of $Pb(Zr_{0.50},Ti_{0.50})O_3$ thin films with atomic force microscopy," *Proceedings of the Third International Symposium on Instrumentation Science and Technlogy*, vol. 3, pp.352-356, 2004.

[134] Y. Bastani, *et al.*, "Critical thickness for extrinsic contributions to the dielectric and piezoelectric response in lead zirconate titanate ultrathin films," *Journal of Applied Physics,* vol. 109, pp. 014115, 2011.

[135] Y. Matsui, *et al.*, "Thermal stability of Pt bottom electrodes for ferroelectric capacitors," *Japanese Journal of Applied Physics Part 2-Letters,* vol. 37, pp. L465-L467, 1998.

[136] C. S. Ganpule, *et al.*, "Role of 90 degrees domains in lead zirconate titanate thin films," *Applied Physics Letters,* vol. 77, pp. 292-294, 2000.

[137] A. N. Morozovska, *et al.*, Landau-Ginzburg-Devonshire theory for electromechanical hysteresis loop formation in piezoresponse force microscopy of thin films," *Journal of Applied Physics,* vol. 110, pp. 052011, 2011.

[138] D. S. Fu, *et al.*, "Thickness dependence of stress in lead titanate thin films deposited on Pt-coated Si," *Applied Physics Letters,* vol. 77, pp. 1532-1534, 2000.

[139] M. A. McLachlan, *et al.*, "Probing local and global ferroelectric phase stability and polarization switching in ordered macroporous PZT," *Advanced Functional Materials,* vol. 21, pp. 941-947, 2011.

[140] D. McCauley, *et al.*, "Intrinsic size effects in a barium titanate glass-ceramic," *Journal of the American Ceramic Society,* vol. 81, pp. 979-987, 1998.

[141] E. K. Akdogan and A. Safari, "Size effects in nanophase $PbTiO_3$," *Proceedings of the 12th IEEE International Symposium on Applications of Ferroelectrics*, vol.1, pp. 487-490, 2001.

[142] T. Ohno, *et al.*, "Size effect for lead zirconate titanate nano-particles with PZT(40/60) composition," *Advanced Powder Technology,* vol. 18, pp. 579-589, 2008.

[143] A. N. Morozovska, *et al.*, "Finite size and intrinsic field effect on the polar-active properties of ferroelectric-semiconductor heterostructures," *Physical Review B,* vol. 81, pp. 205308 ,2010.

[144] P. Bintachitt, *et al.*, "Collective dynamics underpins Rayleigh behavior in disordered polycrystalline ferroelectrics," *Proceedings of the National Academy of Sciences of the United States of America,* vol. 107, pp. 7219-7224, 2010.

[145] J. Yin and W. Cao, "Polarization reversal study using ultrasound," *Applied Physics Letters,* vol. 79, pp. 4556-4558, 2001.

[146] R. Ahluwalia and W. W. Cao, "Effect of surface induced nucleation of ferroelastic domains on polarization switching in constrained ferroelectrics," *Journal of Applied Physics,* vol. 93, pp. 537-544, 2003.

[147] V. Nagarajan, *et al.*, "Thickness dependence of structural and electrical properties in epitaxial lead zirconate titanate films," *Journal of Applied Physics,* vol. 86, pp. 595-602, 1999.

[148] W. Y. Hsu and R. Raj, "X-ray characterization of the domain-sturcture of epitaxial lead zirconate titanate thin-films on (001)-strontinium titanate," *Applied Physics Letters,* vol. 67, pp. 792-794, 1995.

[149] S. Lis, *et al.*, "Application of flowable oxides in photonics," *Materials Science-Poland,* vol. 26, pp. 189-194, 2008.

[150] F. X. Li and R. K. N. D. Rajapakse, "A constrained domain-switching model for polycrystalline ferroelectric ceramics. Part I: Model formulation and application to tetragonal materials," *Acta Materialia,* vol. 55, pp. 6472-6480, 2007.

[151] T. Mäkelä, *et al.*, "Continuous roll to roll nanoimprinting of inherently conducting polyaniline," *Microelectronic Engineering,* vol. 84, pp. 877-879, 2007.

[152] N. Unno and J. Taniguchi, "Fabrication of the metal nano pattern on plastic substrate using roll nanoimprint," *Microelectronic Engineering,* vol. 88, pp. 2149-2153, 2011.

[153] P. M. Muralt, *et al.*, "Seed-layers of the titania-lead oxide system," *Materials Rearch Society Symposium Proceedings*, vol. 748, pp. 75-80, 2003.

[154] L. E. Ocola, *et al.*, "Lithography for sub-60 nm resist nanostructures," *Journal of Vacuum Science & Technology B,* vol. 17, pp. 3164-3167, 1999.

[155] Z. Q. Wu, *et al.*, "Unusual vortex structure in ultrathin $Pb(Zr_{0.5}Ti_{0.5})O_3$ films," *Journal of Applied Physics,* vol. 101, pp. 014112, 2007.

[156] B. J. Rodriguez*, et al.*, "Vortex polarization states in nanoscale ferroelectric arrays," *Nano Letters,* vol. 9, pp. 1127-1131, 2009.

[157] A. Gruverman*, et al.*, "Vortex ferroelectric domains," *Journal of Physics-Condensed Matter,* vol. 20, pp. 342201, 2008.